UNIVERSITÀ
DEGLI STUDI
FIRENZE

Doctoral Programme in Industrial Engineering

Dottorato di Ricerca in Ingegneria Industriale

XXXIV

Development of a methodology to estimate traumatic brain injuries from signals of sensors embedded into a helmet

ING/IND-14

Doctoral Candidate

Andrea Bracali

Dean of the Doctoral Programme

Prof. Giampaolo Manfrida

Supervisors

Prof. Niccolò Baldanzini

Prof. Marco Pierini

External referees

Prof. Eric Jacquelin

Prof. Francisco Josè Lopez Valdes

Years 2018/2021

Act as if what you do makes a difference. It does. - William James

Summary

Motorcyclists are at high risk in road traffic collisions, however motorcycle usage is growing in popularity thanks to their affordability and their peculiarity to easily move in traffic congestions. The major cause of death and disability to motorcyclists is Traumatic Brain Injuries (TBIs), and the only possibility to protect the head is wearing a certified helmet. Despite the helmet usage, the head can be subjected to a serious impact in road crashes, and early diagnosis and treatment of potential TBIs is the only way to save riders' lives. Recently, the European Community developed an automatic emergency call system (eCall) to enable a rapid and focused treatment in the event of a road crash. However, the adoption of such a device on Powered Two Wheelers (PTWs) is hampered by difficulties in defining exactly when an emergency call needs to be made.

The goal of this study was to develop a methodology for a real time estimation of TBIs in road crashes involving motorcyclists. TBI prediction can be used as activation criterion for the eCall enabling this system for PTWs. The methodology developed in this work consists of 5 single-axis accelerometers attached to the inner surface of the helmet outer shell and an Artificial Intelligence (AI) module, which consists of two sub-modules: the kinematics sub-module and the injury sub-module.

The first part of this study involved the development of the kinematics sub-module. The aim of this sub-module was to estimate the head linear and rotational accelerations. It is based on Long Short Term Memory (LSTM) Artificial Neural Networks (ANNs) fed with the accelerations acquired by the accelerometers embedded into the helmet. ANNs were trained using numerical data obtained reproducing in a virtual environment several helmeted head impact simulations. The model accuracy was investigated with experimental tests reproducing oblique impacts carried out in collaboration with AGV company and the Imperial College of London. Unlike past technologies, the methodology described in this thesis provides an estimation of the head acceleration time patterns without the need of a direct contact between sensors and head, ensuring the possibility of a practical application in the motorcycling field.

The second part of this study focused on the development of the injury sub-module. Its aim was to predict the TBI risk in terms of brain strain and strain rate in 12 specific Regions of Interest (ROI). It is based on Convolutional Neural Networks (CNNs) fed with the components of the linear and rotational head acceleration outputted by the kinematics sub-module. CNNs were trained with numerical data extracted from a finite element model of brain. Experimental oblique impact tests were used to assess the model performances. Results showed that, for specific applications, a detailed 3D computational model of brain used to estimate TBIs can be replaced by ANNs, addressing the main limitations of the computational

models: high computation time and complex computational software. In addition, the results proved that ANNs can be trained using only numerical data and then used with real-world data, drastically reducing the amount of experimental tests needed to develop such complex models.

Contents

List of Figures

List of Tables

Chapter 1

Introduction

1.1 Motivation

Likelihood of road traffic collisions resulting in injuries to motorcyclists is extremely high. The Department of Transport 2019 annual report revealed that in Great Britain motorcyclists have the highest crash and injury rates per mile travelled of all road users, which is 65 times larger than car occupants [1]. The Community database on road crashes resulting in death or injury (CARE database) shows that motorcyclists were one of the largest category of road traffic deaths in the European Union (EU) accounting 15.6% of all road deaths in 2019. According to the National Highway Traffic Safety Administration (NHTSA), a similar trend was observed in the same year in the United States (US), where 5014 motorcyclists died in road collisions, representing 14% of all road deaths [2].

1.1.1 Traumatic Brain Injury

Traumatic Brain Injury (TBI) is the most frequent cause of serious and fatal road crashes for motorcyclists [3, 4]. In fact, lack of an external protection exposes motorcyclists to riskier head impacts than car occupants in crashes. The standard certified helmet is the only protective device that can be exploited to reduce frequency and severity of this kind of injury. Its function is absorbing the energy during an impact and consequently reducing the force and the translational acceleration sustained by the head, leading to a reduction of skull fractures and associated intracranial bleeding likelihood [5]. Linear acceleration is known as the main cause of focal injuries [6], therefore the helmet contributes in reducing focal injuries too.

In the event of an impact, the head is also subjected to a rotational motion which is extremely dangerous for the brain. Nowadays, head rotational kinematics is acknowledged as the leading cause of diffuse injuries and subdural haematoma [7, 8]. Considering the key role played by rotational kinematics on brain injuries, the United Nations Economic Commission for Europe revised the ECE 22.05 helmet homologation standard [9]. The new regulation, ECE 22.06, took effect on January 2021 and introduced new tests for homologation, based also on the rotational acceleration [10]. In addition, new technologies, that can be integrated into the helmet with the aim of reducing the head rotation during an impact, are now available on the market. Two of the most used technologies are the Flex (three-layer impact liner) and the Multi-Directional Impact Protection System (MIPS). Flex

liner includes three layers with different materials (Expanded Polystyrene (EPS), Expanded Polyolefin (EPO) and Expanded Polypropylene (EPP)) that can provide a reduction of linear and rotational impact energies [11]. MIPS is a thin layer inserted between the foam liner and the comfort liner able to reduce the rotational energy transferred to the head [12].

1.1.2 Automatic Emergency Call Systems

Timely treatment of traumatic brain injuries is another key aspect to consider to minimize their consequences [13]. In line with this, the European Community developed an automatic emergency call system (eCall) for road crashes. This system became mandatory for all the new cars from 2018, while it is still under investigation for motorcyclists. The adoption of this solution on Powered Two Wheelers (PTWs) is hampered by difficulties in defining exactly when an eCall needs to be made. As the helmet is mandatory in several countries, turning it into a sensing device able to estimate TBIs in real time could be a proper activation criterion to enable the eCall system also for riders.

1.1.3 Head kinematics estimation

The development of wearable devices for the estimation of TBIs has been addressed over the last 20 years. TBI risk assessment is commonly performed assessing the head kinematics during an impact and linking it to the injury risk. The Head Impact Telemetry System (HITS) [14] and 6 Degree of Freedom (6DOF) [15] were two of the earliest and most widely used devices, integrated into a helmet, to collect kinematic data in the sport field. However, they required sensors to be placed as close to the head as possible to achieve acceptable results. Thus, latest efforts have been focused on the development of instrumented mouthguards, which are commonly worn by athletes and can provide a closer connection of the sensors to the head than the one provided by HITS or 6DOF. However, mouthguards cannot be considered for a daily usage with motorcycles and scooters and for a further integration with the eCall system. Despite their good capability in the prediction of head Centre of Gravity (CoG) kinematics due to their rigid connection with the head, there is an acceptability problem. In fact, the rider (scooter or motorcycle user) should change its behaviour to adopt these devices and previous research projects (SAFERIDER and RiderScan, EU funded projects) showed a riders' resistance to the introduction of new technologies and change of their habits.

1.2 Research objectives

In this context, new technologies to enable crash detection and emergency treatment for riders should be deepened. This is the purpose of the present work, which focuses on the development of an innovative methodology for a real time estimation of motorcyclists' traumatic brain injuries in crashes. TBI likelihood predicted with this methodology can be used as an activation criterion to trigger the eCall system. In addition, rescuers can benefit from these data, ensuring a fast and appropriate treatment.

The goal of this thesis can be broken down into different challenges. First, the devices developed for similar purposes were analysed. As TBIs are connected to

head kinematics, the aim of these devices was to estimate the head kinematics with a good approximation. However, all of them were developed for sport applications and they needed sensors placed as close to the head as possible or even rigidly connected to it. The methodology described in this thesis was conceived to be worn by motorcyclists, therefore a comfortable and user friendly solution should have been implemented. This can be obtained embedding the sensors into the helmet outer shell, but helmet and head are not rigidly connected, and they can move quite independently. The first challenges faced in this work were related to this aspect: 1) Is it possible to estimate the head accelerations with sensors embedded in the helmet, far from the head? 2) May it be easier to determine the acceleration of the helmet CoG and then to estimate the head CoG acceleration via an appropriate transfer function? 3) Could the prior assessment of the helmet kinematics contribute to a more accurate assessment of the head accelerations?

To fully achieve the purpose of this work, a tool to predict the TBI risk based on the head kinematics was needed. If existing injury criteria can be a direct link to the head kinematics and they can provide a real-time assessment, their accuracy is still poor to be used in real-world applications. On the other hand, TBI estimation based on detailed computational models of brain would achieve a more accurate prediction, but high computation time and complex computational software could not ensure a real-time estimation. In this context, 4) Is it possible to make a real-time TBI estimation based on the head kinematics?

Overall, this work wants to investigate the previous questions in terms of feasibility rather than accuracy, as the accuracy is strongly dependent on the models used.

The techniques used to face these challenges and therefore to accomplish the aim of this work are multidisciplinary and involve algorithms such as artificial neural networks and computerized methods such as finite element analysis.

1.3 Research process

The work of this thesis started with an accurate state of the art review (Chapter 2). The main gaps of the systems to estimate the head kinematics deployed in the last years were highlighted and the different approaches were chosen for the concept of the methodology described in this thesis. Partnerships with helmet manufacturers such as AGV (Dainese SpA) and research universities such as the Imperial College of London (ICL) were started to gather know-how from different engineering areas.

The first faced challenge was adapting the 6 Degrees of Freedom (6DOF), which is one of the most used method to the estimation of the linear and rotational head accelerations for on-field applications, to the estimation of the helmet centre of gravity accelerations. Results showed that the helmet deformability affected the 6DOF functioning resulting in poor performances in the estimation of the helmet accelerations.

The second faced challenge involved the direct estimation of the head kinematics using accelerometers embedded into the helmet outer shell. The state of the art review revealed areas where the indirect identification of a load time history using signals acquired by sensors are currently deepened. The concept of a technical solution based on neural networks was developed and implemented in a virtual environment. A collaboration with AGV and the Imperial College of London was established to test this solution using an experimental set-up and promising results

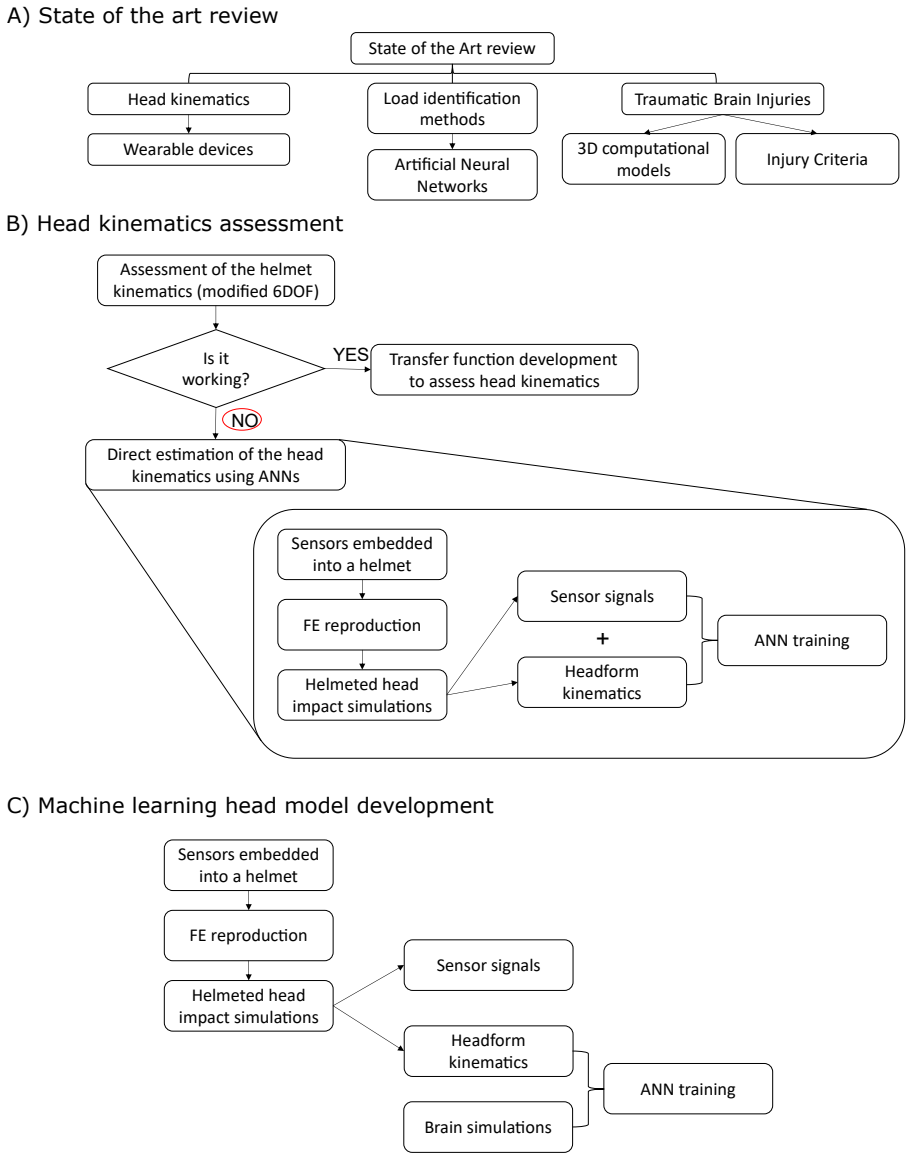

Figure 1.1: Illustration of the research process. Review of the State of the Art (A), Head kinematics estimation process (B), process used to develop the machine learning head model (C).

were obtained.

The last challenge involved the development of a methodology to predict TBI risk using the head kinematics estimated with the method discussed in the last paragraph. Again, the review of the state of the art gave interesting tools and approaches to be exploited. An algorithm based on neural networks to predict the brain deformation in real-time was developed using finite element simulations. Experimental tests were carried out in a collaboration with the Imperial College of London to assess the performances of the algorithm, obtaining promising results.

1.4 Thesis outline

Chapter 2

This chapter describes the literature review of the different topics studied in this research. A detailed analysis of the state of the art has been performed as it represents the starting point of the development of a new technology and allowed me to correctly situate the contribution of this research in relation to existing frameworks. Finally, the steps involving the development of the smart helmet described in this paper are discussed along with its results.

Chapter 3

Can the assessment of the acceleration of the helmet Centre of Gravity facilitate a subsequent estimation of the head kinematics? In an attempt to answer this question, one of the most widely used systems, the 6DOF system, was modified with the aim of estimating the linear and rotational acceleration components of the helmet CoG. The research was carried out by reproducing in a virtual environment three different impacts of a finite element model of a helmet integrated with accelerometers and a deformable plate. After the description of the method, results are presented and discussed in this chapter.

Chapter 4

This chapter describes the development of a new methodology for estimating head kinematics using Artificial Neural Networks (ANN). Data acquired by twelve accelerometers attached to the inner surface of helmet outer shell are processed by an artificial intelligence module to estimate the accelerations of the head centre of mass. The methodology was developed in a virtual environment reproducing impacts of a helmet model coupled with the Hybrid III head model and a deformable plate. After the description of the method, results are presented and discussed in this chapter.

Chapter 5

The methodology described in chapter 4 has been further investigated in this chapter. The positioning of the accelerometers and their minimum number to obtain acceptable results have been analysed. Finally, an experimental campaign was carried out in collaboration with Dainese SpA and Imperial College of London to verify the possibility of training the neural network described in chapter 4 using only numerical data. After the method description, results are presented and discussed in this chapter.

Chapter 6

In this chapter a computational model of human brain was used to develop a 'machine learning head model (MLHM)' to estimate strains and strain rates in key areas of the brain. The input data used to train the model are the Hybrid III head CoG acceleration data extracted in the study described in chapter 4, while deformations and strain rates in key areas of the brain derived from numerical simulations using a finite element model of human brain were used as output data. After the method description, results are presented and discussed in this chapter. This study was carried out at the 'Head Lab' department of the Imperial College London.

Chapter 7

In this chapter the conclusions are discussed. These summarize the findings presented in the previous chapters and underline how the research relates to the state of the art.

1.5 Methodology concept overview

This section describes the concept of the methodology developed in this work. It consists of a number of accelerometers normal oriented to the inner surface of a helmet shell and attached to it. In the event of an impact, the signals acquired by the accelerometers are given as input to an Artificial Intelligence (AI) module composed by two sub-modules: the kinematics sub-module and the injury sub-module (Figure 1.2).

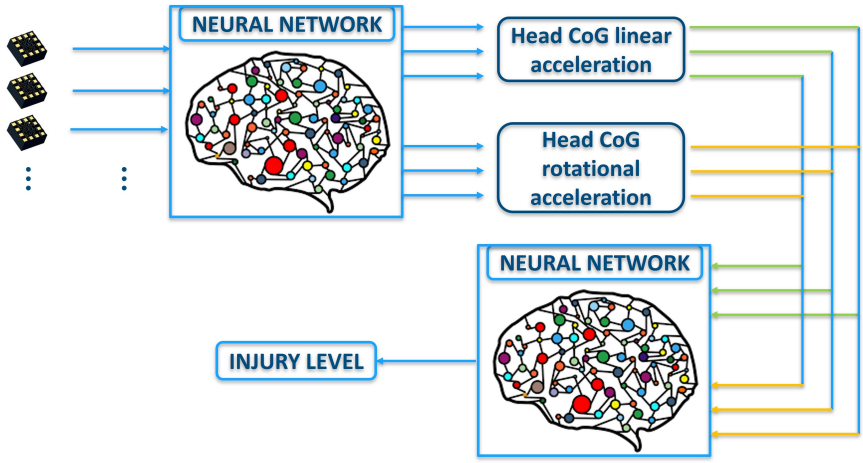

Figure 1.2: Artificial intelligence module.

Specifically, the kinematics sub-module is based on LSTM networks. It is fed with the adequately filtered accelerations acquired by the sensors attached to the helmet. It returns as outputs the components of the linear and rotational accelerations of the head which are given as inputs to the injury sub-module. This is based on CNN networks and its function is to predict the brain injury level in terms

of strain and strain rate of the brain tissue. The steps covered in the development of the two sub-modules can be found respectively in chapter 4 and 6.

A full-face model of helmet (AGV X 3000, size 58/59), certified both DOT FMVSS 218 and UNECE 22.05, was used to obtain the needed data to train ANNs of the kinematics sub-module. This means that this module will only be suitable for this specific helmet model. As the AI module is designed to be trained using mainly numerical data, this procedure can be repeated with any helmet. A few number of experimental tests are still needed to validate the FE model of any new helmet.

On the other hand, the injury module was trained using data obtained from the finite element model of brain belonging to the Head Lab department of the Imperial College of London [16]. Any implementation of the AI module on another helmet will not affect this sub-module. Indeed, the inputs provided to the injury sub-module are the head accelerations, even though they may change based on the helmet type, they will not affect the brain response.

Chapter 2

State of the Art

In this chapter, a state of the art analysis of the various areas of research covered in this work is described. The three main areas studied are Traumatic Brain Injuries (TBIs), the head centre of gravity accelerations estimation using sensorized protective devices, Artificial Neural Networks (ANNs). Specifically, for each of these topics a literature review of the field of interest is done and the main gaps which has been found are highlighted. The technical matters are described in detail in future chapters.

This chapter concludes with an overview of the innovative methodology to estimate TBIs deepened in this work. This section may help the reader to fully understand the different steps involved in the smart helmet development that are described in the further chapters.

2.1 Traumatic Brain Injuries

Traumatic brain injury is defined as an alteration in brain function, or other evidence of brain pathology, caused by an external force [17]. The external force that causes the injury is addressed as injury mechanism, while the mechanical behaviour of the brain exposed to the force is called mechanical response [18]. This chapter will deepen TBI starting from the anatomy of the head, describing the different typologies of injuries, their severities, moving on to the injury mechanisms and criteria. Finally, Finite Element models of human head and deep learning head models will be discussed.

2.1.1 Anatomy of the head

The head is the upper portion of the body. The most interesting parts of the head from a mechanical point of view are the scalp, skull, blood vessels, meninges, cerebrospinal fluid, cerebrum, cerebellum and brain stem.

The scalp consists of 5 layers, as shown in Figure 2.1 the skin, connective tissue, epicranial aponeurosis, loose areolar tissue, and pericranium. Under the scalp there is the skull, a protective envelope for the brain and the sense organs. It is composed by face and cranium, with the last one that comprises 8 bones: occipital bone, two temporal bones, sphenoid bone, frontal bone, two parietal bones and ethmoid bone.

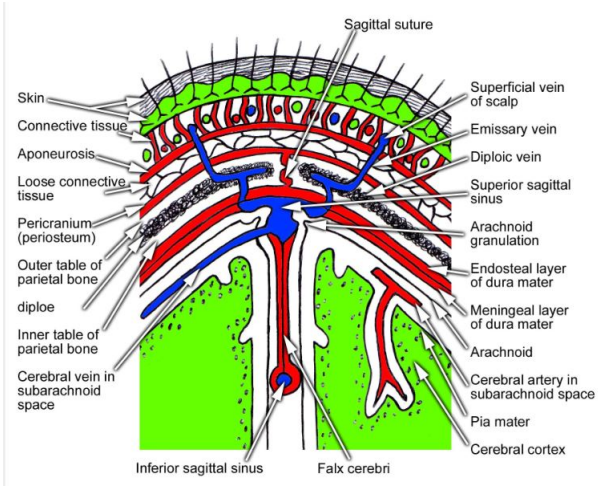

Figure 2.1: Coronal section of the scalp (adopted from Medscape).

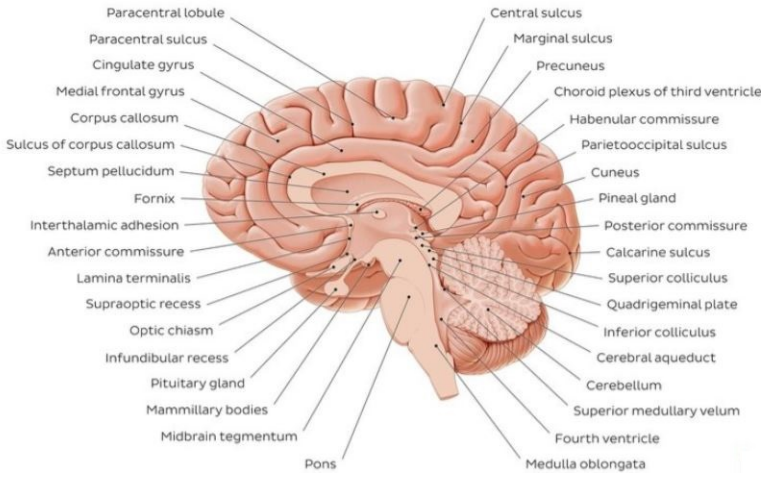

Figure 2.2: Midsagittal view of brain (adopted from kenhub).

Table 2.1: Glasgow coma scale.

Eye opening		Motor response		Verbal response	
Spontaneous	4	Obeys	6	Oriented	5
To speech	3	Localises	5	Confused	4
To pain	2	Withdraws	4	Inappropriate	3
None	1	Abnormal flexion	3	Incomprehensible	2
		Extensor response	2	None	1
		None	1		

The meninges are the three membranes aimed to protect the brain and the spinal cord (Figure 2.1). The outer membrane, closest to the skull, is called dura mater. The Arachnoid mater is the middle one, instead the pia mater is the inner membrane, the closest to the brain tissue. Between the arachnoid mater and the pia mater there is a space filled with a fluid called cerebrospinal fluid. It cushions and protects the brain from external impact loads or movements.

The brain is the most complex organ of the human being. At a high level, it comprises 3 parts: cerebrum, brainstem and cerebellum (Figure 2.2). The cerebrum is the largest part of the brain (occupies approximately 85% of the cranial space) and it comprises grey matter and white matter. Grey matter is mainly made of neuron somas (the cellular body of the neuron), while the white matter mostly comprises axons (the main fiber that starts from the soma bringing to other neurons the output).

The brainstem is the bridge between the cerebrum and the spinal cord. It comprises three parts: midbrain, pons and medulla. The midbrain is a complex structure made of several neuron clusters and other structures, the pons is a round bulge located above the medulla oblongata, which is the most inferior part of the midbrain and where the brain meets the spinal cord.

2.1.2 Type of Injury and their severity

Focal and diffuse brain damage are the principal mechanisms of TBIs: the former is the main cause of injury types such as contusion and intra-cranial haemorrhage, the latter is mainly linked to Diffuse Axonal Injury (DAI) or brain swelling [19–22]. At first instance, traumatic brain injury severity is determined on the basis of the level of consciousness or Glasgow coma scale (GCS) score after resuscitation (Table 2.1). After a general check-up, 3 different values are assigned to the patient based on its eye opening, motor and verbal responses. The GCS score is obtained adding these 3 values. A GCS score of 13-15 corresponds to a mild TBI mostly resulting in a concussion with full recovery. GCS scores of 9-13 and 3-8 correspond respectively to a moderate and a severe injury.

TBIs can occur in different forms: concussion, Diffuse Axonal Injury, contusions, hematomas. Concussion is a transient and reversible alteration of the mental status frequently involving loss of consciousness or memory lasting less than six hours [23]. DAI occurs when the brain is subjected to a high deceleration resulting in a widespread rupture of axonal fibers and myelin sheaths. The main symptom of DAI is a loss of consciousness for more than six hours [24, 25]. Contusions and hematomas can happen consequently to open or closed impacts. Contusions symptoms depend on contusion size and location commonly resulting in edema

and increased IntraCranial Pressure (ICP). Hematoma can be epidural, subdural or intracerebral. It consists of a blood collection and it can generate edema and increased ICP [26, 27].

The Abbreviated Injury Scale (AIS) is the commonly used index to quantify the severity of injuries throughout the body [28]. AIS has a range of severities identified by increasing numbers from 0 to 6: no injury, minor, moderate, serious, severe, life threatening, fatal. AIS is used to analyse severity of individual injuries all over the body. Instead, the overall injury severity is assessed considering the maximum value of AIS indices of a patient with multiple injuries, usually referenced with MAIS [29].

2.1.3 Injury mechanisms

During an impact, the brain faces a complex variety of responses, both in kinematics and deformation, that makes extremely difficult to fully associate injuries to their causes. Over the years, researchers investigated how the mechanical energy resulting from an impact is transferred from the skull to the brain and how it affects the brain tissue, as this is a key aspect to understand concussion and DAI.

Bulk modulus of brain is five or six order of magnitude greater than the shear modulus [30–32]. As a result, the deformation of the brain tissue is primarily influenced by the shear, which is usually associated to concussion and DAI [33]. Indeed, shear brings to the extension of the axons, which are a portion of the neurons in charge of carrying nerve impulses.

Positive and negative pressures are the major mechanisms of hematomas and contusions [18]. When the head suffers an impact, a positive pressure arise at the site of the impact, while a negative pressures occurs at the countrecoup site generating contusions in these locations. In addition, the relative motion between brain and skull can lead to the stretch or shear of the bridging veins that drain blood to the superior sagittal sinus from the brain. This mechanism can result in veins rupture (Hematomas).

2.1.4 Injury criteria

Currently, TBI risk assessment is performed with criteria comprised of a biomechanical metric and an injury risk function. The former condenses the severity of an impact suffered by the head, the latter is used to connect the previously described metric and its brain injury likelihood. Two main types of biomechanical metrics were developed over the years: one group is based on kinematic parameters of the head, while another on the brain tissue deformation suffered by the brain matter during the impact. Most of the existing injury criteria are based on the head kinematics because it is easier measuring head kinematics response, either on a dummy or a volunteer, than measuring brain tissue response.

Head kinematics based criteria

The head kinematics can be divided into two different components: translational and rotational kinematics. Some of the existing criteria are based exclusively on translational head kinematics, others are based on rotational head kinematics only, some others included both translational and rotational head parameters.

Injury criteria based on linear acceleration were the first ones to be developed. In 1966 the Gadd Severity Index (GSI) [34] was proposed fitting the Wayne State Tolerance Curve, which is based on skull fracture data [35]. Some years later it was developed the Head Injury Criterion (HIC) [36], which is the most commonly used metric for evaluating head and brain injury risk. It is currently the only head injury criterion required by UN/ECE 22.05 standard [9], used in helmet regulation and it is used also in Euro NCAP testing Protocols [37, 38].

$$HIC = max\left\{(t_2 - t_1)\left[\frac{1}{t_2 - t_1}\int_{t_1}^{t_2}|a(t)dt|\right]^{2,5}\right\} \tag{2.1}$$

where a is the magnitude of the resultant head linear acceleration, instead t_1 and t_2 are respectively the initial and final integral times over which HIC is calculated (t_1 and t_2 are selected so as to maximize HIC).

More recent studies identified the rotational motion of the head as the main cause of TBIs [7, 39–41]. The latter findings triggered the development of new injury criteria based on the rotational movement of the brain. Some of the most important are listed below:

Generalized Acceleration Model for Brain Injury Threshold (GAMBIT)

In 1986 [42] Newman proposed this criterion that considers kinematics analogue to maximum shear stress/strain theory. Thus, the combination of linear (a) and rotational (α) accelerations was assumed "equivalent" to the normal and shear stresses.

$$GAMBIT = max\left[\left(\frac{a(t)}{a_c}^n + \frac{\alpha(t)}{\alpha_c}^m\right)\right]^{\frac{1}{s}} \tag{2.2}$$

where a is the magnitude of the resultant head linear acceleration and a_c is its critical value, α is the magnitude of the resultant head rotational acceleration and α_c is its critical value, the exponents n, m, and s are empirically determined constants.

Head Impact Power (HIP)

This criterion was proposed by Nemann et al. [43] in 2000. HIP is based on the hypothesis that the rate of change of head kinematics energy is linked to the probability of head injury.

$$HIP = max\left\{m\sum a_i(t)\int a_i(t)dt + \sum I_{ii}\alpha_i(t)\int \alpha_i(t)dt\right\} \tag{2.3}$$

where a is the magnitude of the resultant head linear acceleration, α is the magnitude of the resultant head rotational acceleration, I_{ii} are the principal moments of inertia of the head about the anatomical axes and m is the head mass.

Rotational Injury Criterion (RIC)

RIC was proposed by Kimpara et al. [44]; it was formulated similarly to HIC, by replacing the linear acceleration term with the angular acceleration.

$$RIC = max\left\{(t_2 - t_1)\left[\frac{1}{t_2 - t_1}\int_{t_1}^{t_2}|\alpha(t)dt|\right]^{2,5}\right\} \tag{2.4}$$

where α is the magnitude of the resultant head rotational acceleration, instead for t_1 and t_2 the same considerations made for the HIC are applicable.

Brain Injury criteria (BrIC)

The BrIC was proposed in 2013 by Takhounts et al. [45] as an update of the Kinematic Rotational Brain Injury Criterion (BRIC) [46]. BrIC is entirely based on angular velocity.

$$BrIC = \sqrt{\left(\frac{\omega_x}{\omega_{xcr}}\right) + \left(\frac{\omega_y}{\omega_{ycr}}\right) + \left(\frac{\omega_x}{\omega_{zcr}}\right)} \tag{2.5}$$

where ω_x, ω_y and ω_z are the X-, Y- and Z- components of the angular velocity and ω_{xcr}, ω_{ycr}, ω_{zcr} are their critical values determined using FE modelling [45].

Rotational Velocity Change Index (RVCI)

In 2015, Yanaoka et al. [47] proposed a new criterion based on the change of the head rotational velocity during a certain maximum value. RVIC was formulated to improve correlation between head kinematics and brain tissue-level predictors for diffuse injuries in occupant and pedestrian crashes.

$$RVIC = \sqrt{R_x\left(\int_{t_1}^{t_2}\alpha_x dt\right)^2 + R_y\left(\int_{t_1}^{t_2}\alpha_y dt\right)^2 + R_z\left(\int_{t_1}^{t_2}\alpha_z dt\right)^2} \tag{2.6}$$

where α_x, α_y and α_z are the angular accelerations respectively around the X, Y and Z axes, R_x, R_y and R_z are weighting factors about each determined using a head FE model. For t_1 and t_2 the same considerations made for the HIC are applicable [47].

Universal Brain Injury Criterion (UBrIC)

In 2018, Gabler et al. proposed UBrIC [48], a criterion applicable to a wide range of impact conditions including sport and automotive. It is based on the hypothesis that maximum brain deformation generated by rotational head motion is equivalent to the deformation undergone by a second-order system under excitation.

$$UBrIC = \left\{\sum\left[\omega_i^* + (\alpha_i^* - \omega_i^*)e^{-\frac{\alpha_i^*}{\omega_i^*}}\right]^r\right\}^{\frac{1}{s}} \tag{2.7}$$

both the head angular velocity (ω_i^*) and angular acceleration (α_i^*) are normalized using a critical value obtained using a head FE model. The constant parameter r establishes the power at which the magnitude is evaluated and is generally taken equal to 1 or 2.

Diffuse Axonal Multi-Axis General Evaluation (DAMAGE)

DAMAGE [49] was proposed in 2019 by Gabler et al. and it is based on the equations of motion of a three degree of freedom second-order system. DAMAGE estimates the maximum brain strain using the entire time history of the head angular acceleration.

$$DAMAGE = \beta max_t \left\{ \left| \delta(\vec{t}) \right| \right\} \tag{2.8}$$

where β is a scale factor and $\delta(\vec{t})$ is the displacement time history vector obtained as solution of the equations of motion for a damped three degree-of-freedom coupled mechanical system under excitation [49].

Applications of these criteria range from the estimation of the level of trauma in crash reconstruction to vehicle homologation, using sensors of anthropometric test dummies. All these criteria may also be used to estimate injuries directly in real world crashes, but their application is hampered by the technological limits in performing a precise and accurate estimation of the kinematic data (linear and rotational accelerations).

Tissue deformation based criteria

Strain and stress sustained by the brain during a head impact well correlate with the reported brain injuries [50, 51]. Several head injury predictors based on tissue deformation have been studied and developed over the years. Some of the most important and interesting ones are here described.

Brain pressure: This predictor is based on the IntraCranial Pressure (ICP), i.e. the gradient of pressure that arises into the cranial cavity after an impact [52]. In 1980, Ward et al. using an analytical-experimental to investigate the response of the animal and human cadaver brains proposed threshold values of 173kPa and 235kPa for the ICP respectively for minor and serious injuries [53]. In 2007, Kleiven [54] suggested a threshold value of 65.8kPa for mild TBI based on 58 football player collision cases reconstruction using finite element model analyses.

Strain and Strain Rate: The Maximum Principal Strain has been addressed as a close predictor of diffuse axonal injuries [55]. The rate of first principal strain is another predictor for TBI introduced for the first time by Zhang et al. [56]. In addition, in the study previously mentioned [54], Kleiven suggested tolerance thresholds for MTBI:

- A 1^{st} principal strain in corpus callosum equal to 0.21;
- A 1^{st} principal strain in the grey matter equal to 0.26;
- A 1^{st} principal strain rate in the grey matter equal to 48.5 $1/s$;

Nowadays, researchers are still performing studies to understand the correlation between tissue strain or strain rate and TBI. Two of the most recently studies [57, 58], confirmed that strain and strain rate are important factors in determining patterns of diffuse axonal injuries. Specifically, Donat et al. [58] performed controlled cortical

impacts on rats, comparing the experimental results with FE simulations, while Hajiaghamemar et al. [57] performed tests on pigs to quantify the relationship between axonal injury and tissue deformations.

2.1.5 FE models of the human head

Recently, computational modelling of TBI using detailed finite element model of human head (Figure 2.3) is getting more and more significant [16, 32, 54, 59] . Unlike head kinematics, brain tissue deformation measurement is impossible in the real world with current technologies and finite element modelling (FEM) became the state of the art method to compute brain tissue response. Indeed, most of the tissue level injury predictors previously discussed are assessed using FEM simulations. In the last years, several brain models have been developed and validated to be used to assess TBIs. Validation is the critical step in the development of these models. Most of the brain FEM developed over the years were validated using cadaveric head impact experimental data. Some of the brain FEM currently used are: the Strasbourg University Finite Element Head Model (SUFEHM) [60] ,the Simulated Injury Monitor (SIMon) [32], the model developed at the Royal Institute of Technology in Stockholm [54] and the model developed at the Imperial College of London by Ghajari et al. [16].

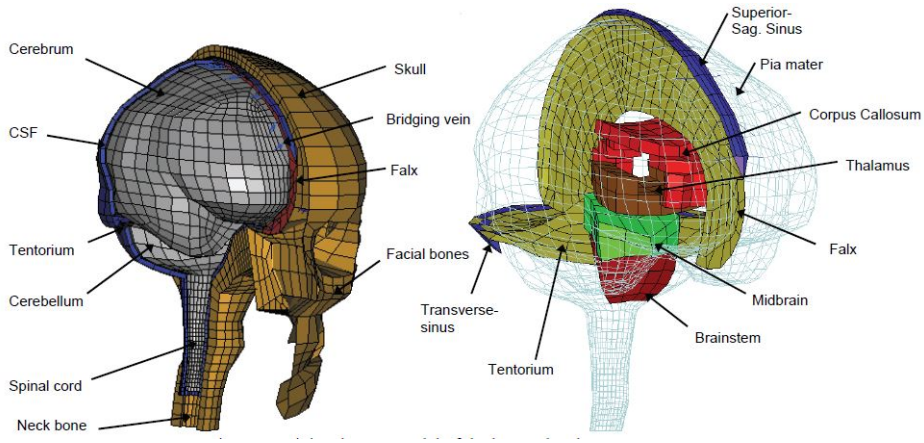

Figure 2.3: Example of finite element model of the human head (adopted from [54]).

High computation time and complex computational software are the main limitations of FEM which hampered tissue level predictors from becoming metrics to estimate TBI in real world applications.

2.1.6 Developed Machine Learning Head Models

In the last years Developed Machine Learning Head Models (MLHMs) are beginning to be explored to address the limitations introduced by FEA. They consist in deep learning techniches applied to existing finite element models of human head. This process generates algorithms used to assess in few milliseconds the same outputs obtained with hours of simulations. The first example of deep learing model applyied to a FE model to develop a surrogate of FEA for stress analysis was performed by

Liang et al. [61] in 2018. The authors exploited 729 aorta geometries and stress distribututions to train and test their model; it was able to assess the Von Mises stress distribution and the peak Von Mises stress with average errors of respectively 0.492% and 0.891%.

In 2019, Shaoju Wu et al. [62] exploited a Covolutional Neural Network (CNN) to approximate the complexity of the Worcester Head Injury Model (WHIM) [63] and instantly estimate MPS of the whole brain, MPS of the corpus callosum, and fiber strain of the corpus callosum. They used 2592 training samples obtained augmenting 53 National Football League (NFL) lab reconstructed impacts and 110 video confirmed impacts measured in college sports. Performances were estimated using an independent impact dataset of 314 NFL impacts. Results showed that CNN achieved a $R^2 = 0916$ in a 10-fold cross-correlation [64].

In 2021, Zhan et al. [65] proposed several MLHMs developed using two different methodologies: data fusion and transfer learning. The difference lied in the data combination used to train the different MLHMs. Data fusion strategy combines a dataset of 12780 head impact simulations and a certain number of on-field impacts to obtain the training dataset. Transfer learning strategy uses a double training: a first training using only the head impact simulations dataset and a second one using only on-field datasets. In the same year, Bourdet et al. [66] developed a deep learning model to approximate the Strasbourg University FE Head Model (SUFEHM) complexity and make a fast assessment of the Maximum Von Mises (MVM) stress substained by the brain. The authors used a dataset of 3754 motorcycle and bicycle tests to train, validate and test the deep learing model. It was shown that models based on deep learning technique can accurately estimate the brain response and ultimately they may replace FEM.

The state of the art review on TBIs provided interesting insights. In summary, FEM is an extremely powerful tool to compute TBI, but its usage in real-world applications is hampered by the high computational time required and its complexity. Replacing FEM with machine learning head models can be the solution to these limitations, but few studies are still available on this topic, since its a novel approach, to exploit these models in real-world applications. New studies are therefore needed to provide more evidences on the MLHM effectiveness.

2.2 Methods to estimate the head CoG accelerations

A reliable method to assess head kinematics during an impact is crucial for the development of a smart helmet able to estimate brain injuries in real time. This issue has been addressed by many researchers in the last two decades, with the greatest efforts made in the development of wearable devices for sports applications. Concurrently, several mathematical methods were developed to indirectly identify impact load time history from data acquired by sensors. In this section, a review of the state of the art dealing with these two aspects will be described.

2.2.1 Wearable devices

While brain FE models are essential for estimating TBI, equally important is the input provided to these models, i.e. the head kinematics, which can be measured by various wearable devices. Recent advances in impact sensing technology have enabled the spread of on-field measurement devices able to collect in real-time impact data including instrumented helmets/headgears, headbends, earplugs, and mouthpieces. These systems incorporate micro-electromechanical systems (MEMS) inertial sensors to measure linear and rotational accelerations and rotational speed at the Centre of Gravity (CoG) of the head.

HITS and 6DOF

Considering instrumented helmets/headgears, Head Impact Telemetry System (HITS) [14] was one of the earliest and most widely used device developed for sport applications [67–73]. Specifically, HITS or similar versions of it were developed for use in hockey helmets [74, 75], football helmets [67, 71], boxing head-gear [76] and soccer headgear [77]. This device is comprised of an array of 6 single-axis accelerometers, a data acquisition system, an on-board memory and a wireless transceiver; each accelerometer is embedded in a fabric padding physically attached to the helmet padding. This insert acts as a spring maintaining the essential contact between head and the accelerometers during an impact. The axes of the accelerometers are orthogonally oriented toward the head surface. Referring to the head as to a sphere with centre (O), location of any point on the sphere surface can be identified by its azimuth (θ) and elevation angle (α) (Figure 2.4).

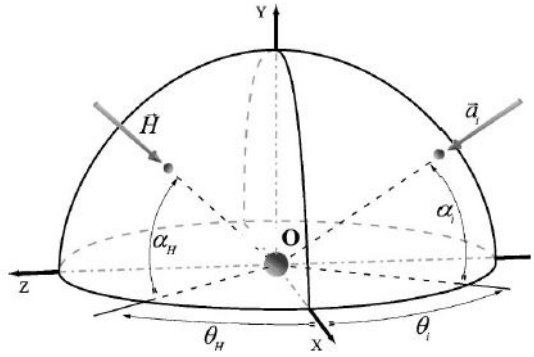

Figure 2.4: Head sketched using a hemisphere of center O (adopted from [14]).

Considering a set of n head-mounted accelerometers and a generic impact vector $\vec{H}$, the acceleration magnitude $\vec{a_i}$ at each accelerometer location a_i can be estimated through a mathematical procedure described in [14]. The final equation is given as follow:

$$||a_i|| = \left|\left|\vec{H}\right|\right| (\cos\alpha_i \cos\alpha_H \cos(\theta_i - \theta_H) + \sin\alpha_i \sin\alpha_H) \tag{2.9}$$

where (θ_i, α_i) is the location of the i-th accelerometer a_i. Since formula of equation 2.9 returns an approximation of $||a_i||$, the head linear acceleration magnitude

at point O $\left|\left|\vec{H}\right|\right|$ and the impact location (θ_H, α_H) are assessed by minimizing the least-square error as follow:

$$\sum_{i=0}^{n}(\left|\left|\vec{H}\right|\right|(\cos\alpha_i\cos\alpha_H\cos(\theta_i-\theta_H)+\sin\alpha_i\sin\alpha_H)-||a_i||)^2 \tag{2.10}$$

The rotational acceleration is estimated from the linear acceleration vector and a hypothetical pivot point taken 10cm below the head CoG. Rowson et al. [72] suggested an alternative equation 2.11 derived from the equation of motion.

$$\gamma = (m\sqrt{a_x^2+a_y^2}d)/I \tag{2.11}$$

where γ is the rotational acceleration peak, m the head mass, a_x and a_y linear acceleration peaks respectively along the anterior–posterior axis and medial–lateral axis of the head, I is the moment of inertia of the head, and d is the perpendicular distance from the head CoG to the impact vector. The same authors describe an experimental validated regression model to estimate the parameters m , d and I too [72].

HITS was updated, reorienting the sensing axes of the accelerometers tangentially to the head surface and adding six single-axis accelerometers for a total of twelve sensors. The new system, named 6 Degree of Freedom (6DOF) measurement device [15] (Figure 2.5) and still used for sport applications [72, 78], estimates both the linear and the rotational accelerations through an iterative optimization of the head equations of motion (2.12) during the impact [15]:

$$||a_i|| = \vec{r_{ai}}\cdot\vec{a}+\vec{r_{ai}}\cdot(\vec{\alpha}\times\vec{r_i}) \tag{2.12}$$

where $||a_i||$ is the acceleration measured by each accelerometer, $\vec{a}$ is the head CoG linear acceleration, $\vec{\alpha}$ is the head CoG rotational acceleration, $\vec{r_i}$ is the accelerometer location relative to the head CoG and $\vec{r_{ai}}$ is the orientation of the sensing axis of each accelerometer. The total squared error between the measured and the estimated acceleration at each location is the cost function for the optimization algorithm [15].

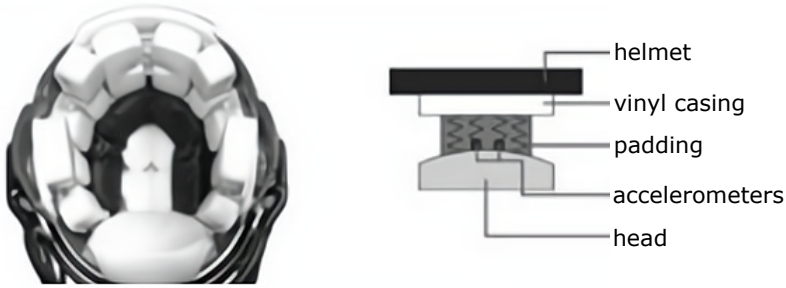

Figure 2.5: 6DOF measurement device installed in a Riddell Revolution helmet (left) and a schematic of the measurement device in the helmet (right) (adopted from [15]).

6DOF and HIT system share the same limitation: sensors need to remain as much as possible in contact with the head to provide accurate results. To address this problem, most of the validation studies of HIT and 6DOF exploited a medium helmet [67, 71] which is too small for the Hybrid III headform compared to how players wear the helmet [73] and therefore is not representative of the reality. Fit is one of the main discriminant for these systems: a helmet fitting loosely has a more pronounced own movement respect to the head than a helmet fitting tightly.

Beckwith et al. [71] conducted experimental tests to replicate impacts occurring in the NFL and correlated the head kinematics recorded by the HIT with those obtained from a Hybrid III headform. Results showed acceleration two to five times greater than the ones showed by the Hybrid III headform when the impact occur at the chin location. A poor accuracy of the HIT system was also shown by Jadischke et al. [73], which reproduced tests in a similar manner to the ones performed by Beckwith et al. [71]. More than half of the impacts showed an absolute error for peak acceleration greater than 15%.

Other devices

Another device is the gForce Tracker (GFT) [79]. This system is characterised by one triaxial accelerometer and one triaxial gyroscope embedded inside a casing attached to a helmet (Figure 2.6). This technology provides the maximum values of the resultant linear acceleration and rotational velocity obtained from a power fit regression. GTF is not widely used since it has average absolute errors up to 40% if the regression is performed incorporating data from all impact directions [79].

Figure 2.6: gForce Tracker device attached on the back part of the helmet outer shell (adopted from [79]).

Head kinematics measurement using instrumented helmets is highly affected by many factors as sensor location, helmet fit, hair/skin properties, relative movement and adhesion. For instance, Wu et al. [80] instrumented volunteers with three devices (mouthpiece (MP), skin patch, and skull cap) using an ear-canal sensor as reference for the skull. This study shows how relative motion between the sensors and the skull highly affects measurements of skin patch and skull cap devices. Wu et al. suggest a mouthpiece device as most suitable and accurate for the head kinematics measurement.

A first use of a mouthpiece is dated 2007, when Higgins at al. [81] demonstrated that an accelerometer attached to a mouthpiece is a valid measurement of acceleration. In the same work Higgins proved that accelerometers attached to the helmet

significantly overestimated head accelerations. The same conclusions can be found in other two studies: Manoogian et al. [82] demonstrated that the helmet peak linear acceleration is more or less 10 times the head peak one; Joodaki et al. [83] proved that the peak linear acceleration of the helmet is 2/5 times greater than the head. Instead, the peak angular velocity of helmet was greater than the head in some tests and less in others.

Recently, mouthpieces have become extensively investigated as a way of measuring the head kinematics. In 2018 Miller et al. [84] validated a custom MP (Figure 2.7) comparing the head kinematics measured by the MP to kinematics of an anthropomorphic test device. The good results obtained ($R^2 > 0.98$ for both rotational velocity and linear acceleration and $R^2 > 0.93$ for rotational acceleration) confirmed that devices rigidly connected to the head are a promising and accurate method of collecting head kinematics data.

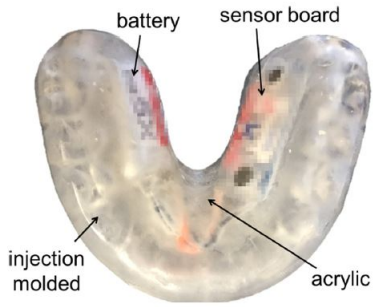

Figure 2.7: Instrumented mouthpiece (adopted from [84]).

Overall, improvement of MP provided the means to record head impact exposure in several sports. From rugby [85] to American Football [86], box and martial art [87], MP were used to collect various head impact data. Reliable devices that can accurately monitor head impact kinematics have great potentiality and can be used to detect an injury-prone impact as deepened by Gabler et al [88]. Other categories of devices comprise skin mounted sensor (xPatch; X2 Biosystems, Seattle, Washington USA), earplugs [89] and bands [90].

From this review it is evident how devices rigidly connected to the head provide more detailed and accurate data, but they are hardly accepted by riders (i.e. motorcycle or scooter users) for daily usage. In fact, a behavioural change would be required to adopt these devices, but previous research projects such as SAFERIDER [91] or RiderScan [92] proved that riders are reluctant to change their habits. The outcomes of the previously mentioned projects indicate that the utmost attention should be dedicated to the riders' acceptability during the development of a new device. In order to minimize any acceptability issue, this category of measuring devices was not further considered in this research. Considering only helmet based systems, the main highlighted issues are the following:

- HIT and 6DOF provided the best performances in the head kinematics estimation, but they need to keep accelerometers as much as possible in contact with the head. As shown in the examples taken from the State of

The Art, accelerometers are kept in contact with the head by specific systems (Figure 2.5), leading to poor comfort and usability;

- None of the systems developed over the years considered road applications but only sport applications.

2.2.2 Head and helmet behaviour during an impact

In the previous section the existing devices to estimate the head acceleration were analysed. However, none of the solutions described is currently used to record head impact data in motorcycle applications. This is mainly due to the poor performances of technologies directly embedded into the helmet, as the head and the helmet are not rigidly connected and they show a relative motion at the contact interface during an impact. This phenomenon is driven by several factors such as the padding compression, chin strap tension, friction between head and helmet, fit. In addition, helmets can be designed to maximize the fit and therefore reduce the relative motion between head and helmet [93, 94] , or to enhance the rotation of the helmet compared to the head rotation [12].

Recently, Joodaki et al. [83] tried to quantify the relative motion between head and helmet in Football impacts. The study was carried out reproducing 7 helmet to helmet impact configurations using instrumented dummies. Sensors were also placed into the helmets. Results confirmed that the kinematics of head and helmet are significantly different during an impact. Indeed, a translation of the helmets in the range 12-41mm and a rotation up to 37° compared to the head were observed during the tests.

The high complexity in the physics behind the impact led researches to move from solutions consisting of accelerometers kept in contact with the head, but still placed on the helmet (HIT, 6DOF), to sensors directly integrated inside the head (MP), as analysed in the previous sections. However motorcyclists can not accept this kind of solution, and new approach should be investigated. To such end, the problem should be rephrased as follows: given a non linear system comprised of two elements loosely interconnected (head-helmet assembly), estimating the acceleration of one component (head) using signals acquired by sensors placed on the other component (helmet). Looking at the state of the art, this issue is experienced in several areas and is known as load identification. For instance, it takes an important role in fields such as strength analysis, vibration control, structural failure estimation, etc. Methods used over the years to address the load identification are deepened in the next section.

2.2.3 Load identification methods

The two main approaches to this problem are the frequency-domain method [95–97] and the time-domain method [98–100]. The former exploits the relationship between the frequency response in output and the frequency spectrum of the structure. The load history is then assessed using a modal coordinate transformation. For the latter the load identification is performed inverting the convolution integral relationship between the loads and structural system responses, which can include displacement, velocity or acceleration. Time-domain methods resulted more accurate and the results showed a better physical meaning, thus more practical compared to frequency-domain methods [101]. Over the years many time-domain method were developed.

In 1992 Kreitinger et al. [102] proposed a method based on the sum of weighted accelerations to identify the forces without knowing the structure model properties. This method was strongly limited to one-dimensional applications. In 2002 Liu et al. [103] proposed an inverse procedure to determine the load acting on a composite plate using two different kernel functions. Pan et al. [104] developed a method for force identification by adopting redundant concatenated dictionary and weighted L1-norm regularization method. In 2009 Mao et al. [105] proposed an algorithm based on the precise time-step integration for Markov parameters. In 2013 Ding et al. [106] proposed a method based on average acceleration discrete algorithm to perform a discrete force identification. The approach adopted by Li et al. [107] is based on Green's function method and orthogonal polynomial fitting technique. In addition to these methods, many others were developed over the years, such as statistical analysis method [108, 109], optimization method [110, 111] and so on.

The stability of time-domain methods is hardly affected by the ill-conditioned transfer function matrix and the measurement noise, also known as ill-posed problem [112]. Several regulation methods were developed to improve ill-posed problems such as Tikhonov regulation method [105, 113], Singular Value Decomposition methods [114], Landweber regulation method [115], conjugate gradient method [116], Levenberg-Marquardt regulation method [117]. The main limitation of all these methods is the difficulty to define the convolution integrals and the transfer functions, mostly applicable only for linear structures. This limitation was overcome by Artificial Neural Networks (ANNs), which are data-based methods that do not require the knowledge of the structure properties. A review of the studies published in the state of the art using ANN to identify load time history can be found in the introduction of chapter 4. The main gap in the state of the art concerns the absence of reliable impact load history identification on a body (head) with sensors attached in a second body (helmet), considering that the two bodies are not fully connected, but they can relatively rotate.

2.3 Artificial Neural Networks

Artificial Neural Networks are a technology derived from several studies performed on brain structure and nervous system functions. Overall, processing of information is performed by different elements (Figure 2.8):

- neurons: are the main working units of the brain designed to transmit information to other nerve cells, muscle, or gland cells;
- synaptic connections (synapses): they act as connecting gates for the passage of information between neurons;
- dendrites: they are minor fibers that branch out from the cellular body of the neuron (called soma). Through the synapses the dendrites collect inputs from afferent neurons and propagate them towards the soma and
- axon: it is the main fiber that starts from the soma bringing to other neurons (even distant) the output.

The access of ions through the synapses of dendrites generates a difference of potential between the body of the neuron and the external part. When this potential exceeds a certain threshold a spike (impulse) is produced. The neuron sends a short

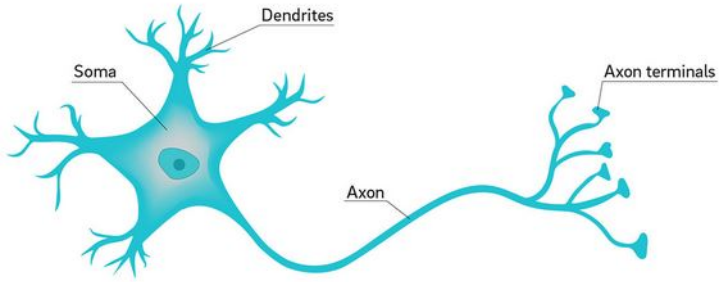

Figure 2.8: Illustration of a neuron (adopted from David Baillot/ UC San Diego).

electrical signal called action potential along its axon: this potential determines the release of ions from the synapses of the axon ensuring the transmission of information.

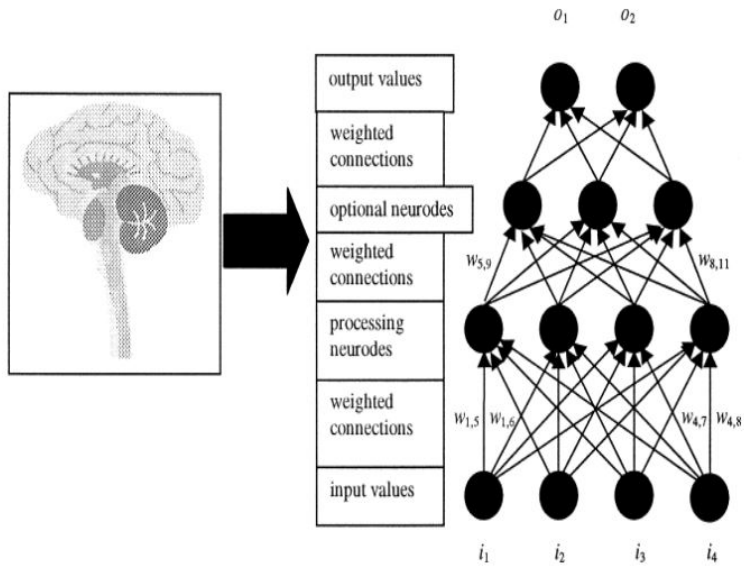

Figure 2.9: Sample artificial neural network architecture (adopted from [118]).

ANNs were developed trying to emulate this complex electrical activity taking place inside the brain. They consist of several deeply connected artificial neurons (nodes) arranged in layers, with the output of a layer given as input to the next layer (Figure 2.9). Specifically, a single node might receive data from all or a subset of nodes belonging to the layer beneath it; these connections emulate the synaptic connections of the brain. A first mathematical model of neuron was proposed in 1943 by McMulloch and Pitts [119]. It used binary data as inputs to produce a single binary output. An improvement of this model was introduced in 1958 by Rosenblatt [120] with the definition of the well known "perceptron". The main idea was to define algorithms capable of learning the function that maps input to output instead of defining them explicitly. Referring to a simple artificial neuron shown in Figure

2.10, each data from incoming connections is weighted simulating the electrical excitation of a nerve cell and consequently the transfer of information within the network or brain. All the weighted values are combined using a summation; an additional weight (bias) is usually considered in the previous summation allowing the activation function to be moved left or right, to better fit the data. Once the combined value has been calculated, a transfer function is used to produce the node output (and hence the input signals for the next processing layer). The most common transfer functions used are logistic sigmoid, Rectified Linear Unit (ReLU) and Hyperbolic Tangent (Tanh). After having defined the ANN architecture, the weight matrix is defined during the training phase using known data, split between inputs and outputs. This process involves the definition of a cost function, i.e. a measure of "how good" a neural network did with respect to its given training sample and the expected output.

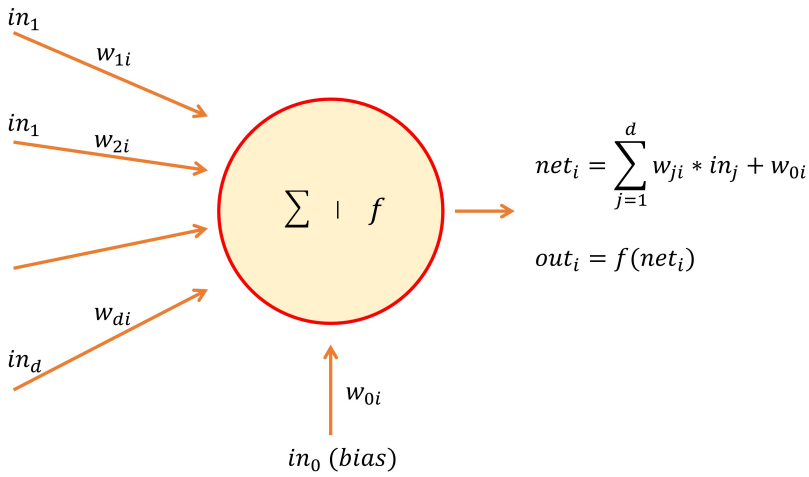

Figure 2.10: Illustration of an artificial neuron.

Training ANN consists of minimising the cost function moving in the negative direction of its derivative. The process of calculating the derivatives is called back-propagation [121]; it uses the chain rule from the last layer (which is the one directly connected to the loss function, i.e the function used to assess the distance between the current output of the algorithm and the expected output) to the first layer, which is the one that takes the input data. The process of descending through the gradient, i.e. adjusting the parameters of the model to go down through the loss function is called gradient descent.

2.3.1 Artificial Neural Network types

Among the existing ANNs, only the network architectures used in this thesis will be described: Long-Short Term Memory (LSTM) and Convolutional Neural Network (CNN). The difference between the perceptron previously described and these networks lies on the neuron mathematical model. The LSTM belongs to the Recurrent Neural Network (RNN) family [122], which is one of the most known types of artificial neural network. They exploit sequential data or time series data and they are usually used in speech recognition and natural language processing. A

detailed description of RNN and LSTM can be found in section 3 of chapter 4.

Compared to LSTM, CNN are more often used for classification and computer vision tasks and they better work with image, speech or audio signal inputs. The three main types of layers used by these ANNs are the convolutional, pooling and fully-connected (FC) layers. The FC layer is always used to connect all the information coming from the last hidden layer and the final output layer. The convolutional layer learns features by convolving different filters to the input sample. Each filter size should be taken smaller than the sample size to ensure a proper functioning.

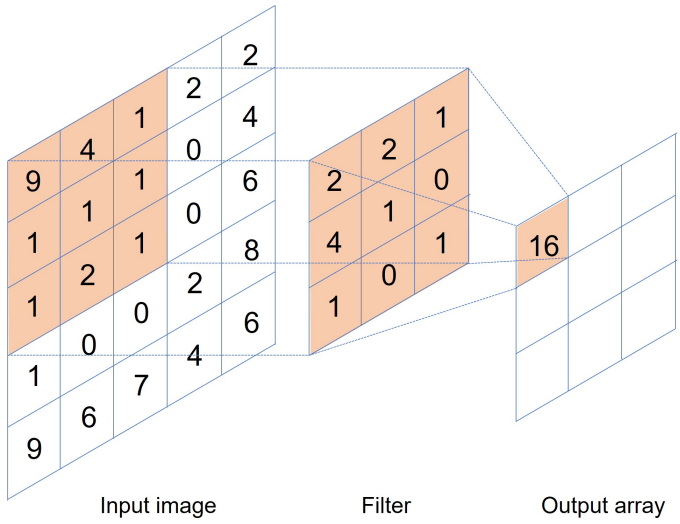

Figure 2.11: Detail of convolutional layer.

Considering the example in Figure 2.11, a specific filter is applied to an input image (both of them are described by two matrices): the filter is applied to a section of the image and the process is repeated until all the image is processed. The obtained output is known as feature map, activation map, or convolved feature. The hyper-parameters that affect most the CNN performances are the following:

- number of filters;
- stride which is the number of pixel or unit that defines the amount of movement of the filter over the image;
- padding which works extending the area of the image before being processed by the filter. If set to zero, all the pixels added in the extra area will be set to zero. This option helps the filter to analyse the image in a more accurate way.

Each convolutional layer is followed by an activation function, task usually held by the ReLU function, which introduces non-linearity to the model. This expedient is used to avoid the "vanish gradient" [123], i.e. when the gradient is extremely small preventing the weights from changing their values. The training process is the same described in the previous section.

Chapter 3

Feasibility study for the estimation of the helmet CoG accelerations

This manuscript was published in May 2022 to Transportation Research Interdisciplinary Perspectives (TRIP). Transportation Research Interdisciplinary Perspectives is a multidisciplinary journal which publishes papers concerned with any and all social science aspects of transportation.

Real time estimation of head kinematics with a good accuracy is essential to develop a methodology for a real time estimation of TBIs in crashes. Over the years several systems incorporating sensors into helmets were developed and employed to estimate head kinematics in on-field applications. However, devices, that provided the best performances, required sensors placed as close to the head as possible, but the helmet will always have its own relative motion respect to the head during an impact . Thus, the first step was to embed sensors into the helmet, far from the head. As helmet and head are not rigidly connected, but they can move quite independently, such a solution would assess the helmet kinematics rather then the head one. Is adapting existing methods to the estimation of the helmet kinematics a feasible solution? Could the assessment of the helmet kinematics contribute to a more accurate assessment of the head accelerations?

The manuscript addresses these questions, adapting the 6 Degrees of Freedom (6DOF) method to estimate the linear and rotational accelerations of the helmet Centre of Gravity (CoG) during an impact. The full-face FE model of the AGV X3000 helmet used in this chapter is the model used to carry out the analyses described in the entire thesis. The model was validated by Dainese SpA through experimental tests. The helmet was coupled to a rigid headform complying to the ECE 22.05 regulation and three different impact were reproduced in a virtual environmental. The impacts were performed at 8 m/s, i.e. the impact speed required by the Fédération Internationale de Motocyclisme (FIM) standard [124].

Results show that the modified 6DOF method had strong limitations estimating the acceleration time histories and the peak values of the rotational acceleration. Considering the results, it was considered not necessary to include parameters as friction between the headform and the helmet, fit, chin strap tension. These factors would have added further variability increasing the complexity and therefore the

estimation error. However, the accuracy was already not acceptable.

In conclusion, the results show that 6DOF method, moving the accelerometers into a helmet, can not be adapted to the estimation of the helmet kinematics. The main source of error is the helmet deformability, confirmed by the parametric study performed on the elasticity of the helmet outer shell presented in this chapter. This represents an important step for this project, as it was the turning point to the implementation of an innovative solution, as described in the next Chapter.

Transportation Research Interdisciplinary Perspectives 14 (2022) 100603

Contents lists available at ScienceDirect

Transportation Research Interdisciplinary Perspectives

journal homepage: www.elsevier.com/locate/trip

Feasibility study for the estimation of a motorcycle helmet Centre of Gravity accelerations with 6 Degrees of Freedom (6DOF) system

A. Bracali *, D. Barbani, N. Baldanzini

Department of Industrial Engineering, University of Florence, Firenze, Italy

ARTICLE INFO

Keywords:
Traumatic Brain Injuries (TBIs)
Head acceleration
Helmet acceleration
Safety
Smart helmet

ABSTRACT

Traumatic Brain Injury (TBIs) is the most frequent cause of serious and fatal road crashes. European Community has adopted an automatic emergency call system (eCall) and made it mandatory for new cars since 2018. eCall was adapted also to motorcycles, which are worldwide linked to significant mortality and trauma rates in crashes. In this context, the development of a helmet fitted with sensors, capable to estimate biomechanical crash consequences and to transmit the information over the eCall system, has the potential to reduce motorcycle crashes severity. The aim of this study is to adapt the 6 Degrees of Freedom (6DOF) method to the estimation of the linear and rotational accelerations of a helmet Centre of Gravity (CoG) during an impact and check the fitness of the method for the scope. The research was performed with virtual testing tools, reproducing three impacts of the helmet on a deformable structure at 8 m/s. The results indicate that the 6DOF estimates the peak values of the linear acceleration components with good approximation, while the peak values of the rotational acceleration components and the time histories of all the components present large errors. The 6DOF cannot be extended beyond the application to rigid bodies and another prediction method has to be identified for the accelerations of the helmet centre of gravity.

1. Introduction

Motor vehicle crashes are among the most common causes of Traumatic Brain Injuries (TBIs)-related death, behind only intentional self-harm and unintentional falls. In the USA, these three principal mechanisms of injury account respectively for 18.7%, 32.5% and 28.1% of all injuries (Centers for Disease Control and Prevention et al., 2014). A study made on 1557 TBI patients (Majdan et al., 2012) hospitalized in Austria, Slovakia, Bosnia, Croatia and Macedonia highlighted that 44% of TBIs were traffic related (car drivers, car passengers, motorcyclists, bicyclists and pedestrians). Several studies pointed out that among all road users, TBIs are mainly linked to motorcyclists with fatal and serious injuries (Chinn et al., 2001; Gibson and Thai, 2007; Aare and Holst, 2003; Meng et al.). These studies highlighted the importance of the investigation of brain trauma in motorcyclists and the development of new methods to mitigate these injuries.

Usually, TBI risk assessment is performed with criteria comprised of a biomechanical metric and an injury risk function. Most of the existing biomechanical metrics are based on head kinematics, measured with crash test dummies or instrumented headforms. Injury criteria based on linear acceleration were the first ones to be developed, e.g. Head Injury Criterion (HIC) (Versace, 1971), a metric for head injuries widely used also in Euro NCAP testing Protocols (EuroNCAP, 2017a,b). More recent studies identified the rotational acceleration as the main cause of TBIs (Gennarelli et al., 1972; Thomas et al., 1982; Melvin, 1991; Kleiven, 2006). The latter findings triggered the development of new injury criteria based on the rotational movement of the brain. The most common ones are: Generalized Acceleration Model for Brain Injury Threshold (GAMBIT) (Newman, 1986), Head Injury Power (HIP) (Newman et al., 2000) and Brain Injury criteria (BrIC) (Takhounts et al., 2003). Applications range from the estimation of the level of trauma in accident reconstruction to vehicle homologation, using sensors of anthropometric test dummies. All these criteria may also be used to estimate injuries directly in real world crashes, but their application is hampered by the technological limits in performing a precise and accurate estimation of the kinematic data (linear and rotational accelerations).

Helmets are currently widely used as protective devices to mitigate the severity of TBIs caused by an impact. Several systems incorporate micro-electromechanical systems (MEMS) inertial sensors into helmets, to measure some kinematic data and to estimate linear and rotational head accelerations at the Centre of Gravity (CoG) of the head. Head Impact Telemetry System (HITS) (Chu, 2005) was one of the earliest and most widely used device to collect kinematic data in the sport field (S.M. et al., 2005; Funk et al., 2007; Greenwald et al., 2008; Crisco

* Corresponding author.
E-mail address: andrea.bracali@unifi.it (A. Bracali).

https://doi.org/10.1016/j.trip.2022.100603
Received 30 September 2021; Received in revised form 15 February 2022; Accepted 13 April 2022
Available online 6 May 2022

et al., 2011; Beckwith et al., 2012; Rowson et al., 2012; Jadischke et al., 2013). This device is comprised of an array of 6 single-axis accelerometers, a data acquisition system, an on-board memory and a wireless transceiver; each accelerometer is embedded in a fabric padding physically attached to the helmet padding. This insert acts as a spring maintaining the essential contact between head and the accelerometers during an impact. The axes of the accelerometers are orthogonally oriented towards the head surface. Their function is to primarily measure the linear acceleration of the head, instead the rotational acceleration is estimated assuming a hypothetical pivot point in the neck.

HITS was updated, reorienting the sensing axes of the accelerometers tangentially to the head surface and adding six single-axis accelerometers for a total of twelve sensors. The new system, named 6DOF measurement device (Rowson et al., 2011), estimates both the linear and the rotational accelerations iteratively solving an optimization problem (Beckwith et al., 2007; Kimpara et al., 2011; Rowson et al., 2012). HITs and 6DOF are the most common systems for monitoring head kinematics and in both of them the sensing elements need to be in contact with the head to obtain accurate results.

More recently the gForce Tracker (GFT) (Allison et al., 2015) was developed. This system is characterized by one triaxial accelerometer and one triaxial gyroscope embedded inside a casing attached to a helmet. This technology provides only the maximum values of the resultant linear acceleration and rotational velocity obtained from a power fit regression and this data is not enough to perform an estimation of the head injuries.

Another category of devices, rigidly connected to the head but not associated to a helmet, comprises mount-guards (Miller et al., 2018; Gabler et al., 2020), earplugs (Knox, 2002) and bands (Tierney et al., 2008). These devices provide more detailed and accurate data, but they are hardly acceptable by riders (i.e. motorcycle or scooter users) for daily usage. In fact, a behavioural change would be required to adopt these devices, but previous research projects such as SAFERIDER (Bekiaris et al., 2009) or RiderScan (Delhaye and Marot, 2015) proved that riders are reluctant to change habits. The outcomes of the previously mentioned projects indicate that the utmost attention should be dedicated to the riders' acceptability during the development of a new device. In order to minimize any acceptability issue, this category of measuring devices was not further considered in this research.

Helmet based methodologies may have the potential to estimate in real time a fatal/serious injury. These devices, applied to rider helmets, can enable the real-time estimation of the trauma during a crash. However, practical considerations come into play for a widespread adoption of the existing systems. HITs and 6DOF have the necessity to ensure the constant contact of the accelerometers with the head and the utmost attention should be paid by the user while wearing the helmet: a complex usage procedure could limit the adoption of the improved helmet and the presence of the accelerometers on the accessible surface of the helmet could expose them to unintentional damage. GFT exploits sensors attached to the helmet shell, i.e. far from the head, however it has unsatisfactory average absolute errors (up to 40% if a wide variety of impact directions is considered Allison et al., 2015). To remove the drawbacks posed by the placement of the accelerometers, they could be attached to the inner of the helmet shell. The estimation of the head kinematics could be solved dividing the problem into two parts: (1) the estimation of the linear and rotational accelerations of the helmet CoG; (2) the development of a transfer function to estimate the accelerations of the head CoG from the ones of the helmet.

This study explores the possibility to use an existing technology, the 6DOF method, to perform the first step of the procedure. The 6DOF method was implemented in a finite element (FE) model of a motorcyclist helmet, instrumented with sixteen accelerometers. Since the 6DOF method was developed to estimate the acceleration of a rigid body, the main research question is: can the 6DOF method be applied to a motorcycle helmet to estimate its CoG accelerations with a +/-10% of error at each time over the entire time history? If the time history is not reproduced within a tolerable error, can the peak values of the linear and rotational accelerations be estimated with a +/- 10% error?

2. Materials and methods

2.1. Original 6DOF method

The 6DOF measurement device uses 12 accelerometers positioned in orthogonally oriented pairs at 6 different locations (Fig. 1): sensing axis of the accelerometers is tangential to the head and accelerometers are embedded in a padding to guarantee a contact with the head during impacts. In this setup the measured signals represent the head accelerations.

This method predicts both the linear and rotational head accelerations through an iterative optimization of the head equations of motion (1) during the impact:

$$\|a_i\| = \vec{r_{ai}} \cdot \vec{a} + \vec{r_{ai}} \cdot (\vec{\alpha} \times \vec{r}_i) \tag{1}$$

where $\|a_i\|$ is the acceleration measured by each accelerometer, $\vec{a}$ is the head CoG linear acceleration, $\vec{\alpha}$ is the head CoG rotational acceleration, $\vec{r}_i$ is the accelerometer location relative to the head CoG and $\vec{r_{ai}}$ is the orientation of the sensing axis of each accelerometer. The total squared error between the measured and the estimated acceleration at each location is the cost function (2) for the optimization algorithm (Rowson et al., 2011).

$$\sum_{1}^{12} \left(\|a_i\| - \left[\vec{r_{ai}} \cdot \vec{a} + \vec{r_{ai}} \cdot (\vec{\alpha} \times \vec{r}_i) \right] \right)^2 \tag{2}$$

2.2. Updated 6DOF method

The 6DOF device was implemented in a FE model of a motorcyclist helmet. Compared to the original device described in the previous section, the accelerometers were rigidly attached to the inner of the helmet shell, always in orthogonally pairs to measure the helmet accelerations. The sensing axes of the accelerometers were oriented tangentially to the helmet shell. Although the 6DOF method needs only 12 accelerometers placed in pairs at 6 locations, a higher number of locations was considered to investigate possible optimized configurations of the accelerometers, capable to minimize the estimation errors. The 16 most frequently impacted helmet sections (Fig. 2), according to the Motorcycle Accident In Depth Study (MAIDS) (MAIDS, 2009) coding scheme (Fig. 3), were selected based on in-depth crash data (Fig. 4). Each location was selected within a different helmet section. Considering the accelerometer distribution on the helmet (Fig. 2), 16 locations were considered enough for a satisfactory spatial sampling of the helmet surface.

The same cost function of the original 6DOF device was used to estimate the accelerations, but helmet CoG accelerations were used instead of head CoG accelerations in Eq. (3). The particle swarm algorithm (PSA) was applied as optimization algorithm in this study, versus the simulated annealing (SA) used in the original 6DOF formulation, since PSA has higher performance than SA (Bagaram, 2017).

The 6 pairs of accelerometers required by the 6DOF system were chosen among the 16 pairs of accelerometers available in order to obtain different configurations of accelerometers to be investigated. Two sets of accelerometer configurations were created, based on two different criteria. The selection procedure was a sequential implementation of the following steps:

1. each position was once selected as the first position for a configuration of accelerometers;
2. the remaining five positions were chosen implementing one of the two following criteria:

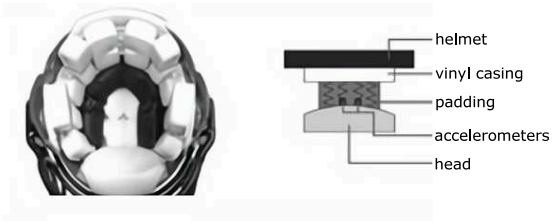

Fig. 1. 6DOF measurement device installed in a Riddell Revolution helmet (left) and a schematic of the measurement device in the helmet (right) (Rowson et al., 2011).

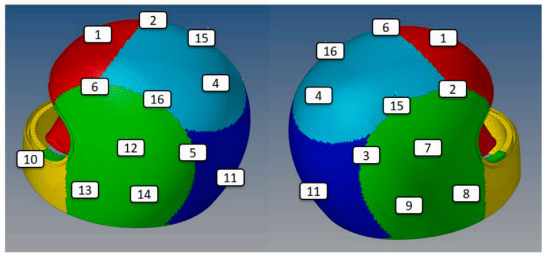

Fig. 2. Locations of the 16 orthogonally oriented accelerometer pairs.

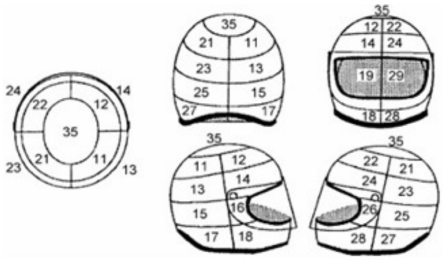

Fig. 3. Coding scheme of helmet sections used in MAIDS (MAIDS, 2009).

(a) maximizing the sum of the distances between any two positions in the configuration (criterion of maximum dispersion);
(b) minimizing the mean square error of the distance between any two accelerometers of the configuration referred to the mean distance among positions in the configuration (criterion of the uniform distribution).

The procedure was defined to systematically position the accelerometers on the helmet shell, to better capture its kinematic. Each configuration had to differ from any previously defined one in order to be included in the study. Thirty-two configurations were created and investigated applying the 6DOF method to find the best performing accelerometer arrangement.

2.3. FE models

A full-face model of helmet (AGV X 3000, size 58/59), certified both DOT FMVSS 218 (DOT-FMVSS-218, 1984) and UNECE 22.05 (ECE22.05, 2002), was used for this study. LS-Dyna solver, version 971 (Hallquist et al., 2006), was used to perform impact simulations. The helmet model, provided by Dainese SpA (Cernicchi et al., 2008), consists of an energy-absorbing liner, an outer shell and a chin strap: shell elements were used for the external polycarbonate shell (material model: MAT058), while solid elements for the expanded polystyrene of the energy-absorbing liner (material model: MAT075). The helmet CoG was connected with an interpolation constraint to 10,000 randomly selected nodes belonging to the shell surface. This modelling of the helmet CoG allowed to measure the reference accelerations while not stiffening the helmet shell. In the impacts, the helmet was coupled with an appropriate rigid headform model.

Three different impact configurations of the helmet on a flat surface were reproduced (Fig. 5). In Configuration 1 the impact point was located on the top of the helmet, while in Configuration 2 the impact point was on the left side of the helmet. These impact configurations were selected to reproduce 2 out of the 5 impact conditions (P and X points) required by the ECE 22.05 standard (ECE22.05, 2002). In the third configuration the impact point was chosen not aligned with the sagittal, transversal or horizontal plane, and the velocity vector was defined to reproduce an oblique impact. In each configuration the helmet impacted the surface at 8 m/s.

The 6DOF algorithm was developed assuming rigid body dynamics, but both the head and helmet are deformable bodies. The helmet shell is a laminated composite, modelled with MAT58 material. To investigate the influence of the helmet deformability on the estimations of the 6DOF algorithm, the elastic Young Modulus of the shell material was progressively increased in a sequence of simulations to approximate the condition of infinitely rigid body. This approach was implemented for the second impact configuration, which presented the largest errors in this study.

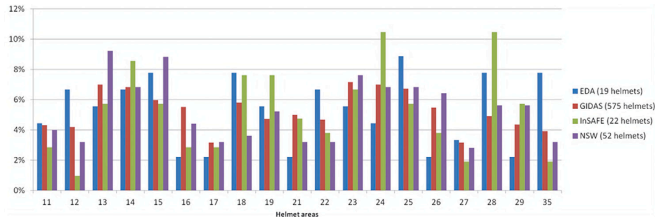

Fig. 4. Distribution of helmet contact sections (EDA, GIDAS, InSAFE, NSW datasets) (Pioneers, 2020) using the MAIDS helmet sections scheme (MAIDS, 2009).

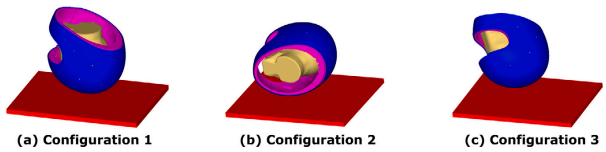

Fig. 5. Impact configurations.

The following metrics were considered to evaluate the error of the computed acceleration: percentage error for linear and angular peak both for resultant and component accelerations; mean and maximum absolute error for the time histories of linear and angular accelerations, both for resultant and each component. In all calculations, the FE helmet CoG accelerations, obtained from the simulations, were taken as reference signals.

Eq. (3) was used to evaluate the mean relative error: ϵ_{mean} is the mean relative error, n is the number of discrete data points, $6dof$ is the predicted acceleration by the 6DOF method, HF is the reference signal, HF_{max} is the maximum absolute value of the reference signal. A specific HF_{max} was determined for each component and for the resultant of both linear and rotational acceleration. Eq. (4) was used to evaluate the maximum relative error; where ϵ_{max} is the maximum relative error. Eq. (5) and (6) were used to calculate the peak relative positive and negative errors: ϵ_{peak-} is the negative one and ϵ_{peak+} is the positive one; $6dof_{(-)}$ is the negative peak value for the predicted acceleration and $HF_{(-)}$ for the real one (5). Instead, the positive peaks are specified by the plus sign (6).

$$\epsilon_{mean} = \frac{1}{n}\sum \frac{6dof_i - HF_i}{HF_{max}} \tag{3}$$

$$\epsilon_{max} = max\left(\frac{6dof_i - HF_i}{HF_{max}}\right) \tag{4}$$

$$\epsilon_{peak(-)} = \frac{6dof_{(-)} - HF_{(-)}}{HF_{max}} \tag{5}$$

$$\epsilon_{peak(+)} = \frac{6dof_{(+)} - HF_{(+)}}{HF_{max}} \tag{6}$$

For each configuration of accelerometers, average ϵ_{mean} and ϵ_{peak+} over the three impact configurations were computed for both the linear and rotational resultant accelerations. The accelerometer configuration that minimized both the errors was selected as the best one. Specifically, ϵ_{mean} was used to understand if this method was suitable to reproduce the entire time history of the acceleration of the helmet CoG; instead, ϵ_{peak+} gave an estimation of the method performances in the prediction of peak values.

3. Results

The first step was to identify and select the best relative position of accelerometers among the 32 configurations defined in the previous section. According to the results in Tables 1 and 2, the configurations of accelerometers obtained maximizing the distance between each accelerometer locations are characterized by lower values for both the average ϵ_{mean}, ϵ_{max} and average ϵ_{peak+}. Among these configurations, ϵ_{mean} has similar values both for the resultant linear acceleration and the resultant rotational acceleration (Table 1). Moreover, most of these configurations have average ϵ_{peak+} below 5% for the resultant linear acceleration. As the average ϵ_{peak+} for the resultant rotational acceleration and ϵ_{max} for both the linear and rotational accelerations are the error metrics with the largest values, the best configuration had to minimize these parameters. The selected configuration (#4) is also characterized by the best value of the average ϵ_{mean} both for the resultant linear and rotational accelerations. It includes the sensors located at the positions 1-4-8-10-11-13 (Fig. 2). The configuration was used for the performance assessment of the 6DOF method in the estimation of the helmet CoG accelerations.

For each configuration the comparison was performed at component level and the related errors metrics were computed and analysed. In the first configuration (Figs. 6 and 7) the most relevant discrepancies occur in a_x and a_y linear accelerations and in α_x and α_z rotational accelerations. The impact kinematics is mainly along the Z axis and around the Y axis. Therefore, a_z and α_y are the components with larger amplitude and a good qualitative match can be observed. The errors reported in Table 3 confirm the qualitative assessment: the positive and negative peak values of the linear acceleration along the Z axis and the resultant amplitude are estimated almost perfectly (maximum error 1%). Both the a_z and the resultant linear acceleration are characterized by larger values of ϵ_{max} (respectively 16% and 17%). In the graphs of Figs. 6 and 7, components (a_z and α_y), the differences between the reference and predicted data increase shortly after the main peak (starting from 0.015 s). Instead, the component along the X axis is characterized by the worst estimation as underlined by the maximum relative error equal to 23% and the negative and positive peak errors equal to 12% and 9%.

Similar results were obtained for the rotational acceleration, although errors are larger than for the linear acceleration: the main component (α_y) and the resultant are characterized by the smallest peak estimation errors. Instead, the resultant rotational acceleration has the worst ϵ_{max} equal to 50% due to the high ϵ_{max} values of the three components. Without the presence of a marked peak in the acceleration

Table 1
Average ϵ_{mean}, ϵ_{max} and ϵ_{peak+} over the three impact configurations as a function of the 16 accelerometer configurations obtained maximizing the distance between each accelerometer location.

Error Type	*Acceleration Type*	*Accelerometer configurations*															
		1	*2*	*3*	*4*	*5*	*6*	*7*	*8*	*9*	*10*	*11*	*12*	*13*	*14*	*15*	*16*
ϵ_{mean} [%]	*Linear*	5.06	5.67	5.17	4.49	4.95	4.22	5.03	5.13	4.62	4.90	4.41	4.15	5.17	5.42	4.65	5.11
	Rotational	12.1	14.0	14.0	12.2	14.5	13.7	14.0	14.4	14.2	13.4	13.2	12.8	13.7	14.5	13.2	14.5
ϵ_{max} [%]	*Linear*	40.8	37.2	42.7	42.3	42.5	32.2	31.0	40.1	39.1	39.4	41.7	35.7	35.5	44.8	36.3	31.4
	Rotational	93.5	125	101	83.1	117	120	110	125	93.3	103	100	95.9	107	116	93.0	115
ϵ_{peak+} [%]	*Linear*	9.29	3.91	1.32	3.25	5.00	2.37	13.2	5.49	3.05	13.5	1.97	1.70	8.64	9.87	4.46	2.91
	Rotational	40.3	59.0	34.2	30.7	45.3	48.0	60.5	49.0	44.3	45.5	34.4	32.4	61.1	46.1	34.1	58.5

Table 2
Average ϵ_{mean}, ϵ_{max} end ϵ_{peak+} over the three impact configurations as a function of the 16 accelerometer configurations obtained minimizing the mean square error of the mean distance between each accelerometer location.

Error Type	*Acceleration Type*	*Accelerometer configurations*															
		1	*2*	*3*	*4*	*5*	*6*	*7*	*8*	*9*	*10*	*11*	*12*	*13*	*14*	*15*	*16*
ϵ_{mean} [%]	*Linear*	11.3	10.5	10.5	8.24	9.42	10.6	10.8	11.7	10.6	9.96	10.5	9.29	7.08	10.1	10.0	10.7
	Rotational	33.0	34.5	33.1	31.6	30.7	31.1	33.7	32.9	33.3	31.1	32.3	31.0	25.4	32.3	33.9	28.2
ϵ_{max} [%]	*Linear*	74.6	67.1	72.2	42.3	63.3	72.9	80.2	87.2	79.6	68.9	65.7	60.6	39.6	71.0	62.4	88.1
	Rotational	203	234	212	234	212	189	198	197	191	205	202	218	185	219	228	178
ϵ_{peak+} [%]	*Linear*	27.8	26.1	31.4	7.99	15.7	26.1	39.1	45.9	39.2	23.1	19.7	15.8	13.7	24.8	13.1	44.2
	Rotational	139	171	151	170	147	126	166	129	157	140	137	153	119	154	163	104

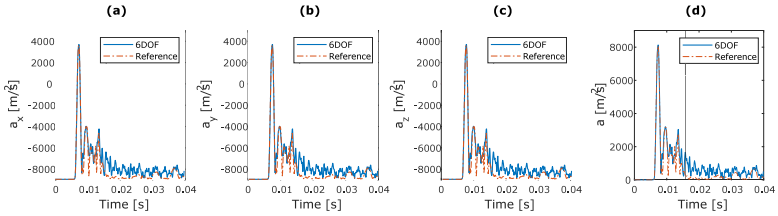

Fig. 6. Configuration 1: response of the simulated and 6DOF estimated linear accelerations of the helmet CoG (see also Table 3): (a) x axis component, (b) y axis component, (c) z axis component, (d) resultant acceleration. The vertical line indicates the time corresponding to ϵ_{max}.

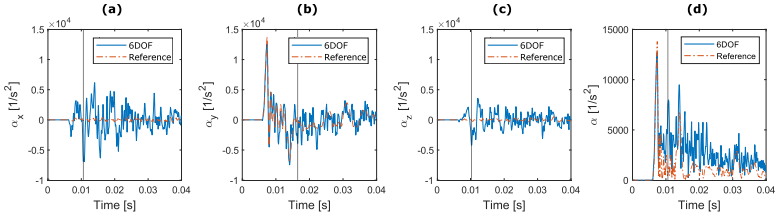

Fig. 7. Configuration 1: response of the simulated and 6DOF estimated rotational accelerations of the helmet CoG (see also Table 3): (a) x axis component, (b) y axis component, (c) z axis component, (d) resultant acceleration. The vertical line indicates the time corresponding to ϵ_{max}.

Table 3
Configuration 1: mean and maximum relative errors, positive and negative peak errors for the helmet accelerations.

Error type	Linear Acceleration				Rotational Acceleration			
	a_x	a_y	a_z	Resultant	α_x	α_y	α_z	Resultant
ϵ_{mean} [%]	3.67	0.89	3.41	4.01	10.4	6.98	5.57	10.2
ϵ_{max} [%]	22.6	6.57	15.5	17.3	48.7	30.4	29.9	49.7
ϵ_{peak+} [%]	8.51	3.81	0.82	0.60	40.4	8.80	22.3	8.05
ϵ_{peak-} [%]	11.8	5.50	0.41	/	46.6	4.64	26.8	/

Note: / is used when the parameter is not applicable.

signal, the 6DOF algorithm was not able to properly predict both α_x and α_z (Fig. 7).

In the second configuration, the helmet velocity was aligned with the Y axis and the helmet impacted the surface on the right side. The

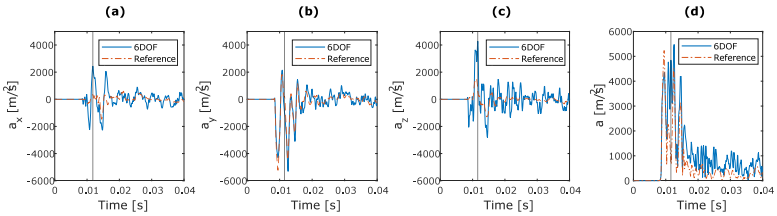

Fig. 8. Configuration 2: response of the simulated and 6DOF estimated linear accelerations of the helmet CoG (see also Table 4): (a) x axis component, (b) y axis component, (c) z axis component, (d) resultant acceleration. The vertical line indicates the time corresponding to ϵ_{max}.

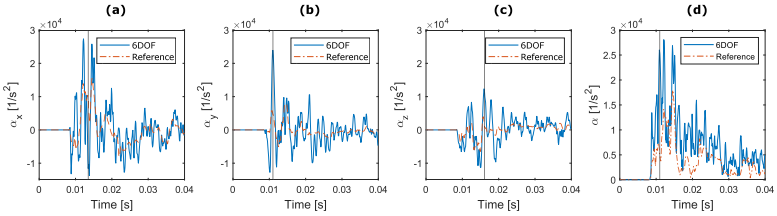

Fig. 9. Configuration 2: response of the simulated and 6DOF estimated rotational accelerations of the helmet CoG (see also Table 4): (a) x axis component, (b) y axis component, (c) z axis component, (d) resultant acceleration. The vertical line indicates the time corresponding to ϵ_{max}.

Table 4
Configuration 2: mean and maximum relative errors, positive and negative peak errors for the helmet accelerations.

Error type [%]	Linear Acceleration				Rotational Acceleration			
	a_x	a_y	a_z	Resultant	α_x	α_y	α_z	Resultant
ϵ_{mean} [%]	6.34	4.73	8.46	8.63	17.8	13.6	10.6	18.3
ϵ_{max} [%]	39.9	23.0	68.1	77.7	115	107	57.7	113
ϵ_{peak+} [%]	34.9	5.94	51.9	4.48	65.7	88.4	46.7	56.2
ϵ_{peak-} [%]	15.2	1.29	29.2	/	31.2	42.7	27.2	/

Note: / is used when the parameter is not applicable.

6DOF estimations show more diffuse errors, but the linear acceleration along the Y axis has been correctly estimated (Fig. 8). All the predicted components of the rotational acceleration differ from the reference curves (Fig. 9). Overall, the curves predicted by the 6DOF system tend to overestimate the local maxima and minima of the acceleration components. The errors confirm these findings (Table 4). a_y is the only component of acceleration predicted with acceptable errors: 6% and 1% for ϵ_{peak+} and ϵ_{peak-} respectively, while ϵ_{mean} is 5%. The other components of the linear acceleration have errors up to 52% in the estimation of the positive peak value and 29% for the negative one of a_z. The resultant linear acceleration shows a small error on the peak value ($\epsilon_{peak+} = 4\%$), although the time history does not reproduce the reference curve. The peak value of the target acceleration occurred at $t_1 = 0.009$ s, instead in the acceleration reproduced with the 6DOF the peak occurred at $t_2 = 0.012$ s. All the estimated rotational acceleration components show significant errors: up to 88% in the estimation of the positive peak value of α_y and ϵ_{mean} in the range 11%–17%. The resultant rotational acceleration has similar results for ϵ_{mean} (18%) and ϵ_{peak+} (56%). In Fig. 9 the rotational accelerations are compared. The average mean and maximum relative errors are 15% ± 4% and 98% ± 30% respectively; while the average positive peak error is 64% ± 21% and the average negative peak error is 34% ± 8%. The whole results are reported in the Table 4.

In the third configuration a generic impact, with randomly selected direction of the helmet velocity and helmet orientation with respect to the plate, was reproduced. The linear and rotational accelerations, components and resultants, are reported in Figs. 10 and 11. Y and Z components of the linear accelerations have similar amplitudes and they show a good agreement with the reference signals. X component has a smaller amplitude range, but it shows a comparable qualitative match between 6DOF and reference curves. Results reported in Table 1 confirm the previous analysis: the ϵ_{mean} does not exceed 4% for each component. Peak errors show that a_x and a_y have the best negative (ϵ_{peak-}), and positive (ϵ_{peak+}) peak predictions. The quality of the component estimation also affected the resultant estimation as demonstrated by ϵ_{mean} and ϵ_{peak+}, respectively equal to 4% and 5%.

The prediction of the rotational accelerations is still affected by a greater error than the linear acceleration (Table 5): ϵ_{mean} never falls below 10% and errors up to 70% and 73% affect respectively the positive and negative peak estimations. The comparison between the predicted and target rotational accelerations is shown in Fig. 11. 6DOF curves tend to overestimate local minima and maxima of the real acceleration over the entire time history, leading to unacceptable errors in estimation as discussed above.

The 6DOF measurement device was developed to be used with substantially rigid body, but in this study the accelerometers were attached to the helmet shell, a deformable body. The impact configuration with the prediction performances of the worst accelerations, i.e. the second configuration, was selected as test case to verify how deformability affected the results. Increments from 10 to 10^4 times of the helmet shell Young modulus were implemented to change the deformability of the body up to an extremely stiff shell. Results shown in Table 6

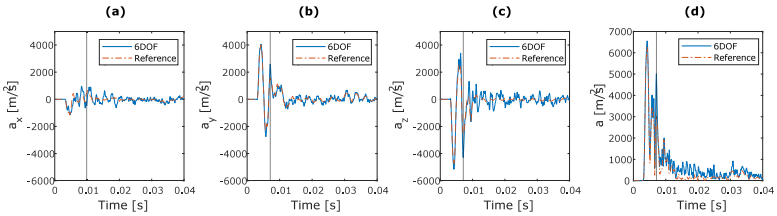

Fig. 10. Configuration 3: response of the simulated and 6DOF estimated linear accelerations of the helmet CoG (see also Table 5): (a) x axis component, (b) y axis component, (c) z axis component, (d) resultant acceleration. The vertical line indicates the time corresponding to ϵ_{max}.

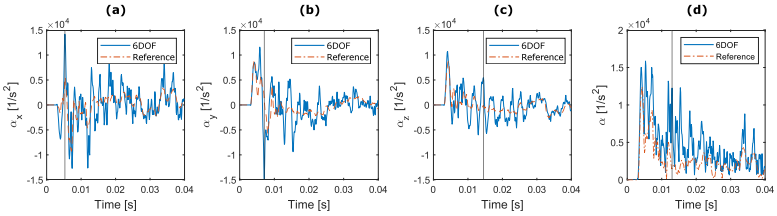

Fig. 11. Configuration 3: response of the simulated and 6DOF estimated rotational accelerations of the helmet CoG (see also Table 5): (a) x axis component, (b) y axis component, (c) z axis component, (d) resultant acceleration. The vertical line indicates the time corresponding to ϵ_{max}.

Table 5
Configuration 3: mean and maximum relative errors, positive and negative peak errors for the helmet accelerations.

Error type [%]	Linear Acceleration				Rotational Acceleration			
	a_x	a_y	a_z	Resultant	α_x	α_y	α_z	Resultant
ϵ_{mean} [%]	2.91	1.64	4.04	3.82	15.2	14.4	11.0	17.1
ϵ_{max} [%]	14.4	16.5	27.2	31.9	72.4	129	45.0	86.5
ϵ_{peak+} [%]	4.74	0.89	12.3	4.68	69.9	21.2	16.2	27.8
ϵ_{peak-} [%]	0.75	7.14	6.86	/	27.5	73.4	27.6	/

Note: / is used when the parameter is not applicable.

highlighted a decreasing trend in the four error metrics as the stiffness of the helmet shell increased: ϵ_{mean} decreased in the range 1%–2% and 5%–6% respectively for the linear and rotational accelerations; ϵ_{max} showed the greatest improvement (e.g. the related error of α_x decreased from 115% to 32%); both ϵ_{peak+} and ϵ_{peak-} dropped below 15%.

4. Discussion

eCall is a pan-European system for the automatic emergency call in case of road crashes. Initially developed for cars, eCall was extended to other vehicles, including Powered Two-Wheelers (PTWs), within the I_Heero project. Currently BMW is offering the system on its motorcycles but also aftermarket systems are available. This technology on PTWs enables new possibilities for early crash detection and emergency treatment of riders. In fact, riders are not protected by an outer structure as in cars, but the helmet use is mandatory in several countries. Helmet could be turned into a sensing protective equipment, capable to improve the crash detection (currently performed by on-board sensors) but also to integrate a real time estimation of head injuries into the activation criterion of the eCall. The latter data could also be transmitted to the rescue team and enable a more timely and effective intervention. TBIs are overrepresented among riders (Gibson and Thai, 2007), and they are one of the most severe and dangerous consequences of an impact. Detection and timely treatment are key to minimize consequences (Tepas III. et al., 2009).

The estimation of head injuries requires appropriate knowledge of the head kinematics during the impact. Measurement systems embedded into the helmets could provide adequate data to perform real time estimation of the injuries, but new helmets should require to the end users the same level of usage expertise than the current marketed solutions. As the 6DOF method has strict requirements for the positioning of sensors (i.e. in contact with the head), there is the need to investigate possible changes to sensors layout and the implications on the accuracy and precision of the derived data. In the current study the sensors were attached to the inner side of the outer shell of the helmet.

From 16 pairs of accelerometers, 32 possible configurations of the sensors were defined and simulated in the three impact configurations, representative of crash conditions both in terms of impact points and velocity. The accelerometer configurations obtained with the maximization of the distance between accelerometer locations (Table 1) led to better accuracy than minimizing the square error referred to the mean distance (Table 2). On the contrary, the accelerometer configurations generated with the same criterion had similar performances and none of them was clearly outperforming the other ones. For instance, the sixteen accelerometer configurations in Table 1 have comparable values of ϵ_{mean} both for the linear and rotational accelerations. Similar remarks apply to ϵ_{max}, except that some configurations (#2, #6, #8) have noticeably higher values. The results demonstrate the strong effect of the criterion for the sensor distribution on the prediction accuracy of CoG accelerations with flexible bodies, and negligible differences among the accelerometer configurations generated with

Table 6
Increasing Young modulus of the outer shell: mean and maximum relative errors, positive and negative peak errors for the helmet accelerations.

Error type	Configuration	Linear Acceleration				Rotational Acceleration			
		a_x	a_y	a_z	Resultant	α_x	α_y	α_z	Resultant
ε_{mean} [%]	E	6.34	4.73	8.46	8.63	17.8	13.6	10.6	18.3
	$E*10$	4.52	2.51	4.15	4.58	6.37	5.48	5.85	6.85
	$E*10^2$	3.37	2.45	3.72	3.87	11.3	8.10	9.23	11.3
	$E*10^3$	2.13	1.92	2.98	3.27	7.98	5.64	7.23	7.45
	$E*10^4$	1.18	1.20	1.80	1.88	6.46	4.51	4.89	5.00
ε_{max} [%]	E	40.0	23.0	68.1	77.7	115	107	57.7	113
	$E*10$	34.4	14.6	33.0	34.6	60.9	46.3	37.3	45.9
	$E*10^2$	19.3	12.7	36.9	20.2	56.6	52.7	54.8	54.0
	$E*10^3$	11.2	10.0	28.7	14.8	37.3	30.3	60.1	45.9
	$E*10^4$	5.14	5.49	13.0	7.65	32.4	26.1	25.9	25.5
ε_{peak+} [%]	E	34.9	5.93	51.9	4.49	65.7	88.4	46.7	56.2
	$E*10$	23.8	12.2	22.3	12.0	5.14	27.4	26.6	17.3
	$E*10^2$	8.60	4.44	18.0	6.38	30.9	22.8	28.1	27.4
	$E*10^3$	8.34	1.43	28.3	2.09	32.7	13.3	17.3	30.5
	$E*10^4$	0.67	4.54	12.2	5.92	0.39	10.2	12.1	8.17
ε_{peak-} [%]	E	15.2	1.29	29.2	/	31.1	42.7	27.2	/
	$E*10$	30.3	14.6	16.1	/	23.6	34.4	21.4	/
	$E*10^2$	15.4	9.52	21.7	/	31.6	30.2	32.3	/
	$E*10^3$	5.42	2.12	13.0	/	19.0	18.2	17.7	/
	$E*10^4$	3.58	4.62	5.55	/	6.62	14.8	11.1	/

Note: / is used when the parameter is not applicable.

the same criterion. The observed differences may vanish if the accelerometer configurations would be tested on a larger set of impact configurations. Such a test should be conducted before accepting the possibility to successfully perform an optimization of the accelerometer distribution within a specific distribution criterion. This activity was not developed within the present research, since the main focus was on the applicability of the 6DOF method to flexible bodies. Nonetheless the following research activities were developed with the best accelerometer configuration, i.e. #4 in Table 1, as it minimized the greatest number of errors metrics (i.e. 4 out of 6).

The system, with the selected accelerometer configuration, was tested in three different impact configurations. The results show a good capability in the assessment of linear acceleration peak values: in all configurations the peak error on the resultant of the linear acceleration never exceeded 5%, although in the second configuration the peak of the 6DOF prediction was delayed compared to the reference signal. The latter result is a consequence of higher peak errors in the components: maximum peak error exceeded 50% in this configuration, while it reached 12% in the other two configurations. In general, the 6DOF prediction of the linear accelerations overestimated the local minima and maxima in each impact configuration (Tables 3–5). This trend was extremely evident in the second impact configuration time histories of the x and z components as well as for the resultant (Fig. 8). The predicted signals were good in proximity of the peaks of the resultant for the configurations 1 and 3 as well as of the components with the largest amplitude for all impact configurations, but they failed to match the reference signals over the entire time range.

With reference to the rotational acceleration, the results highlighted the general difficulty of the method to correctly reproduce the entire time history of the in each component. Specifically, the predicted rotational accelerations tended to overestimate the local minima and maxima as for the linear accelerations. Mean errors were never below 6% in any impact configuration, with a maximum of 18% in the estimation of the resultant rotational acceleration in the second impact configuration, and the predicted values of the negative and positive peaks had errors up to 88%.

The results demonstrated an extremely limited predictive capability for the 6DOF method applied to a flexible body, already in a limited set of impact configurations. The errors were not in line with the desired accuracy and they did not justify further investigation. In fact, this research aimed to verify the general applicability of the 6DOF method to predict the CoG accelerations of a flexible body. The parametric study on the elasticity of the outer shell, confirmed that the main source of error is the body deformability.

An intrinsic limitation applies to this study. Namely the impossibility of carrying out an experimental verification, as the CoG is not a physical point of the helmet and no measurement of its accelerations can be performed. A secondary possible limitation could be the use of a single helmet model. Nonetheless the feasibility study is not affected by this limitation, as more helmets would be necessary to confirm a positive estimation capability of the 6DOF method but a single helmet is sufficient to prove the limitations, if a general application of the method is desired.

This research showed that a different method has to be identified for the prediction of the CoG accelerations. Such a method should be capable of handling the flexibility of the body and, possibly, it should also integrate the transfer function from the CoG accelerations of the helmet to the head accelerations.

5. Conclusions

The study focused on the investigation of the 6DOF method to estimate the acceleration of a motorcyclists' helmet centre of gravity. Three different configurations of a helmet, coupled with a standard rigid head and impacting on a deformable plate, were reproduced in a virtual environmental. The FE model of the helmet was integrated with 32 accelerometers in orthogonally pairs at 16 different locations on its outer shell.

Since the 6DOF needed only 6 pairs of accelerometers, a preliminary study to identify the best configuration of accelerometers was performed. The criterion used to generate the accelerometer configurations influenced the precision of the estimated results, but there were limited differences among the best configurations based on the same criterion. The best configuration was used for a detailed analysis and comparison of the predicted signals with the reference ones.

Results suggested that the 6DOF capability to estimate linear accelerations depended on the impact configuration and on the desired outcome. If the peak of the resultant linear acceleration could suffice, the investigation on the 6DOF applicability to flexible bodies could be further extended. If the prediction of the entire acceleration signal

is sought, the 6DOF method has severe limitations, especially for the rotational accelerations.

Future works should consider a totally novel method capable of taking into account the flexibility of the body, which is the greatest limit of technologies integrated into the helmet. Otherwise, a novel technology able to directly estimate the head CoG accelerations using sensors attached to the helmet surface should be deepened.

CRediT authorship contribution statement

A. Bracali: Conceptualization, Methodology, Software, Formal analysis, Data curation, Writing – original draft, Writing – review & editing. **D. Barbani:** Conceptualization, Methodology, Writing – review & editing, Supervision. **N. Baldanzini:** Conceptualization, Methodology, Writing – review & editing, Supervision.

Declaration of competing interest

The authors declare that they have no known competing financial interests or personal relationships that could have appeared to influence the work reported in this paper.

Acknowledgement

Authors acknowledge the Dainese SpA for the support in FE modelling.

References

Aare, M., Holst, H., 2003. Injuries from motorcycle- and moped crashes in Sweden from 1987 to 1999. Inj. Control Saf. Promot. 10 (3), 131–138.

Allison, M.A., Kang, Y.S., Maltese, M.R., Bolte, J.H., Arbogast, K.B., 2015. Measurement of hybrid III head impact kinematics using an accelerometer and gyroscope system in ice hockey helmets. Ann. Biomed. Eng. 43 (8), 1896–1906. http://dx.doi.org/10.1007/s10439-014-1197-z.

Bagaram, M., 2017. Comparison of Simulated Annealing and Particle Swarm Optimization on Reliability-Redundancy Problem (Ph.D. thesis). University Of Washington.

Beckwith, J.G., Chu, J.J., Greenwald, R.M., 2007. Validation of a noninvasive system for measuring head acceleration for use during boxing competition. J. Appl. Biomech. 23 (3), 238–244. http://dx.doi.org/10.1123/jab.23.3.238.

Beckwith, J.G., Greenwald, R.M., Chu, J.J., 2012. Measuring head kinematics in football: Correlation between the head impact telemetry system and hybrid III headform. Ann. Biomed. Eng. 40 (1), 237–248. http://dx.doi.org/10.1007/s10439-011-0422-2.

Bekiaris, E.D., Spadoni, A., Nikolaou, S.I., 2009. SAFERIDER project: new safety and comfort in powered two wheelers. In: 2009 2nd Conference on Human System Interactions. IEEE, pp. 600–602.

Centers for Disease Control and Prevention, et al., 2014. Traumatic brain injury in the United States: Fact sheet. Washington, DC: Centers for Disease Control and Prevention.

Cernicchi, A., Galvanetto, U., Iannucci, L., 2008. Virtual modelling of safety helmets: practical problems. Int. J. Crashworth. 13 (4), 451–467.

Chinn, B., Canaple, B., Derler, S., Doyle, D., Otte, D., Schuller, E., Willinger, R., 2001. Cost 327 motorcycle safety helmets. European Commission, Directorate General for Energy and Transport.

Chu, J.J., 2005. An algorithm for estimating acceleration magnitude and impact location using multiple nonorthogonal single-axis accelerometers. J. Biomech. Eng. 126 (6), 849. http://dx.doi.org/10.1115/1.1824135.

Crisco, J.J., Wilcox, B.J., Beckwith, J.G., Chu, J.J., Duhaime, A.C., Rowson, S., Duma, S.M., Maerlender, A.C., McAllister, T.W., Greenwald, R.M., 2011. Head impact exposure in collegiate football players. J. Biomech. 44 (15), 2673–2678. http://dx.doi.org/10.1016/j.jbiomech.2011.08.003.

Delhaye, A., Marot, L., 2015. A European scanning tour for motorcycling safety, final report of the EC/MOVE/C4 project RIDERSCAN.

DOT-FMVSS-218, 1984. Laboratory procedure for motorcycle helmet testing - federal motor vehicle safety standard no. 218. National Highway Traffic Safety Administration, Department of Transportation U.S..

ECE22.05, 2002. Uniform provisions concerning the approval of protective helmets and of their visors for drivers and passengers.

EuroNCAP, 2017a. European New car assessment programme (Euro NCAP) assessment protocol adult occupant protection. November.

EuroNCAP, 2017b. European New car assessment programme (Euro NCAP) pedestrian testing protocol. November.

Funk, J.R., Duma, S.M., Manoogian, S.J., Rowson, S., 2007. Biomechanical risk estimates for mild traumatic brain injury. J. Chem. Inf. Model. 51 (9), 343–361. http://dx.doi.org/10.1017/CBO9781107415324.004.

Gabler, L.F., Huddleston, S.H., Dau, N.Z., Lessley, D.J., Arbogast, K.B., Thompson, X., Resch, J.E., Crandall, J.R., 2020. On-field performance of an instrumented mouthguard for detecting head impacts in American football. Ann. Biomed. Eng. 48 (11), 2599–2612.

Gennarelli, T.A., Thibault, L.E., Ommaya, A.K., 1972. Pathophysiologic Responses to Rotational and Translational Accelerations of the Head. SAE Technical Papers, pp. 296–308. http://dx.doi.org/10.4271/720970.

Gibson, T., Thai, K., 2007. Helmet Protection Against Basilar Skull Fracture. ATSB Research and Analysis Report, Citeseer.

Greenwald, R.M., Joseph, T.G., Chu, J.J., Crisco, J.J., 2008. Head impact severity measures for evaluating brain injury risk exposure. pp. 789–798. http://dx.doi.org/10.1227/01.NEU.0000311244.05104.96, 62, 4.

Hallquist, J.O., et al., 2006. LS-DYNA theory manual. Livermore Softw. Technol. Corp. 3, 25–31.

Jadischke, R., Viano, D.C., Dau, N., King, A.I., McCarthy, J., 2013. On the accuracy of the head impact telemetry (hit) system used in football helmets. J. Biomech. 46 (13), 2310–2315. http://dx.doi.org/10.1016/j.jbiomech.2013.05.030.

Kimpara, H., Nakahira, Y., Iwamoto, M., 2011. Head injury prediction methods based on 6 degree of freedom head acceleration measurements during impact. Int. J. Automot. Eng. 2 (2), 13–19. http://dx.doi.org/10.20485/jsaeijae.2.2_13.

Kleiven, S., 2006. Evaluation of head injury criteria using a finite element model validated against experiments on localized brain motion, intracerebral acceleration, and intracranial pressure. Int. J. Crashworthiness 11 (1), 65–79. http://dx.doi.org/10.1533/ijcr.2005.0384.

Knox, T., 2002. Use of Instrumented Earplugs to Measure Driver Head Accelerations. SAE Technical Paper.

MAIDS, 2009. In-Depth Investigations of Accidents Involving Powered Two-Wheelers. Final Report 2.0 [Report]. - [s.l.], Association of European Motorcycle Manufacturers (ACEM.

Majdan, M., Mauritz, W., Wilbacher, I., Janciak, I., Brazinova, A., Rusnak, M., Leitgeb, J., 2012. Traumatic brain injuries caused by traffic accidents in five European countries: outcome and public health consequences. Eur. J. Public Health 23 (4), 682–687. http://dx.doi.org/10.1093/eurpub/cks074.

Melvin, J., 1991. Review of biomechanical impact response and injury in the automotive environment. Transportation Research Circular.

Meng, S., Cernicchi, A., Kleiven, S., Halldin, P., 2020. High-speed helmeted head impacts in motorcycling: A computational study.

Miller, L.E., Kuo, C., Wu, L.C., Urban, J.E., Camarillo, D.B., Stitzel, J.D., 2018. Validation of a custom instrumented retainer form factor for measuring linear and angular head impact kinematics. J. Biomech. Eng. 140 (5).

Newman, J.A., 1986. A generalized model for brain injury threshold. In: Proceedings of International Conference on the Biomechanics of Impact, 1986. pp. 121–131.

Newman, J.A., Shewchenko, N., Welbourne, E., 2000. A proposed new biomechanical head injury assessment function -the maximum power index. Reprinted from: Stapp Car Crash J. 44 (724).

Pioneers, 2020. D1.1 powered two-wheelers – road traffic accidents scearios and common injuries, protective innovations of new equipment for enhanced rider safety.

Rowson, S., Beckwith, J.G., Chu, J.J., Leonard, D.S., Greenwald, R.M., Duma, S.M., 2011. A six degree of freedom head acceleration measurement device for use in football. J. Appl. Biomech. 27 (1), 8–14.

Rowson, S., Duma, S.M., Beckwith, J.G., Chu, J.J., Greenwald, R.M., Crisco, J.J., Brolinson, P.G., Duhaime, A.C., McAllister, T.W., Maerlender, A.C., 2012. Rotational head kinematics in football impacts: An injury risk function for concussion. Ann. Biomed. Eng. 40, http://dx.doi.org/10.1007/s10439-011-0392-4.

S.M., D., S.J., M., W.R., B., P.G., B., M.W., G., J.J., D., R.M., G., J.J., C., J.J., C., 2005. Analysis of real-time head accelerations in collegiate football players. Clin. J. Sport Med. 15 (1), 3–8.

Takhounts, E.G., Eppinger, R.H., Campbell, J.Q., Tannous, R.E., Power, E.D., Shook, L.S., 2003. On the Development of the SIMon Finite Element Head Model. SAE Technical Papers, 2003-October, October, pp. 107–133. http://dx.doi.org/10.4271/2003-22-0007.

Tepas III., J.J., Leaphart, C.L., Pieper, P., Beaulieu, C.L., Spierre, L.R., Tuten, J.D., Celso, B.G., 2009. The effect of delay in rehabilitation on outcome of severe traumatic brain injury. J. Pediatr. Surg. 44 (2), 368–372.

Thomas, A., Gennarelli, M., Lawrence, E., Thibault, S.D., 1982. Biomechanics of Acute Subdural Hematoma. J. Trauma. 680–686.

Tierney, R.T., Higgins, M., Caswell, S.V., Brady, J., McHardy, K., Driban, J.B., Darvish, K., 2008. Sex differences in head acceleration during heading while wearing soccer headgear. J. Athl. Train. 43 (6), 578–584.

Versace, J., 1971. A review of the severity index.

Chapter 4

Estimation of head accelerations using neural networks and sensors embedded in the protective helmet

This manuscript was published in July 2022 to Sensors. Sensors provides an advanced forum for the science and technology of sensor and its applications.

The manuscript explores the concept of a new technology, based on sensors embedded onto a motorcycle helmet shell and Artificial Neural Networks (ANNs), to estimate the time histories of the head acceleration components during an impact. The results of this paper highlight a good accuracy of this technology in the estimation of the head kinematics in terms of time history and peak values.

This study has some limitations to be mentioned: 1) only a S/M size AGV X3000 helmet model was employed, but there are no engineering reasons to assume that different trends would be achieved with another type and size of validated helmet model (after a new training of the neural networks). At present, there are no reasons to believe that the use of a single helmet would undermine the generalization of the methodology; 2 a unique friction coefficient was used in the contacts between helmet - headform and helmet - surface. These two variables can be taken into account to investigate how the output changes. Based on the results, rather than single trends, specific corridors can be defined for the target head accelerations. Consequently, the head accelerations predicted by the ANNs can be shifted using proper coefficients to match the variability of the corridors obtained for the target curves.

In conclusion, this study represents the conceptualisation of the kinematic sub-module of the Artificial Intelligence (AI) module, which is the core of the methodology investigated in this Thesis. This represents a relevant contribution to the state of the art concerning the development of wearable devices for the assessment of the head kinematics for on-field applications.

sensors

MDPI

Article

Estimation of Head Accelerations in Crashes Using Neural Networks and Sensors Embedded in the Protective Helmet

Andrea Bracali * and Niccolò Baldanzini

Department of Industrial Engineering, University of Florence, 50139 Firenze, Italy; niccolo.baldanzini@unifi.it
* Correspondence: andrea.bracali@unifi.it; Tel.: +39-3479-284-137

Abstract: Traumatic Brain Injuries (TBIs) are one of the most frequent and severe outcomes of a Powered Two-Wheeler (PTW) crash. Early diagnosis and treatment can greatly reduce permanent consequences. Despite the fact that devices to track head kinematics have been developed for sports applications, they all have limitations, which hamper their use in everyday road applications. In this study, a new technical solution based on accelerometers integrated in a motorcycle helmet is presented, and the related methodology to estimate linear and rotational acceleration of the head with deep Artificial Neural Networks (dANNs) is developed. A finite element model of helmet coupled with a Hybrid III head model was used to generate data needed for the neural network training. Input data to the dANN model were time signals of (virtual) accelerometers placed on the inner surface of the helmet shell, while the output data were the components of linear and rotational head accelerations. The network was capable of estimating, with good accuracy, time patterns of the acceleration components in all impact conditions that require medical treatment. The correlation between the reference and estimated values was high for all parameters and for both linear and rotational acceleration, with coefficients of determination (R^2) ranging from 0.91 to 0.97.

Keywords: traumatic brain injuries (TBIs); linear acceleration; rotational acceleration; safety; helmet sensors; neural networks

Citation: Bracali, A.; Baldanzini, N. Estimation of Head Accelerations in Crashes Using Neural Networks and Sensors Embedded in the Protective Helmet. *Sensors* **2022**, *22*, 5592. https://doi.org/10.3390/s22155592

Academic Editor: Carlo Ricciardi

Received: 30 May 2022
Accepted: 22 July 2022
Published: 26 July 2022

1. Introduction

Despite attempts to minimize the incidence and severity of head injuries with improved protective equipment, closed-head impacts represent the highest percentage of Traumatic Brain Injuries (TBIs) diagnosed each year among the civil population in the United States (US) [1]. In 2017, 61,000 TBI-related deaths occurred in the United States, and motor vehicle crash was the second most relevant category after suicide [2]. In addition, TBIs, regardless of severity level, can lead to difficulties in performing daily activities, such as gait impairment [3]. Worldwide, Vulnerable Road Users (VRUs) account for more than half of all global deaths in road crashes (the events related to two- and three-wheeled vehicles represent 26% of all deaths) [4]. Therefore, models capable of properly estimating TBI are needed to perform real-time estimation of the injuries and thus to improve protective devices.

Currently, TBI risk assessment is made using criteria coupling a biomechanical metric and an injury risk function. There are two types of biomechanical metrics: based on kinematic parameters of the head or on the brain tissue deformation during the impact. Most of the existing injury criteria are based on the head kinematics since measurements, either on a dummy or a volunteer, are easier than measuring brain tissue response. An overview of these metrics was provided by Gabler et al. [5]. The latest findings on the key role played by rotational acceleration on brain injuries led the United Nations Economic Commission for Europe to revise the ECE 22.05 helmet homologation standard [6]. The new regulation, ECE 22.06, took effect on January 2021 and introduced new tests for homologation also based on the rotational acceleration [7]. Several studies [8–14] were conducted to improve the knowledge of TBI and to develop a method or an injury criterion

to estimate injuries based on kinematic parameters. The possibility of estimating the linear and rotational accelerations of the head during a crash becomes key to predicting TBIs, but the estimation process is extremely difficult in real-world conditions (e.g., impacts between football players, motorcyclists' road crashes, skiers' falls). Since a helmet is the most common solution to mitigate TBIs, several technical solutions used the helmet as part of the measuring system. Systems incorporating microelectromechanical system (MEMS) inertial sensors into helmets were developed and employed, with the Head Impact Telemetry System (HITS) [15] being one of the earliest and most widely used [11,16–21]. The HIT system is composed of six single-axis accelerometers oriented normal to the skull, and it is specifically designed to measure head accelerations by elastically coupling the accelerometers in contact with the head, isolating them from the helmet shell. The linear acceleration is estimated with an optimization method, while the rotational acceleration is computed assuming a pivot point located about 10 cm below the head Centre of Gravity (CoG). A development of HIT with a new sensor layout resulted in the 6DOF (Degrees of Freedom) HIT measurement device [22], providing both the linear and the rotational accelerations and iteratively solving the optimization problem [12,20,23].

The most recent helmeted device was the gForce Tracker (GFT) [24], characterized by a triaxial accelerometer and a triaxial gyroscope embedded inside a casing attached to the helmet. This technology provides the maximum values of the resultant linear acceleration and rotational velocity obtained from a power fit regression. Other devices require a rigid connection to the head such as mount-guards, earplugs and bands. These devices provide more accurate data at the expense of comfort and user-friendliness, and they may cause an acceptability problem to end users such as motorcyclists or bikers.

Although the indirect identification of the head kinematics by using helmet dynamics was extensively deepened in previous research, all measurement devices fitted to the helmet and capable of estimating kinematic parameters as a function of time require sensors to be in contact with the head to overcome the difficulties due to the relative movement between head and helmet. The helmet rotation in relation to the head is primarily affected by the coupling of different head and helmet sizes as well as by a combination of padding compression, chin strap tension, and friction between the helmet and the head. This dependency produces different rotational velocities and rotational acceleration sustained by the helmet and head during an impact. Additionally, the presence of the foam component between the helmet outer shell and the head significantly reduces its linear acceleration compared to the helmet one. Manoogian et al. [25] demonstrated that the helmet peak linear acceleration is approximately 10 times the head peak acceleration. More recently, Joodaki et al. [26] found that the peak linear acceleration of the helmet was 2/5 times greater than the head one, while the helmet peak angular velocity was greater or smaller than the head one according to the impact conditions; in some tests, the helmet rotated more than 30 deg relative to the head.

The technical solution investigated in this paper is based on a novel sensing system characterized by a new layout of the accelerometers, which are placed on the inner side of the helmet shell. In this configuration, the signal processing for the determination of the head kinematics cannot rely on simplifying assumptions, as typical of previous studies. The high number of parameters influencing head kinematics increases the complexity level and suggests the use of deep learning techniques for the estimation task.

At present, there are a limited number of applications of deep Artificial Neural Networks (dANNs) for identifying the impact load history of structures [27–29]. dANNs are computing models used for information processing that only need data for supervised learning. They are often used to identify and model a complex functional relationship or pattern between input and output data with a black-box approach. ANNs can detect complex non-linear relationships between variables through their training phase. Nowadays, several software offer packages to develop ANNs in an easy and friendly way with multiple training algorithms [30]. However, ANNs also have some disadvantages: performances achieved are highly reliant on the quantity and quality of data given as input and output to train the networks; collecting the necessary amount of data to train the network can be

costly and time-consuming [31]. Staszewski [28] and Ghajari [27] used an dANN model to identify the impact load acting on a composite plate; specifically, in Ghajari [27], the effects of signal features, network architectures and sensor placements on the performance of the dANN model were analyzed. Most recently, Zhou [29] proposed a novel impact load identification method of non-linear structures by using deep Recurrent Neural Networks (RNNs), verifying this method in three non-linear cases: damped Duffing oscillator, non-linear three-degree-of-freedom system and non-linear composite plate. Finally, deep learning neural networks techniques were recently implemented to recognize human activities from wearable sensors [32,33]. To date, there is no application for the identification of a body (e.g., head) acceleration with sensors embedded in a second body (e.g., helmet), which exhibits a relative movement to the first one.

This paper contributes to the methodological development of a device for the real-time estimation of TBIs. Specifically, it proposes a novel method to estimate, as time functions, the components of head linear and rotational accelerations from signals provided by twelve single-axis accelerometers embedded in the outer shell of a motorcycle helmet. The sensors are organized in orthogonally oriented pairs at six different locations, with their sensing axis tangential to the helmet, as described in [34]. The system's non-linearity at the helmet–head interface is modeled within the estimation process using deep learning ANNs. They were trained using data collected from finite element simulations, which is a time-saving and cost-effective technique compared to carrying out the same number of experimental tests.

2. Materials and Methods

Head impact scenarios were defined considering previous research on head impacts. A wide and representative set of impact conditions was defined and reproduced with a finite element model to generate the necessary datasets. The Artificial Neural Network architecture was defined to optimize the estimation of head kinematics. The procedure implemented to develop and validate the technology is described at the end of this section.

2.1. Head Impact Scenarios

A head impact scenario can be defined by two different variables: relative position between the helmeted head and the ground and the impact speed vector. Considering a reference scenario (Figure 1a) where the helmeted head was oriented such that the transverse plane of the head was parallel to the ground, the relative position in a generic scenario was defined by sequentially rotating the ground around the X-axis and Y-axis, while the helmeted head position was unchanged. Different ranges were considered for these two parameters: the angle β around the X-axis was varied between -100° and 100°, but the angle γ around the Y-axis was varied between -125° and 115°.

The impact speed vector was defined through its tangential and normal components to the ground and the orientation of the tangential component in the ground plane. Vehicle impact speed varies between 20 and 88 km/h in urban accidents [35]. Different studies reproducing typical oblique impacts in motorcycle crashes through experimental impact tests [36] or FE analyses [27,37] observed that the angular kinematics of the head remained quite constant at high tangential speeds. Cernicchi et al. [38] simulated motorcycle head impacts using two different V_n magnitudes: 2.20 and 5.66 m/s and a tangential velocity ranging from 0 to 60 m/s. They observed that at constant V_n, the angular acceleration peak did not vary above a specific V_t threshold (V_t^*). However, as V_n increased, the value of V_t^* seemed also to increase (for V_n = 2.20 m/s, V_t^* = 4.21 m/s, while for V_n = 5.66 m/s, V_t^* = 8.57 m/s). Based on previous research, the magnitude of the impact speed ranged between 8 and 78 km/h to reproduce real-world head impacts in urban crashes. This magnitude was obtained by combining the normal speed component V_n, which ranged between 2 and 12 m/s, and the tangential speed component V_t, which varied between 3 and 18 m/s. A range of 360° was considered for the orientation of the tangential component in the ground plane (angle θ).

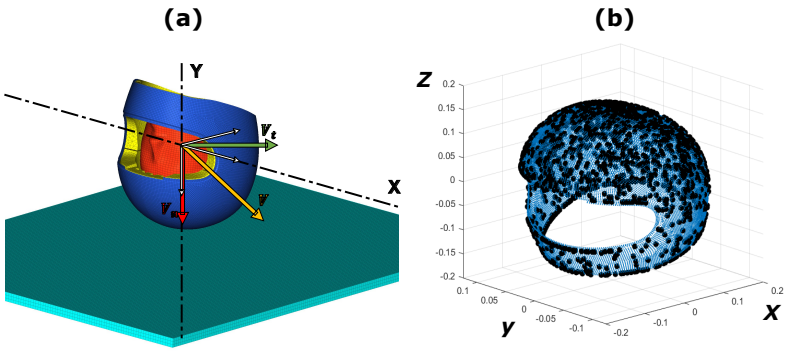

Figure 1. (**a**) Start of the first head-impact scenario; (**b**) scatter plot of the shell mesh nodes (blue points) and the impact points (black points) for the entire training dataset.

The latter five parameters (rotational angles around X-axis and Y-axis, normal and tangential impact speed components and tangential speed orientation) were combined using the Latin Hypercube Sampling (LHS) method [39] to define three different datasets of, respectively, 2000, 200 and 300 simulations. The purpose of the three datasets will be clarified later in Section 3. The impact points on the helmet outer shell for the training dataset of 2000 simulations are shown in Figure 1b.

2.2. Finite Element Head and Helmet Model

Head impact scenarios were simulated using a Hybrid III (HIII) Head finite element model (https://biocorellc.com/finite-element-models/) (accessed on 21 July 2022) distributed by the Biomechanics and Research, LLC (Biocore) [40], which was coupled with an AGV X3000 full-face helmet provided by the Dainese company.

The original HIII model included both the head and neck, but only the head model was used in this study, in accordance with the ECE 22.06 standard [7]. The HIII head was previously validated by the University of Virginia Center for Applied Biomechanics [40], simulating the NHTSA Head Drop Certification Test. The present head includes three main parts: skin rubber layer, rigid skull and head mount. Both the head skin and mount used hexahedral solid elements, but the quadrilateral shell elements were used to mesh the rigid skull.

The helmet model consists of an outer shell, an energy-absorbing liner, a chin pad and a chin strap. Further information about the helmet finite element model used in this paper can be found in [34]. This model was updated, including the accelerometers of the measurement device. Further information about the procedure adopted to select the accelerometer locations can be found in [34].

2.3. Neural Networks

Recurrent neural networks [41] are one of the most known types of Artificial Neural Networks, capable of processing sequential data or time series data. The ability to use feedback loops, commonly described as "memory", ensures the output is influenced by both previous and current inputs. The process of carrying memory forward is described mathematically:

$$h_t = f_h(U * x_t + V * h_{t-1}) \quad (1)$$

$$o_t = f_o(W * h_t) \quad (2)$$

where x_t is the input at time step t, h_t stores the values of the hidden units at time step t and

o_t is the output at time step t. f_h and f_o are the hidden and output unit activation functions. They define how the weighted sum of the input is transformed into an output; commonly used activation functions are logistic sigmoid, rectified linear (ReLU) and Hyperbolic Tangent (Tanh). The weight matrices U, W and V are determined with supervised training of the RNN, but it requires a huge amount of data (Figure 2a). A relevant problem in RNNs concerns long-term memory: input information $(x_{t'})$ persists for a short time, but it cannot be kept for a long period of time due to the vanishing gradient problem.

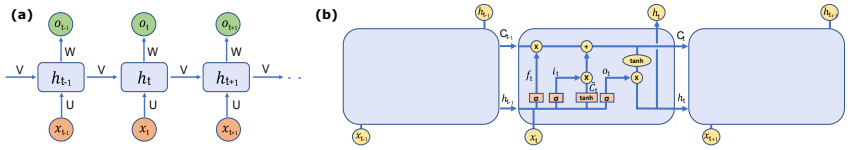

Figure 2. (**a**) Recurrent Neural Network; (**b**) Long Short Term Memory (LSTM) cell.

The long-term dependency was improved with the Long Short-Term Memory (LSTM) structure, introduced by Hochreitener and Schmidhurber [42] for the first time in 1997. They replaced the typical recurrent unit of RNNs with a more complex gated recurrent unit. The LSTM used in this study is a standard LSTM, and it is shown in Figure 2b. The LSTM forward propagation process is described mathematically:

$$f_t = \sigma(W_f * [h_{t-1}, x_t] + b_f) \tag{3}$$

$$i_t = \sigma(W_i * [h_{t-1}, x_t] + b_i) \tag{4}$$

$$\widetilde{C}_t = tanh(W_c * [h_{t-1}, x_t] + b_c) \tag{5}$$

$$C_t = f_t * C_{t-1} + i_t * \widetilde{C}_t \tag{6}$$

$$o_t = \sigma(W_o * [h_{t-1}, x_t] + b_o) \tag{7}$$

$$h_t = o_t * tanh(C_t) \tag{8}$$

where x and h are the input and the output, W the weight matrices and b the biases; σ and $tanh$ are the logistic sigmoid and Tanh activation functions. The LSTM cell can decide whether to discard or keep the past information using the variable "Cell State" (C). With a value of C equal to 1, the information is completely kept, while a 0 means that the information is discarded. The signals of the accelerometers embedded in the helmet are the inputs to the LSTM network, while the outputs are the components of the linear or rotational acceleration of the head. Two separate but identical networks were used for the linear and rotational components to improve the estimation results.

A simple Neural Network with a single LSTM layer did not provide good performances in the impact force history identification, as stated by Zhou [29]. Assuming that the same conclusion can be considered for the estimation of impact acceleration, the deep neural network architecture used by Zhou [29] was the starting point for this study. Some improvements were identified to maximize the performance for the specific problem, and the final architecture is shown in Figure 3. It consists of a Bidirectional Long Short-Term Memory (BLSTM) layer, two LSTM layers and two Fully Connected (FC) layers. Basically, a BLSTM layer consists of a forward LSTM layer and a backward LSTM layer. This provides the opportunity to consider both past and future responses of sequential inputs. BLSTM and the two LSTM layers have 200 cells per layer, the first FC layer has 200 hidden units, but the last FC layer has a number of hidden units equal to the number of outputs. The over-fitting was prevented using the dropout operation to each non-recurrent connection, as shown in the dashed lines in Figure 3. From here onwards, this neural network architecture will be referred to as deep Artificial Neural Network (dANN).

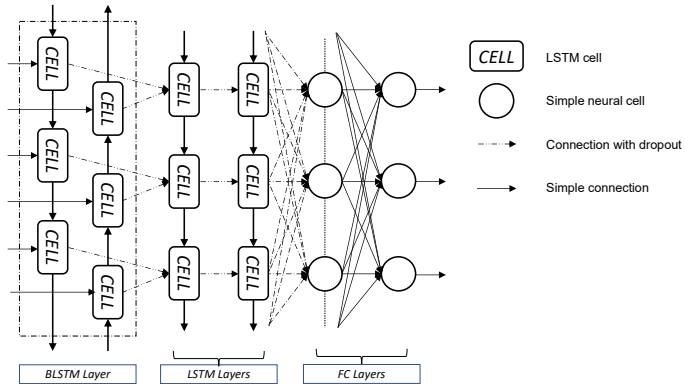

Figure 3. Deep Artificial Neural Network (dANN) architecture.

3. Identification Steps

STEP 1—Development of simulation datasets. Three datasets of simulations reproducing real-world head impacts in urban crashes were implemented with the procedure explained in Section 2.1. The first dataset consisted of 2000 simulations, and the second and the third ones consisted of, respectively, 200 and 300 simulations. The first dataset was used for training the network, while the second and the third datasets were used, respectively, for validation and testing purposes.

STEP 2—Neural Networks design. Two deep neural networks with the same structure described in Section 2.3 were implemented. The networks had the same inputs, i.e., accelerations from the accelerometers embedded in the helmet't outer shell, but the outputs differed: the three head linear acceleration components were used as outputs of the network *A* and the three head rotational acceleration components were the outputs of the network *B*. From here onwards, the neural networks estimating linear and rotational accelerations will be referred to as *A* and *B*, respectively.

STEP 3—Data preparation. Accelerations of the helmet outer shell were filtered using a SAE108 filter, but both the linear and rotational head accelerations were filtered with a CFC1000 filter as suggested by ISO 6487:2002 standard [43].

STEP 4—Model training. Networks *A* and *B* were fed with the inputs and outputs described in STEP 2. Weights and biases were optimized using a back-propagation through time (BPTT) [44] algorithm. The Root Mean Square propagation (RMSprop) [45] was selected as the optimizer. RMSprop is a Gradient Descent-based Learning Algorithm, which adapts, at each iteration, the learning rate of each parameter individually using a subset of the training data. A different subset, called a mini-batch, is used at each iteration. A mini-batch size equal to 16 was chosen to implement this process. The initial learning rate was 0.001, and the maximum epochs used for the training were 1000. After each training epoch, the Root-Mean-Squared-Error (RMSE) on the validation data was monitored. If the RMSE did not decrease after 30 consecutive epochs, the training process was stopped. Every 45 epochs, the learning rate was reduced by a factor of two.

STEP 5—Model performance assessment. Helmet accelerations from the test dataset were used as input for both the NNs *A* and *B*, and the estimated linear and rotational head acceleration components were compared to the target ones. Three parameters were introduced to assess the model performance: peak error, Head Injury Criterion (HIC) [46] and Rotational Injury Criterion (RIC) [12]. The assessment parameters were applied to both the reference head accelerations (extracted from the simulations) and the head accelerations estimated with the dANN. For each of them, the Pearson coefficient R^2 was calculated.

HIC [46] is the most commonly used metric for evaluating head and brain injury risk; it is currently required by the UN/ECE 22.06 standard [7] used in helmet regulation.

$$HIC = max\left\{(t_2 - t_1)\left[\frac{1}{t_2 - t_1}\int_{t_1}^{t_2}|a(t)dt|\right]^{2,5}\right\} \quad (9)$$

where a is the magnitude of the resultant head linear acceleration, and t_1 and t_2 are, respectively, the initial and final integral times over which HIC is calculated (t_1 and t_2 are selected to maximize HIC).

RIC was proposed by Kimpara et al. [12]; it was formulated similarly to HIC by replacing the linear acceleration term with angular acceleration.

$$RIC = max\left\{(t_2 - t_1)\left[\frac{1}{t_2 - t_1}\int_{t_1}^{t_2}|\alpha(t)dt|\right]^{2,5}\right\} \quad (10)$$

where α is the magnitude of the resultant head linear acceleration. For t_1 and t_2, the same considerations made for the HIC are applicable.

In this paper, no consideration about the correlation between the HIC / RIC and head injuries will be analyzed. These criteria were selected exclusively as parameters to compare the estimated and target curves.

4. Results

4.1. Training Dataset

Training, validation and testing datasets were generated as described in Section 2.1 and the five parameters used to define the impact simulations were combined using the LHS. Initially the 2000 values of each parameter were sampled uniformly within their ranges. With this solution, most of the impact points were in the top outer shell area, but the left, right, back and chin areas had a poor spatial sampling. Therefore, the parameters that contributed to spreading the impact points over the outer shell surface (i.e., α and β) were modified, as shown in Figure 4a for β. Angle distributions were modified to have lower frequencies between $-20°$ and $20°$ than between $-100°$ and $-60°$ or $60°$ and $100°$. The new distribution of the parameters created a uniform spatial sampling over the entire outer shell surface of the helmet, as shown in Figure 1.

Figure 4b,c show, respectively, the distribution of the impact speed and the angle between the impact speed direction and the ground. Most of the impact simulations are characterized by an impact speed magnitude within the range of 8–16 m/s and an inclination angle within the range of 16–45°.

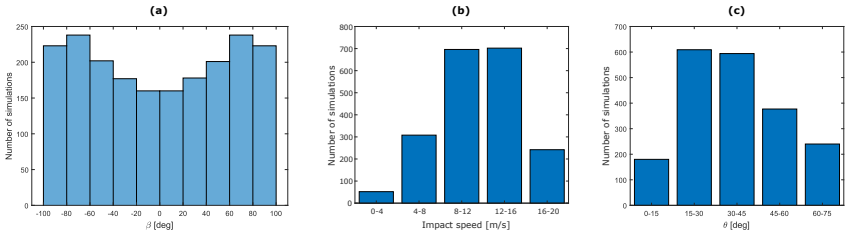

Figure 4. Distribution of (**a**) β angle values, (**b**) the impact speed magnitude, (**c**) the angle between the impact speed direction and the ground for the training dataset simulations.

4.2. Head Linear Acceleration

The deep Artificial Neural Networks used to estimate the head linear acceleration components were trained, as described in STEP 4 of Section 3. LSTM and BLSTM layers and the first fully-connected layer had 200 hidden units. Dropout probability was set equal to 0.5 and learning rate equal to 0.001. Two examples of the estimated linear acceleration are shown in Figure 5: the plot in the rightmost column shows the resultant accelerations obtained by combining the three components plotted in previous columns.

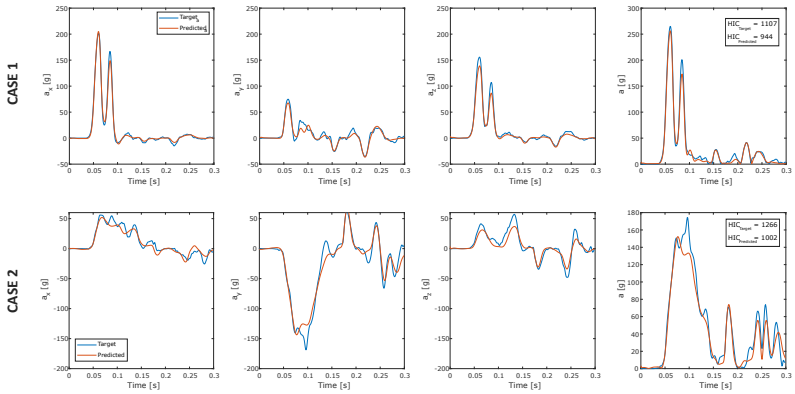

Figure 5. Linear acceleration prediction using the deep neural network model.

The dANN reproduces the acceleration component's shape and the peak values in both cases well (Figure 5). Peak values and HIC were calculated on the entire testing dataset (300 simulations). Scatter plots in Figure 6 show the comparison between peak values of the target and estimated acceleration components. Peaks of the Z-component had the best overall performance with $R^2 = 0.972$. Parameters calculated on the resultant acceleration, i.e., peak value and HIC, had similar R^2 high values, confirming the strong learning ability of dANNs (Figure 7).

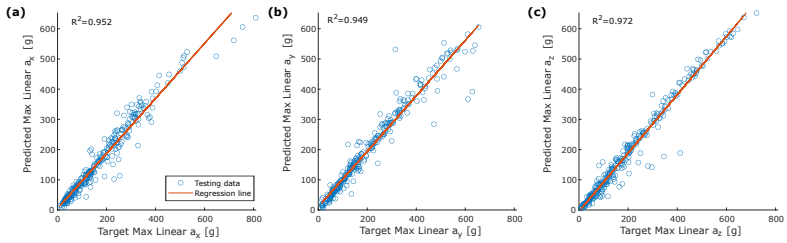

Figure 6. Correlation between target and predicted peak linear acceleration: (**a**) a_x; (**b**) a_y; (**c**) a_z.

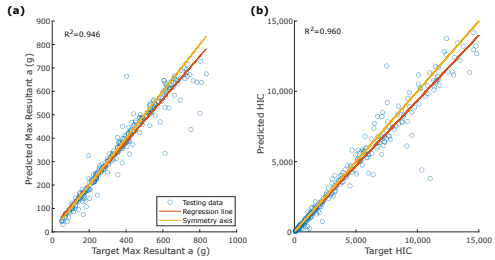

Figure 7. Correlation between (**a**) target and predicted peak for the resultant linear acceleration and (**b**) target and predicted HIC.

4.3. Head Rotational Acceleration

The dANN used to estimate the head rotational accelerations had the same architecture as the dANN described in Section 4.2. Figure 8 shows the rotational accelerations for the same cases reported in Figure 5. Rotational acceleration components of shape and peak values were estimated with a good approximation (Figure 9). Rotational peak values around the Y-axis had the best performances, with $R^2 = 0.908$. R^2 coefficients for the peak values around the X and Z axes were, respectively, 0.800 and 0.783.

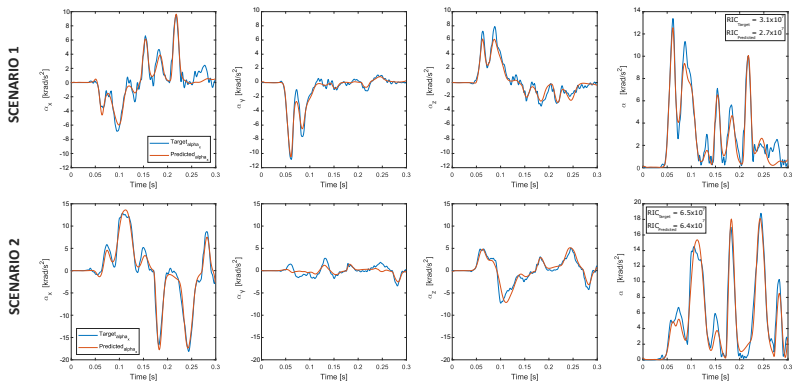

Figure 8. Rotational acceleration prediction using the deep neural network model.

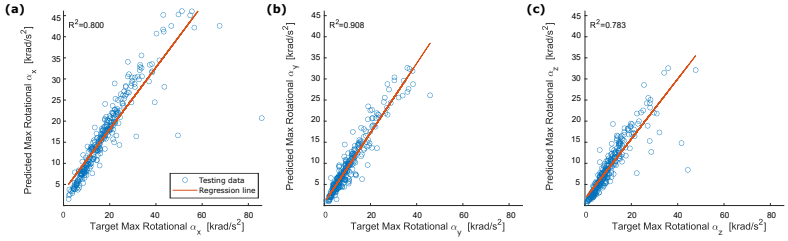

Figure 9. Correlation between target and predicted peak rotational acceleration: (a) α_x; (b) α_y; (c) α_z.

Peak values of the resultant acceleration and RIC have an R^2 correlation coefficient, respectively, of 0.771 and 0.687. (Figure 10). For both parameters, the regression line and the symmetry axis largely diverge for high values of acceleration.

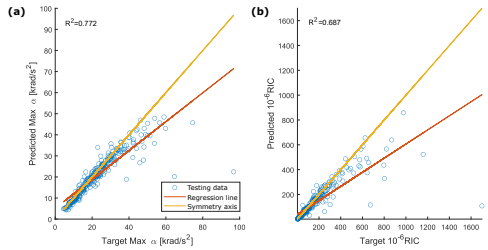

Figure 10. Correlation between (**a**) target and predicted peak for the resultant rotational acceleration and (**b**) target and predicted RIC.

5. Discussions

The indirect head kinematics estimation, through sensors embedded in protective devices and far from the head, is the only way to enable the real-time evaluation of TBIs without reducing the acceptability of the protective devices by the end users. This study presents the development and assessment of a new methodology, based on deep neural networks applied to a sensor system, to estimate the head kinematics with sensors attached to the inner surface of a helmet's outer shell.

Different designs for the neural network used to estimate linear and rotational accelerations were tested. The analyzed architectures differed in the number of BLSTM and LSTM layers. Table 1 reports the designs of the networks and their performances for the rotational acceleration. R^2 for peak values and RIC were used to compare the performances of the different deep neural networks investigated. DANN0 has the architecture and hyperparameters suggested by Zhou [29]; it was trained using the Adam optimizer, i.e., the same used by Zhou in his study. Network performances were not acceptable since values of R^2 ranged between 0.168 and 0.278 for the estimation of peak values. A set of changes (network architecture integrated with an FC layer, learning rate decreased to 0.001, hidden units decreased to 100, and the Adam optimizer replaced with the RMSprop one) led to great improvements. Progressive increase in Hidden Unit values (100, 200 and 300; DANN1-DANN3) generated a slight improvement in the performances against an increase in training time. For instance, using 300 hidden units instead of 200 did not produce considerable improvement (as described in the next paragraphs, results are mainly affected by the lack of data for high acceleration values); therefore, 200 hidden units were used to analyze the learning rate influence. The worst results were obtained by decreasing or increasing the learning rate, as shown, respectively, by model DANN4 and DANN5. Other more complex architectures were investigated (models DANN6-DANN9), but none of them considerably improved the performances to justify the adoption of a more complex architecture against an increase in training time. BLSTM, 2LSTM and 2FC architecture were the most suitable for head kinematics estimation, and it was selected as the preferred one. DANN2 (Table 1) was used both to present the results shown in Section 4 and for the considerations listed below.

Table 1. Effect of learning rate, hidden units and architecture in the peak values and RIC estimation.

	Architecture	Learning Rate	Hidden Units	R^2 Peak Value				R^2 RIC
				α_x	α_y	α_z	Resultant	
DANN0	BLSTM and 2LSTM [29]	0.005	128	0.248	0.278	0.168	0.192	0.404
DANN1	BLSTM and 2LSTM and 2FC	0.001	100	0.776	0.882	0.795	0.755	0.672
DANN2	BLSTM and 2LSTM and 2FC	0.001	200	0.800	0.908	0.783	0.772	0.687
DANN3	BLSTM and 2LSTM and 2FC	0.001	300	0.802	0.927	0.827	0.783	0.681
DANN4	BLSTM and 2LSTM and 2FC	0.01	200	0.775	0.849	0.759	0.746	0.679
DANN5	BLSTM and 2LSTM and 2FC	0.0001	200	0.689	0.016	0.231	0.529	0.514
DANN6	BLSTM and 3LSTM and 2FC	0.001	200	0.817	0.901	0.834	0.782	0.710
DANN7	2BLSTM and 3LSTM and 2FC	0.001	200	0.791	0.917	0.834	0.791	0.705
DANN8	3BLSTM and 2LSTM and 2FC	0.001	200	0.804	0.890	0.765	0.772	0.650
DANN9	4LSTM and 2FC	0.001	200	0.782	0.900	0.780	0.772	0.643

The overall correlation between the reference and estimated head accelerations was higher for the linear accelerations than the rotational ones (i.e., $R^2 = 0.946$ vs. $R^2 = 0.772$ for the resultant). Specifically, rotational acceleration estimation worsens as the absolute value of the acceleration peak increases. As shown in Figure 10, the regression line and the symmetry axis diverge for high values of acceleration. This did not happen for the parameters of the resultant linear acceleration (Figure 7), as the regression line and the symmetry axis remained almost parallel, even for high values of acceleration. The increase in the identification error was expected since rotational acceleration is strongly influenced by friction between head and helmet and the system behavior is more complex to model.

Looking at the comparison between the target and estimated peak values of the resultant rotational acceleration (Figure 10a), the network underestimates the target values starting from a target peak of 40 krad/s^2. This is confirmed by a smaller slope of the regression line compared to the symmetry axis. The network performance is affected by the small number of impacts with high rotational acceleration in the datasets (143 out of 2000 in the training dataset, 28 out of 300 in the testing dataset with a peak of rotational acceleration exceeding 40 krad/s^2). This result is a consequence of the procedure used to generate the databases: the position of the helmet with respect to the ground and the impact speed is defined, and the accelerations of the head–helmet system are a consequence of these parameters. Nonetheless, the network performances need to be properly framed within the physiological limits of the human body and take into account the overall objective of the research (i.e., early detection and treatment of TBIs). From this context, acceleration values, which cause immediate and permanent brain damage, should be clearly excluded.

Brain injury tolerance based on head rotational acceleration was investigated in numerous studies. Pike [47] proposed a peak angular head acceleration of 9 krad/s^2 associated

with a 10% risk of Mild Traumatic Brain Injury (MTBI) based on 27000 head impacts recorded from American football players at the collegiate level. Zhang et al. [48] proposed a maximum resultant rotational acceleration peak of 7.9 krad/s^2 for an 80% probability of sustaining an MTBI. Rotational acceleration peak was also connected to specific TBI such as concussion and DAI. The first type of injury was analyzed by Ommaya et al. [8], which suggested an angular acceleration tolerance of 1.8 krad/s^2 for a 50% probability of concussion. Rowson et al. [20] proposed a tolerance value of 6383 krad/s^2 for the same probability of concussion. Finally, Margulies and Thibault [10] proposed an angular acceleration of 16 krad/s^2 as tolerance to moderate to severe DAI for the human head subjected to a lateral motion. These results support the exclusion of impacts with peak rotational acceleration above 40 krad/s^2 from the assessment of the proposed method, as this threshold is more than double the highest value cited in [10]. With the redefined dataset, the estimation of peak values is improved, and R^2 exceeded 0.9 for each component. The new scatter plots for peak values of the acceleration components, the resultant acceleration and RIC are shown in Figures 11 and 12. Considering Figures 7 and 12, a slight systematic underestimation of the accelerations is still evident when the absolute peak value increases. Future exploitation of this method in a real-time system implemented into a helmet should include a proper correction to adjust for these errors.

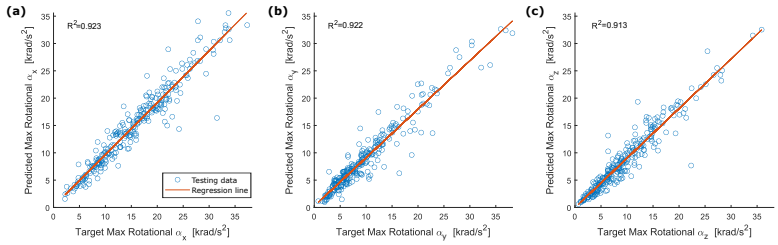

Figure 11. Correlation between target and predicted peak rotational acceleration for the reduced testing dataset (exclusion of impacts with peak rotational acceleration above 40 krad/s^2): (**a**) α_x; (**b**) α_y; (**c**) α_z.

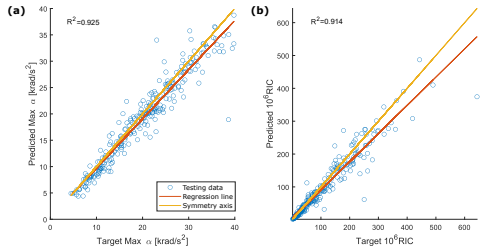

Figure 12. Correlation between (**a**) target and predicted peak for the resultant rotational acceleration and (**b**) target and predicted RIC for the reduced testing dataset (exclusion of impacts with peak rotational acceleration above 40 krad/s^2).

A considerable amount of data is usually needed to obtain acceptable results from a trained deep neural network. Zhou et al. [29], in the identification of the impact load history acting on a composite plate, have used 10,000 signals to train their dANN, compared to 2000 acceleration signals used in this study. All simulations were run on a 72-cpu cluster and each simulation took approximately 20 min, for 28 days of total computational time.

As well as the performances of the dANNs, calculation time is really important for a future industrial application of this method. Results proved that the indirect identification of head kinematics history through dANNs, fed with data from accelerometers embedded in the helmet, can be successfully accomplished using a training dataset of limited size. The use of the LHS method to combine the factors described in Section 2.1 and create a well-distributed dataset of simulations for the training process was a relevant contribution to the methodology, as it avoided data overfitting and selection bias.

6. Conclusions

In this paper, a novel method to identify the head linear and rotational acceleration time signals from acceleration data, acquired by single-axis sensors embedded in the outer shell of a helmet and processed with deep learning techniques, is presented. The results support the following major findings:

- Neural Networks: LSTM Neural Networks are capable of reproducing the underlying non-linear behavior of the model. A specific network was defined to solve the problem, and the related hyperparameters were determined. This result enables real-time prediction of head kinematics and paves the road to the application of specific metrics for TBI estimation.
- Dataset:
  - The training, validation and testing datasets can be obtained from a virtual environment using state-of-the-art tools (e.g., Finite Elements). The approach used for the generation of datasets greatly reduces time requirements and costs compared to experimental tests;
  - An adequate size for the datasets was determined, which may be used for guidance in further applications. The networks can be trained with a limited amount of data because of the well-distributed dataset generated using the LHS method to combine the parameters defining our case study;
  - Both the use of virtual testing tools and the application of the LHS method to generate the simulation inputs facilitate the industrial application of the methodology.
- Prediction: The results proved the high accuracy of the trained networks, as a high correlation coefficient was obtained for all the parameters used in the assessment stage.

To the best knowledge of the authors, this is the first application of neural networks for the estimation of a body (head) acceleration with sensors embedded in a second body (helmet), considering that the two bodies are not fully connected. The results proved the feasibility of the proposed methodology. The next steps will focus on the experimental validation of the findings highlighted in this study.

Author Contributions: Conceptualization, A.B. and N.B.; methodology, A.B. and N.B.; software, A.B.; validation, A.B.; formal analysis, A.B.; investigation, A.B.; data curation, A.B.; writing—original draft preparation, A.B.; writing—review and editing, A.B. and N.B; visualization, A.B.; supervision, N.B. All authors have read and agreed to the published version of the manuscript.

Funding: This research received no external funding.

Institutional Review Board Statement: Not applicable

Informed Consent Statement: Not applicable

Data Availability Statement: The data that support the findings of this study are available from the authors upon reasonable request.

Acknowledgments: This study utilized a model derived from a model licensed from Biomechanics Consulting and Research, LC (Biocore). The development of this model was made possible by a grant from Football Research, Inc. (FRI) and the National Football League, with input from the NFLPA. The views expressed are solely those of the authors and do not represent those of Biocore, FRI, or

any of its affiliates or funding sources. The authors acknowledge Dainese SpA for supporting this research through the availability of the FE helmet model.

Conflicts of Interest: The authors declare no conflict of interest.

Abbreviations

The following abbreviations are used in this manuscript:

TBIs	Traumatic Brain Injuries
PTW	Powered Two Wheeler
ANNs	Artificial Neural Networks
VRUs	Vulnerable Road Users
MEMS	MicroElectroMechanical Systems
HITS	Head Impact Telemetry System
CoG	Centre of Gravity
6DOF	6 Degrees of Freedom
GTF	gForce Tracker
RNNs	Recurrent Neural Networks
LHS	Latin Hypercube Sampling
HIII	Hybrid III
ReLU	Rectified linear function
Tanh	Hyperbolic Tangent function
LSTM	Long Short Term Memory
BLSTM	Bidirectional Long Short Term Memory
FC	Fully Connected
dANN	deep Artificial Neural Network
BPTT	Back Propagation Through Time
RMSprop	Root Mean Square propagation
RMSE	Root Mean Square Error
HIC	Head Injury Criterion
RIC	Rotational Injury Criterion
MTBI	Mild Traumatic Brain Injury

References

1. Santiago, L.A.; Oh, B.C.; Dash, P.K.; Holcomb, J.B.; Wade, C.E. A clinical comparison of penetrating and blunt traumatic brain injuries. *Brain Inj.* **2012**, *26*, 107–125.
2. Daugherty, J.; Waltzman, D.; Sarmiento, K.; Xu, L. Traumatic Brain Injury–Related Deaths by Race/Ethnicity, Sex, Intent, and Mechanism of Injury—United States, 2000–2017. *MMWR* **2019**, *46*, 1050–1056.
3. Dever, A.; Powell, D.; Graham, L.; Mason, R.; Das, J.; Marshall, S.J.; Vitorio, R.; Godfrey, A.; Stuart, S. Gait impairment in traumatic brain injury: A systematic review. *Sensors* **2022**, *22*, 1480.
4. World Health Organization and others. *Global Status Report on Road Safety 2018: Summary*; World Health Organization: Geneva, Switzerland 2018.
5. Gabler, L.F.; Crandall, J.R.; Panzer, M.B. Assessment of Kinematic Brain Injury Metrics for Predicting Strain Responses in Diverse Automotive Impact Conditions. *Ann. Biomed. Eng.* **2016**, *44*, 3705–3718.
6. United Nations. *Uniform Provisions Concerning the Approval of Protective Helmets and Their Visors for Drivers and Passengers of Motor Cycles and Mopeds*; UN ECE 22.05; United Nations: San Francisco, CA, USA, 2002.
7. United Nations. *Uniform Provisions Concerning the Approval of Protective Helmets and Their Visors for Drivers and Passengers of Motor Cycles and Mopeds*; UN ECE 22.06; United Nations: San Francisco, CA, USA, 2021.
8. Ommaya, A.K.; Hirsch, A.E.; Yarnell, P.; Harris, E.H. *Scaling of Experimental Data on Cerebral Concussion in Sub-Human Primates to Concussion Threshold for Man*; DTIC Document; DTIC: Fort Belvoir, VR, USA, 1967.
9. Ono, K.; Kikuchi, A.; Nakamura, M.; Kobayashi, H.; Nakamura, N. Human Head Tolerance to Sagittal Impact—Reliable Estimation Deduced from Experimental Head Injury Using Subhuman Primates and Human Cadaver Skulls. *JSAE Trans.* **1980**, *1089* 3837–3866.
10. Margulies, S.S.; Thibault, L.E. A proposed tolerance criterion for diffuse axonal injury in man. *J. Biomech.* **1992**, *25*, 917–923.
11. Greenwald, R.M.; Gwin, J.T.; Chu, J.J.; Crisco, J.J. Head impact severity measures for evaluating mild traumatic brain injury risk exposure. *Neurosurgery* **2008**, *10*, 789–798.
12. Kimpara, H.; Iwamoto, M. Mild Traumatic Brain Injury Predictors Based on Angular Accelerations During Impacts. *Ann. Biomed. Eng.* **2012**, *40*, 114–126.

13. Rowson, S.; Duma, S.M. Brain Injury Prediction: Assessing the Combined Probability of Concussion Using Linear and Rotational Head Acceleration. *Ann. Biomed. Eng.* **2013**, *41*, 873–882.
14. Gabler, L.F.; Crandall, J.R.; Panzer, M.B. Investigating Brain Injury Tolerance in the Sagittal Plane Using a Finite Element Model of the Human Head. *Int. J. Automot. Eng.* **2016**, *10*, 37–43.
15. Crisco, J.J.; Chu, J.J.; Greenwald, R.M. An algorithm for estimating acceleration magnitude and impact location using multiple nonorthogonal single-axis accelerometers. *J. Biomech. Eng.* **2005**, *126*, 849.
16. Duma, S.M.; Manoogian, S.J.; Bussone, W.R.; Brolinson, P.G.; Goforth, M.W.; Donnenwerth, J.J.; Crisco, J.J. Analysis of real-time head accelerations in collegiate football players. *Clin. J. Sport Med.* **2005**, *15*, 3–8.
17. Funk, J.R.; Duma, S.M.; Manoogian, S.J.; Rowson, S. Biomechanical Risk Estimates for Mild Traumatic Brain Injury. *J. Chem. Inf. Model.* **2007**, *4510*, 343–361.
18. Crisco, J.J.; Wilcox, B.J.; Beckwith, J.G.; Chu, J.J.; Duhaime, A.C.; Rowson, S.; Greenwald, R.M. Head impact exposure in collegiate football players. *J. Biomech.* **2011**, *44*, 2673–2678.
19. Beckwith, J.G.; Greenwald, R.M.; Chu, J.J. Measuring head kinematics in football: Correlation between the head impact telemetry system and Hybrid III headform. *Ann. Biomed. Eng.* **2012**, *40*, 237–248.
20. Rowson, S.; Duma, S.M.; Beckwith, J.G.; Chu, J.J.; Greenwald, R.M.; Crisco, J.J.; Maerlender, A.C. Rotational head kinematics in football impacts: An injury risk function for concussion. *Ann. Biomed. Eng.* **2012**, *40*, 1–13.
21. Jadischke, R.; Viano, D.C.; Dau, N.; King, A.I.; McCarthy, J. On the accuracy of the Head Impact Telemetry (HIT) System used in football helmets. *J. Biomech.* **2013**, *46*, 2310–2315.
22. Rowson, S.; Beckwith, J.G.; Chu, J.J.; Leonard, D.S.; Greenwald, R.M.; Duma, S.M. A six degree of freedom head acceleration measurement device for use in football. *J. Appl. Biomech.* **2011**, *10*, 8–14.
23. Beckwith, J.G.; Chu, J.J.; Greenwald, R.M. Validation of a noninvasive system for measuring head acceleration for use during boxing competition. *J. Appl. Biomech.* **2007**, *23*, 238–244.
24. Allison, M.A.; Kang, Y.S.; Maltese, M.R.; Bolte, J.H.; Arbogast, K.B. Measurement of Hybrid III head impact kinematics using an accelerometer and gyroscope system in ice hockey helmets. *Ann. Biomed. Eng.* **2015**, *43*, 1896–1906.
25. Manoogian, S.; McNeely, D.; Duma, S.; Brolinson, G.; Greenwald, R. Head acceleration is less than 10 percent of helmet acceleration in football impacts. *Tech. Pap. ISA* **2006**, *42*, 383–388.
26. Joodaki, H.; Bailey, A.; Lessley, D.; Funk, J.; Sherwood, C.; Crandall, J. Relative motion between the helmet and the head in football impact test. *J. Biomech. Eng.* **2019**, *141*, 1–16.
27. Ghajari, M.; Peldschus, S.; Galvanetto, U.; Iannucci, L. Effects of the presence of the body in helmet oblique impacts. *Accid. Anal. Prev.* **2013**, *10*, 142–149.
28. Staszewski, W.J.; Worden, K.; Wardle, R.; Tomlinson, G.R. Fail-safe sensor distributions for impact detection in composite materials. *Smart Mater. Struct.* **2000**, *9*, 298–303.
29. Zhou, J.M.; Dong, L.; Guan, W.; Yan, J. Impact load identification of nonlinear structures using deep Recurrent Neural Network. *Mech. Syst. Signal Process.* **2019**, *133*, 106292.
30. Tu, J.V. Advantages and disadvantages of using artificial neural networks versus logistic regression for predicting medical outcomes. *J. Clin. Epidemiol.* **1996**, *49*, 1225–1231.
31. Mahmood, M.A.; Visan, A.I.; Ristoscu, C. and Mihailescu, I.N. Artificial neural network algorithms for 3D printing. *Materials* **2020**, *14* 163.
32. Logacjov, A.; Bach, K.; Kongsvold, A.; Bårdstu, H.B.; Mork, P.J. HARTH: A Human Activity Recognition Dataset for Machine Learning. *Sensors* **2021**, *21*, 7853.
33. Dirgová Luptáková, I.; Kubovčík, M.; Pospíchal, J. Wearable Sensor-Based Human Activity Recognition with Transformer Model. *Sensors* **2022**, *22*, 1911.
34. Bracali, A.; Barbani , D.; Baldanzini, N. Feasibility study for the estimation of a motorcycle helmet Centre of Gravity accelerations with 6 Degrees of Freedom (6DOF) system. *Transp. Res. Interdiscip. Perspect.* **2022**, *14*, 100603.
35. Piantini, S.; Pierini, M.; Delogu, M.; Baldanzini, N.; Franci, A.; Mangini, M.; Peris, A. Injury analysis of powered two-wheeler versus other-vehicle urban accidents. In Proceedings of the IRCOBI Conference, Malaga, Spain, 14–16 September 2016.
36. Aldman, B.; Lundell, B.; Thorngren, L. Oblique impacts, a parametric study in crash helmets. In Proceedings of the IRCOBI (International Research Committee on Biokinetics of Impacts) Conference, Bron, France, 12–14 September 1978.
37. Mills, N.J.; Wilkes, S.; Derler, S.; Flisch, A. FEA of oblique impact tests on a motorcycle helmet. *Int. J. Impact Eng.* **2009**, *36*, 913–925.
38. Meng, S.; Cernicchi, A.; Kleiven, S.; Halldin, P. High-speed helmeted head impacts in motorcycling: A computational study. *Accid. Anal. Prev.* **2020**, *134*, 105297.
39. Iman, R.L.; Conover, W.J. Small sample sensitivity analysis techniques for computer models. with an application to risk assessment. *Commun. -Stat.-Theory Methods* **1980**, *9*, 1749–1842.
40. Giudice, J.S.; Kong, K.; Caudillo, A.; Mukherjee, S.; Panzer, M.B. User Manual-Finite Element Models of helmet Assessment Tools (Hybrid III Head-Neck, NOCSAE Headform, Linear Impact, Pendulum Impact, Drop Impact-Version 1.0 for LS-DYNA. 2018. Available online: https://www.biocorellc.com/wp-content/uploads/2020/11/Manual_2016_Schutt_Air_XP_Pro_Helmet_Model_v1.0.pdf (accessed on 21 July 2022).
41. Medsker, L.R.; Jain, L.C. Recurrent neural networks. *Design Appl.* **2001**, *5*, 64–67.
42. Hochreiter, S.; Schmidhuber, J. Long short-term memory. *Neural Comput.* **1997**, *9*, 1735–1780.

43. *ISO 6487:2002*; Road Vehicles-Measurement Techniques in Impact Tests-Instrumentation. International Organization of Standardization: Geneva, Switzerland, 2002.
44. Werbos, P.J. Backpropagation through time: What it does and how to do it. *Proc. Name IEEE* **1990**, *78*, 3796883.
45. Ruder, S. An overview of gradient descent optimization algorithms. *arXiv* **2016**, arXiv:1609.04747.
46. Versace, J. *A Review of the Severity Index*; SAE Technical Paper; SAE: Warrendale, PA, USA, 1971.
47. Pike, J. *Biomechanical Risk Estimates for Mild Traumatic Brain Injury*; SAE: Warrendale, PA, USA, 2011.
48. Zhang, L.; Yang, K.H.; King, A.I. A proposed injury threshold for mild traumatic brain injury. *J. Biomech. Eng.* **2004**, *126*, 226–236.

Chapter 5

Validation of the methodology through experimental data

In this Chapter, the new methodology, based on Artificial Neural Networks (ANNs), introduced in Chapter 4 is validated through experimental tests. The first part of the Chapter investigates how the number of sensors and their location and orientation affect the head kinematics prediction. Then, the experimental tests performed to assess the representativeness of the data used to train the ANNs are discussed. Finally, experimental and simulation data are given as input to ANNs to predict the head accelerations and a comparison between experimental and predicted kinematics is performed.

Results show that a minimum number of 5 accelerometers normal oriented to the helmet shell should be adopted for this technology. In addition, a fair to good agreement between simulated and experimental data is obtained (CORA scores ranging from 0.42 and 0.65 for the 4 impact configuration analysed) confirming that the helmet model used in this work represents in an acceptable way the behaviour of the AGV X3000 helmet. Results also show that ANNs trained using only numerical data can be exploited with real world data. This represents an important achievement for the development of a technology to predict TBIs in real time and a relevant contribution to the state of the art concerning the adoption of automatic emergency call system (eCall) in Powered Two-Wheeler (PTW) vehicles.

5.1 Method

The method to estimate the head kinematics (for simplicity called Method to Estimate Head Kinematics (MEHK) from now on) described in Chapter 4 used twelve accelerometers attached to the helmet outer shell in orthogonally oriented pairs at six different locations. The sensing axis of each accelerometer was oriented tangentially to the head skull. Data acquired by these sensors were given as input to two different ANNs able to estimate respectively the linear and rotational accelerations of the head Centre of Gravity (CoG). A representative set of impact conditions was defined and reproduced in a virtual environment, to generate data

used to train the ANNs exploited by MEHK (Chapter 4). The same FE model of helmet described in Chapter 3 and the ANN architecture analysed in Chapter 4 were used in this study. The helmet model was modified for this work: the 16 pairs of single-axis accelerometers (Figure 5.1) were replaced by 16 single axis accelerometers with their sensing axes oriented orthogonally to the helmet surface. The same training, validation and testing datasets (Chapter 4) were reproduced using the updated model. Finally, the acceleration components required by MEHK were selected among these 16 accelerometers and several ANNs were implemented (Table 5.1).

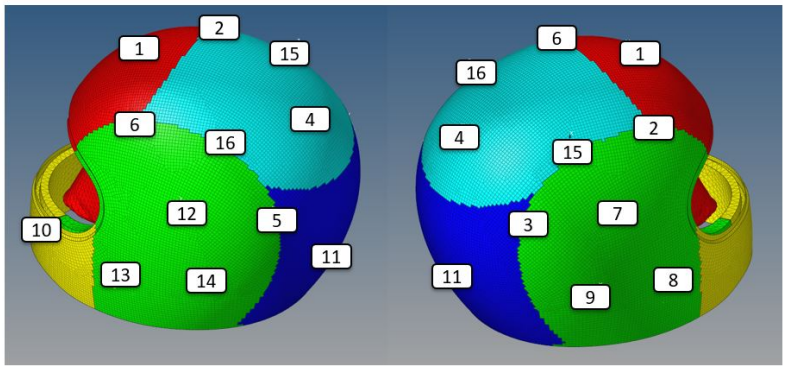

Figure 5.1: Locations of the 16 accelerometers orthogonally oriented to the helmet surface.

Performances were evaluated in multiple steps: first, five random distributions of 12 accelerometers (N12C1-N12C5 shown in Table 5.1) were selected to investigate their influence on the ANNs prediction. Then, Root Mean Square Error (RMSE) obtained during the training process and coefficients of determination R^2 between the estimated parameters (acceleration peaks, HIC, RIC using MEHK) and their target values were assessed and compared with the original MEHK performances. In this chapter, no consideration about the correlation between the HIC / RIC and head injuries will be analysed. Specifically, these two parameters were used to compare the estimated and target curves in a similar manner, as RIC and HIC exploit the same equation. Then, a new distribution of 12 randomly selected accelerometers (N12 shown in Table 5.1) was chosen to investigate how the number of accelerometers affected the results. The accelerometers were sequentially removed from #1 to #14 (N11-N1 shown in Table 5.1). Eleven new ANNs with a decreasing number of inputs (from 11 to 1) were trained both for the linear and rotational accelerations for a total of 22 ANNs; these ANNs shared the same architecture of the initial ANNs. Finally, performances of these ANNs were assessed with the same metrics mentioned before (RMSE and R^2).

Experimental tests

The numerical approach exploited in the first part of this work was used to deepen the influence of the number of accelerometers, their orientation and their position on the helmet shell, on the head kinematics estimation. Once the best combination of accelerometers was identified, experimental tests were performed to

Table 5.1: ANNs implemented and investigated in this work. For each ANN, a different set of accelerometers was selected and their locations on the helmet shell are listed in this Table. All the 16 locations of the accelerometers can be found in Figure 5.1

ANN	Accelerometer configuration
N12C1	2 3 4 6 7 9 10 11 12 13 15 16
N12C2	1 2 4 5 7 8 9 10 11 12 14 16
N12C3	1 2 3 4 5 7 9 10 12 13 14 16
N12C4	2 4 5 6 8 9 10 11 13 14 15 16
N12C5	1 2 3 5 6 7 10 11 12 13 15 16
N12	1 3 4 5 6 7 8 9 11 12 14 15
N11	3 4 5 6 7 8 9 11 12 14 15
N10	4 5 6 7 8 9 11 12 14 15
N9	5 6 7 8 9 11 12 14 15
N8	6 7 8 9 11 12 14 15
N7	7 8 9 11 12 14 15
N6	8 9 11 12 14 15
N5	9 11 12 14 15
N4	11 12 14 15
N3	12 14 15
N2	14 15
N1	15
N5F	1 5 8 10 11

explore the applicability of the methodology with real-world data.

First of all, the representativeness of the finite element model used to generate data for the training of the ANNs was investigated, using three AGV X3000 helmets for a total of 12 impact tests. The tests were performed at Dainese S.p.A laboratory and at the Head laboratory at the Imperial College of London (ICL). A monorail shock absorption test rig developed for helmet testing was exploited. A Hybrid III headform was equipped with nine accelerometers in a 3-2-2-2 orientation [125], which allowed the acquisition of linear and rotational head Centre of Gravity (CoG) accelerations. From the accelerometer numerousness study previously described, 5 accelerometers were considered enough to obtain an acceptable estimation of the head accelerations (further information can be found in the Results and Discussion sections). Therefore, the helmet was instrumented with 5 micro-electromechanical systems (MEMS) accelerometers attached on the inner surface of the helmet shell. Specifically, TE connectivity *model 52* accelerometers were used in the experimental tests; their measurement range was $\pm 2000g$ and they could withstand a shock up to $5000g$. From the 16 locations shown in Figure 5.1, accelerometers were attached in positions 1-5-8-10-11. Since the helmet was a symmetric component, locations were selected to have data from chin (10), upper-front (1), upper-back (5), back (11) and lateral (8) areas.

From the finite element model of the helmet (Figure 5.1), a scaled outer shell with small holes at the 5 selected accelerometer locations was printed using the Stratasys F370 3D printer, Fused filament fabrication (FDM) technology. Specifically, this printed model was used as a jig to identify and mark the locations 1-5-8-10-11 on the surface of the helmets used for the experimental tests (Figure 5.2 (a)). Then,

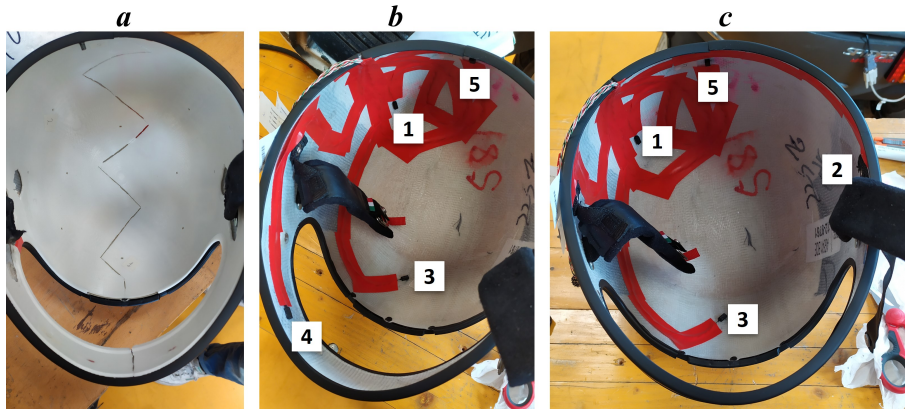

Figure 5.2: (a) Accelerometer location identification using a 3D printed scaled helmet outer shell, (b-c) Instrumented helmet: the five accelerometers #1, #2, #3, #4 and #5 were respectively attached in positions 3, 8, 1, 11 and 5 (Figure 5.1).

the 3D printed liner was removed from the helmet and the accelerometers #1, #2, #3, #4 and #5 were respectively attached in positions 5, 8, 1, 10 and 11 (Figure 5.2 (b-c)). This method ensured high accuracy in determining the positions of the accelerometers on the inner surface of the helmet, and thus good reproducibility of the tests.

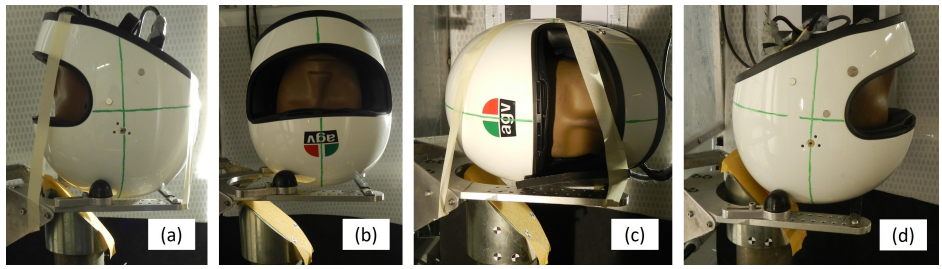

Figure 5.3: Impact test scenarios: (a) upper-front (UF), (b) upper-left (UL), (c) right (R) and (d) back (B).

From here onwards data extracted from the Hybrid III headform (the 6 head kinematics components) and the ones from the 5 accelerometers attached to the helmet will be referred as Head data and Helmet data respectively. Head and Helmet data were sampled at 20000Hz and filtered using respectively a Butterworth low pass filter with a cut-off frequency of 1000 Hz and a SAE 600 filter [126]. Tests were performed with an impact speed of 7.75m/s with a standard deviation of 0.0732. For each helmet, 4 different impact scenarios were tested: upper-front (UF), upper-left (UL), back (B) and right (R) shown respectively in Figure 5.3 (a), (b), (c), (d); these tests provided differentiated data comprehensive of impacts into the helmet front, back and lateral areas. All tests were performed using a 45° anvil. Only oblique impacts were investigated to generate both head linear and rotational acceleration data, as the methodology here discussed aims to predict all the head kinematics components.

Model accuracy was evaluated in multiple ways: first, CORA [127], an objective comparison metric, was used to quantify how accurate were the numerical trends compared to the target ones. CORA is based on two different methods: the corridor and the cross-correlation method. The first method assigns a score based on where the simulation curve falls in relation to corridors around the mean experimental curve. The second method is based on ratings for the phase shift, size, and shape of the predicted curves. Phase shift is influenced by the data synchronisation, while the size, assessed comparing the area below the two curves, can give totally incorrect errors when both curves have trends close to 0 for the entire time duration. Therefore, only the corridor method was considered to assess the accuracy of the predicted curves. The output of the corridor method ranges between 0 and 1 (1 indicates a perfect match). In addition, the numerical trends were properly shifted to be compared with the target curves. The inner corridor required by the CORA metric was generated using the envelope of the 3 tests repeated for each impact configuration, as the 3 repetitions show the variability of the experimental tests performed. When the predicted curve falls into the inner corridor, the prediction can be considered perfect (accuracy = 1). The outer corridor was obtained by doubling the values of the internal corridor.

The FE model of helmet used in this work was validated by AGV company using impact tests according to the ECE 22.05. As a result, the validation focused on finding a good agreement between experimental and simulated head accelerations, without investigating how impact waves would propagate into the outer shell after the impact. This reflected on the Helmet signals obtained from finite element analyses, which are characterised by lower damping and a marked instability after the first $15ms$ after the impact. Therefore, a fixed time interval of 0-$15ms$ was selected to compare the curves. CORA scores were calculated both for 1) Helmet accelerations: CORA scores were assessed for all the 5 accelerometer curves and averaged to compute a single rating for each tested impact; 2) Head accelerations: CORA scores were calculated both for the six components and the two resultants. Then, two rating were assessed averaging respectively the components and the resultants. A future exploitation of this method could involve a subsequent module to estimate TBI using the six head acceleration components, as described in Chapter 6. On the other hand, an injury assessment could be done directly using injury criteria based on resultant linear and/or rotational accelerations such as the HIC. For this reason, two ratings were used to assess accuracy of the numerical head kinematics.

Then, Peak Translational Acceleration (PTA), Peak Rotational Acceleration (PRA), HIC and RIC for the numerical tests were assessed and compared with the target values. PTA is used in all helmet standards, while PRA has been suggested as a metric for predicting subdural hematomas [8]. HIC and RIC were chosen to assess linear and rotational trends in a similar manner, as these criteria exploit the same equation. Target values were calculated from reference curves generated by averaging the 3 experimental test repetitions.

Finally, experimental and numerical Helmet data were given as input to the N5F ANN (Table 5.1). N5F was implemented using as input the 5 accelerometers located in the same positions used to perform the experimental tests (1-5-8-10-11). Head linear and rotational acceleration curves were assessed using N5F and compared with the target ones. Again, CORA metric, PTA, PRA, HIC and RIC were used to assess the accuracy of the prediction.

Table 5.2: Effect of accelerometer orientation, position and numerousness in the linear peak values and HIC estimation and in the RMSE error obtained during the training process.

ANN	Pearson coefficient (R^2)					RMSE
	a_x	a_y	a_z	a	HIC	training process
REF	0.952	0.949	0.972	0.946	0.960	0.208
N12C1	0.939	0.918	0.970	0.921	0.955	0.217
N12C2	0.913	0.924	0.963	0.921	0.953	0.253
N12C3	0.948	0.956	0.972	0.946	0.962	0.214
N12C4	0.944	0.944	0.973	0.945	0.967	0.217
N12C5	0.933	0.926	0.959	0.910	0.956	0.223
N12	0.945	0.925	0.968	0.927	0.962	0.219
N11	0.951	0.922	0.970	0.930	0.967	0.217
N10	0.947	0.928	0.961	0.916	0.965	0.218
N9	0.942	0.932	0.963	0.920	0.957	0.229
N8	0.938	0.917	0.962	0.911	0.957	0.244
N7	0.932	0.917	0.955	0.921	0.953	0.243
N6	0.935	0.915	0.964	0.911	0.945	0.244
N5	0.935	0.918	0.968	0.921	0.938	0.255
N4	0.928	0.893	0.963	0.900	0.940	0.268
N3	0.888	0.887	0.942	0.874	0.917	0.306
N2	0.792	0.851	0.882	0.811	0.829	0.337
N1	0.721	0.025	0.899	0.582	0.512	0.653

5.2 Results

5.2.1 Influence of accelerometer orientation, position and numerousness

The influence of the accelerometer orientation, position and numerousness on the head linear acceleration estimation is shown in Table 5.2. Each ANN listed in Table 5.2 was employed to estimate the head linear acceleration, and the ANN developed for the original MEHK was considered as the reference configuration (REF). This configuration had a high accuracy in the linear acceleration estimation since the Pearson coefficient was close or greater than 0.95 for all the considered parameters (linear peak values and HIC, Table 5.2). The 5 configurations of randomly chosen accelerometers normally oriented to the helmet surface (N12C1-N12C5) had R^2 values in the range $0.910 - 0.973$. N12C2 produced the highest RMSE during the training process (0.253), instead the other configurations showed smaller values between 0.214-0.223.

Keeping the accelerometers in the normal position and decreasing their number from 12 to 1 resulted in a reduction of the Pearson coefficient for all the selected parameters and in an increment of the RMSE obtained during the training (Table 5.2). Indeed, RMSE gradually increased from configuration N12 ($RMSE = 0.219$) to N1 ($RMSE = 0.653$). This reflected on the accuracy of the linear acceleration estimation: if N12 had R^2 coefficients comprised between 0.925 and 0.927, N1 experienced a marked reduction in R^2 coefficients between 0 and 0.899 (if the values of a_y, which had a R^2 close to zero, is excluded, the range would be 0.512-0.899).

Table 5.3: Effect of accelerometer orientation, position and numerousness in the rotational peak values and RIC estimation and in the RMSE error obtained during the training process.

ANN	Pearson coefficient (R^2)					RMSE
	α_x	α_y	α_z	α	RIC	training process
REF	0.923	0.922	0.913	0.925	0.914	0.332
N12C1	0.877	0.890	0.838	0.880	0.882	0.387
N12C2	0.879	0.887	0.841	0.875	0.877	0.398
N12C3	0.875	0.892	0.808	0.873	0.867	0.401
N12C4	0.898	0.878	0.870	0.890	0.894	0.396
N12C5	0.870	0.896	0.845	0.855	0.842	0.436
N12	0.893	0.879	0.850	0.872	0.890	0.393
N11	0.872	0.885	0.857	0.862	0.879	0.399
N10	0.880	0.880	0.879	0.882	0.872	0.421
N9	0.863	0.895	0.841	0.868	0.865	0.404
N8	0.858	0.882	0.800	0.862	0.819	0.432
N7	0.861	0.872	0.802	0.857	0.820	0.458
N6	0.865	0.874	0.798	0.853	0.840	0.464
N5	0.848	0.847	0.801	0.811	0.817	0.516
N4	0.814	0.804	0.688	0.804	0.793	0.546
N3	0.745	0.789	0.660	0.762	0.714	0.573
N2	0.615	0.559	0.139	0.523	0.455	0.755
N1	0.014	0.494	0.025	0.176	0.147	0.943

Table 5.3 describes how the accelerometer orientation, position and numerousness affected the head rotational acceleration estimation accuracy. Again, the configuration of twelve accelerometers placed tangentially to the helmet shell (original MEHK) was considered as reference configuration (REF). It had R^2 coefficients ranging from 0.913 and 0.925 and a RMSE of 0.332. Changing the direction to the accelerometers (from tangential to normal to the helmet shell), performances had a slight drop. Configurations N12C1-N12C5, which had twelve accelerometers placed normally to the helmet shell, produced a RMSE during the training process ranging from 0.387 and 0.436. This resulted in R^2 values varying from 0.841 and 0.898 for the rotational acceleration peaks and RIC prediction.

The last 12 accelerometer configurations (N12-N1) of Table 5.3 showed how the numerousness of accelerometers affected the head rotational acceleration estimation. Decreasing the number of sensors, performances dropped as certified by the gradual increase of the RMSE (from a $RMSE = 0.393$ for N12 to a $RMSE = 0.943$ for N1). R^2 coefficients varied from values close to 0.9 in N12 to values close to 0 in N1.

5.2.2 Representativeness of FE model

Figures 5.4, 5.5, 5.6, 5.7 show the comparison between signals acquired by the 5 accelerometers attached to the helmet shell in the experimental tests and the corresponding numerical sensor accelerations respectively for the upper-front, upper-left, right and back scenarios (Figure 5.3). The comparison between the experimental and simulated head accelerations for the same scenarios can be found in Figures

Table 5.4: CORA scores for the Helmet accelerations. CORA scores were calculated for all the 5 accelerometer curves and averaged to compute a single rating for each tested impact

Impact scenario	CORA score					
	Acc. #1	Acc. #2	Acc. #3	Acc. #4	Acc. #5	Average
UF	0.61	0.46	0.32	0.52	0.41	0.46
UL	0.53	0.56	0.24	0.58	0.53	0.49
R	0.48	0.28	0.39	0.34	0.39	0.38
B	0.72	0.43	0.11	0.56	0.36	0.44

Table 5.5: CORA scores for the Head accelerations. CORA scores were calculated for all six acceleration curves and the two resultant curves. The first 6 scores (components) and the last 2 scores (resultants) were respectively averaged to compute two ratings (average components and average resultants, respectively Avg. comp. and Avg. res. in the Table) for each tested impact.

Impact scenario	CORA score									
	a_x	a_y	a_z	α_x	α_y	α_z	a	α	Avg. comp.	Avg. res.
UF	0.49	0.60	0.69	0.76	0.50	0.63	0.64	0.33	0.61	0.49
UL	0.37	0.42	0.21	0.52	0.49	0.89	0.10	0.40	0.48	0.25
R	0.64	0.68	0.65	0.66	0.56	0.48	0.59	0.52	0.61	0.56
B	0.59	0.88	0.52	0.77	0.71	0.41	0.69	0.64	0.65	0.67

Figures 5.8, 5.9, 5.10, 5.11. CORA scores of Helmet and Head curves estimation are shown respectively in Tables 5.4 and 5.5. Helmet and Head data were synchronised to properly investigate the representativeness of helmet FE model. It is important to note, that a shift in time does not affect the injury probability output, as it depends only on the curve within the time interval selected. This means that, considering two identical curves shifted, if the same portion of curve is considered, the injury probability will the same. The synchronisation between numerical and experimental Helmet data was obtained by matching the time instant the helmet impacted the anvil. Both numerical and experimental tests showed a temporal shift between Head and Helmet accelerations, as the impact occurred initially on the helmet shell and than on the headform. However, in the experimental test the time shift was different compared to the one obtained from the simulation. This was due to a slightly different distance of the headform from the helmet foam in the experimental and simulated test. Therefore, simulated Head curves were shifted to match the experimental trends.

For the UF scenario, the accelerometer #3 acquired the highest acceleration values (Figure 5.4). For this accelerometer, a good qualitative match can be observed between the experimental and the numerical trends: both time histories showed a first peak value followed by a minimum value and a steady trend close to 0 after 5ms. However, numerical peak values overestimated the experimental ones, reducing the overall CORA score equal to 0.32 (Table 5.4). In addition, the numerical minimum value had a time-lag compared to the minimum of the experimental signal.

Table 5.6: Experimental and numerical values of HIC and RIC for each impact configuration.

Impact scenario	HIC		RIC [10^4]	
	Experimental	Numerical	Experimental	Numerical
Upper-front	869 ± 197	1082	2083 ± 710	1155
Upper-left	904 ±115	1221	1777 ± 425	1186
Right	513 ± 264	849	3045 ± 1364	6505
Back	673 ± 177	928	1157 ± 337	1306

Table 5.7: Experimental and numerical values of PTA and PRA for each impact configuration.

Impact scenario	PTA [m/s^2]		PRA [rad/s^2]	
	Experimental	Numerical	Experimental	Numerical
Upper-front	1412 ± 207	1652	8842 ± 928	7367
Upper-left	1480 ± 203	1682	8197 ± 671	8578
Right	1086 ± 320	1597	10581 ± 3728	16192
Back	1202 ± 195	1500	7423 ± 2886	8683

Accelerometers #1 and #5 had the smallest amplitudes. Finally, plots, #2, #4 and #5 showed a satisfactory match between experimental and numerical first local peak values, while the numerical signal fluctuated more than the experimental one after 5ms. Overall, the mean CORA score was equal to 0.46 for this scenario.

Experimental and simulation curves of the linear and rotational head accelerations displayed a close agreement in their time histories and their peak values (Figure 5.8). The majority of the predictions had fair to excellent fidelity (average CORA scores for the components and the resultants were respectively equal to 0.61 and 0.49, as shown in Table 5.5). Only the linear resultant acceleration had a marginal fidelity, with a CORA=0.33 (Table 5.5).

For the UL scenario (Figure 5.5), signals of accelerometers #1 and #5 had the smallest amplitudes, while the other accelerations had similar amplitudes. Numerical curves for accelerometers #2 and #4 fluctuated more than the experimental signals, resulting in overestimated local peaks. Simulated acceleration #3 underestimated the maximum value in correspondence of the impact at 5.5ms and it showed a temporal shifting after this point. Except for the accelerometer #3 (CORA=0.24), the other accelerations were predicted with a good accuracy (CORA$\geq$0.53).

Comparison between experimental and numerical head accelerations for the UL scenario is shown in Figure 5.9. Linear acceleration components obtained from the simulation slightly overestimated the experimental results. In addition, immediately after the impact, numerical curves of the linear acceleration showed a more rapid increase than the corresponding experimental curves. The same considerations applied to the resultant linear acceleration. This led to a marginal fidelity (CORA ranged between 0.10 and 0.42 for the linear accelerations, as shown in Table 5.5). Except for α_z, experimental and simulation curves of the head rotational acceleration were in a good agreement (CORA$\geq$0.40).

For the R scenario (Figure 5.6), accelerometer #1 had the best agreement between simulation and experimental curves (CORA=0.48). Simulation curves of accelerometers #2 and #4 well reproduced respectively only the first peak and

the first two peaks, while the remaining time history had higher fluctuations than the experimental curves, as confirmed by CORA scores ≤ 0.34. Finally, numerical curves of accelerometers #3 and #5 respectively underestimated and overestimated the experimental trends.

Numerical and experimental curves of the head accelerations for the R scenario showed different behaviours (Figure 5.10). a_y, a_z, a, α_z and α obtained from the simulation showed a rapid increment in the acceleration after the impact followed by a short plateau and a subsequent sharp fall. By contrast, the experimental curves had a more gradual rise, a larger plateau and gradual fall. Finally, experimental a_x and α_z had a negligible amplitude, unlike the numerical results, which overestimated these components. Overall, a good agreement between numerical and experimental accelerations was obtained (average CORA scores for the components and the resultants were respectively equal to 0.61 and 0.56, as shown in Table 5.5).

For the B scenario(Figure 5.7), numerical and experimental signals of accelerometers #1, #2, #4 and #5 well matched during the first 5ms, i.e. at the impact. After the first 5ms, numerical curves were affected by a higher fluctuation compared to the experimental curves, resulting in a greater amplitude especially for accelerometers #2 and #5. Overall, these four accelerometers showed a good fidelity with CORA scores ranging from 0.36 and 0.72). Instead, accelerometer #3 showed comparable amplitude for the numerical and experimental curves over the entire time history, but the worst matching (CORA=0.11). For this scenario, simulation curves of the head accelerations were within the acceptability range derived from the 3 experimental tests (Figure 5.11). Indeed, this scenario had the best average CORA both for the components (0.65) and for the resultants (0.67).

The numerical and experimental values of HIC and RIC for each impact configuration are shown in Table 5.6. Overall, Numerical assessment of HIC and RIC overestimated the experimental values, except for the RIC values in the upper-Front and upper-left configurations. PTA and PRA values (Table 5.7 showed a similar trend). Excluding the Right configuration, numerical PTA and PRA had a fair to excellent with the respective average target values, with prediction errors ranging from 4% to 24%.

5.2.3 Head acceleration prediction

Figures 5.12, 5.13, 5.14, 5.15 show the comparison between the head acceleration components predicted by the NF5 and the respective inner and outer corridor obtained from the experimental tests, respectively for the upper-front, upper-left, back and right scenarios (Figure 5.3). Each graph of Figures 5.12, 5.13, 5.14, 5.15 has 4 different head acceleration predictions derived giving to the NF5 different inputs: sensor accelerations extrapolated from the simulations (black dotted line, referred from now on as *predicted numerical*), signals acquired by the accelerometers during the tests performed on the first helmet at Dainese S.p.A and the other 2 helmets at ICL (green, red and orange lines, referred from now on respectively as *predicted exp(A)*, *predicted exp(B)*, *predicted exp(C)*)

For the UF scenario (Figure 5.12), *predicted numerical* was in a good agreement with the experimental results for a_x, a_z, α_y and α_z components (CORA ranged between 0.39 and 0.63 as shown in Table 5.8). In the remaining components, the *predicted numerical* showed a general overestimation trend. *Predicted exp(A), exp(B) and exp(C)* were in agreement with each other except for the *predicted exp(A)* in the α_x component. Finally, *predicted numerical* and the three *predicted*

Table 5.8: CORA scores for the predicted Head accelerations. CORA scores were calculated for all six acceleration curves and the two resultant curves. The first 6 scores (components) and the last 2 scores (resultants) were respectively averaged to compute two ratings (average components and average resultants, respectively Avg. comp. and Avg. res. in the Table) for each tested impact.

		CORA score									
Impact scenario		a_x	a_y	a_z	α_x	α_y	α_z	a	α	Avg. comp.	Avg. res.
TEST 1	exp_A	0.19	0.22	0.31	0.45	0.39	0.57	0.22	0.32	0.35	0.27
	exp_B	0.20	0.13	0.32	0.29	0.34	0.54	0.27	0.31	0.30	0.29
	exp_C	0.20	0.14	0.33	0.30	0.35	0.46	0.36	0.31	0.30	0.29
	Numerical	0.39	0.18	0.55	0.37	0.45	0.63	0.52	0.32	0.43	0.42
TEST 2	exp_A	0.41	0.20	0.08	0.21	0.36	0.80	0.34	0.43	0.34	0.38
	exp_B	0.59	0.12	0.29	0.23	0.34	0.56	0.40	0.28	0.35	0.34
	exp_C	0.47	0.20	0.24	0.34	0.27	0.70	0.31	0.19	0.37	0.25
	Numerical	0.63	0.28	0.28	0.36	0.28	0.66	0.26	0.35	0.41	0.31
TEST 3	exp_A	0.72	0.60	0.47	0.27	0.39	0.49	0.52	0.17	0.49	0.34
	exp_B	0.61	0.61	0.50	0.60	0.49	0.42	0.62	0.20	0.54	0.41
	Numerical	0.60	0.55	0.55	0.61	0.58	0.45	0.46	0.56	0.56	0.51
TEST 4	exp_A	0.52	0.15	0.64	0.25	0.71	0.33	0.59	0.66	0.43	0.62
	exp_B	0.58	0.37	0.49	0.35	0.73	0.50	0.59	0.68	0.50	0.64
	exp_C	0.60	0.46	0.51	0.33	0.74	0.48	0.60	0.62	0.52	0.61
	Numerical	0.56	0.60	0.67	0.44	0.66	0.57	0.65	0.68	0.58	0.66

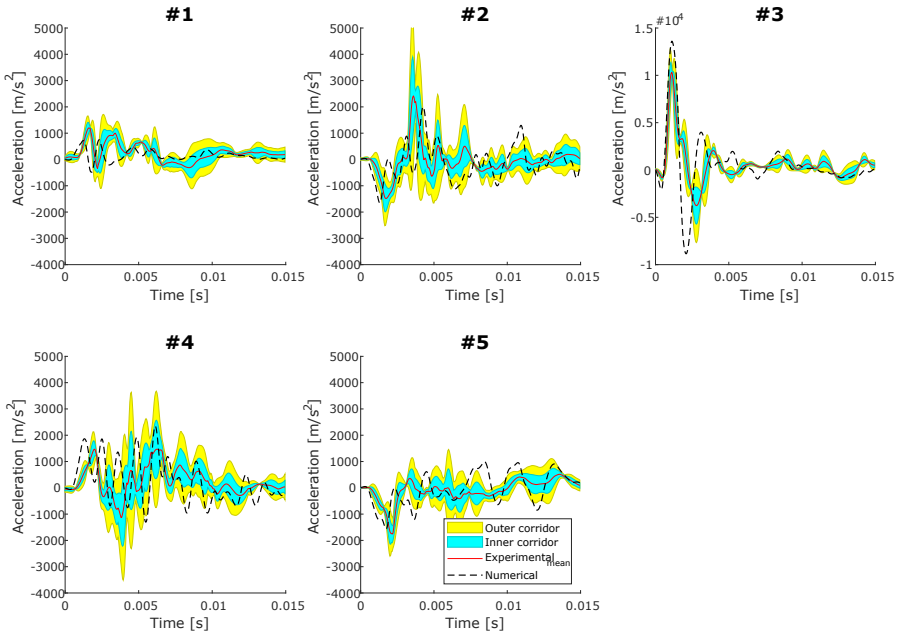

Figure 5.4: Representativeness of the FE model against the UF experimental test, in terms of Helmet accelerations. The cyan shaded area represents the variability of the three experimental tests performed for each impact configuration (inner corridor), the yellow area is the outer corridor, the red line is the mean value across these 3 tests and the black dotted line is the numerical simulation. From top left to bottom right: accelerometers #1, #2, #3, #4 and #5.

exp well matched each others except for the linear acceleration along the Z axis and the rotational acceleration around the X axis, where the *predicted exp* curves had greater values than the *predicted numerical* curves.

For the UL scenario (Figure 5.13), *predicted numerical* curves had a good match with the three *predicted exp* curves except for α_y. a_x and α_z showed the best matching between the predicted curves and the experimental tests, as confirmed by the highest values assumed by the CORA score for these two components (Table 5.8). Predicted linear accelerations are underestimated compared to the target trend, as shown by the resultant acceleration graph (Figure 5.13).

For the R scenario (Figure 5.14), *predicted exp(B)* and *predicted exp(C)* were in a good agreement except for the rotational accelerations around X and Y axes. Excluding a_x, the *predicted exp* curves poorly matched with the *predicted numerical* curves. The impact kinematics was mainly along Y and Z axes and around X axis, therefore a_y, a_z and α_x were the components with the larger amplitudes and a good qualitative match between the predicted numerical curve and the experimental bounded area can be observed (CORA values ranging between 0.55 and 0.61, as shown in Table 5.8).

For the B scenario (Figure 5.15), the linear accelerations along X and Z axes and the rotational acceleration around the Y axis were the components with the

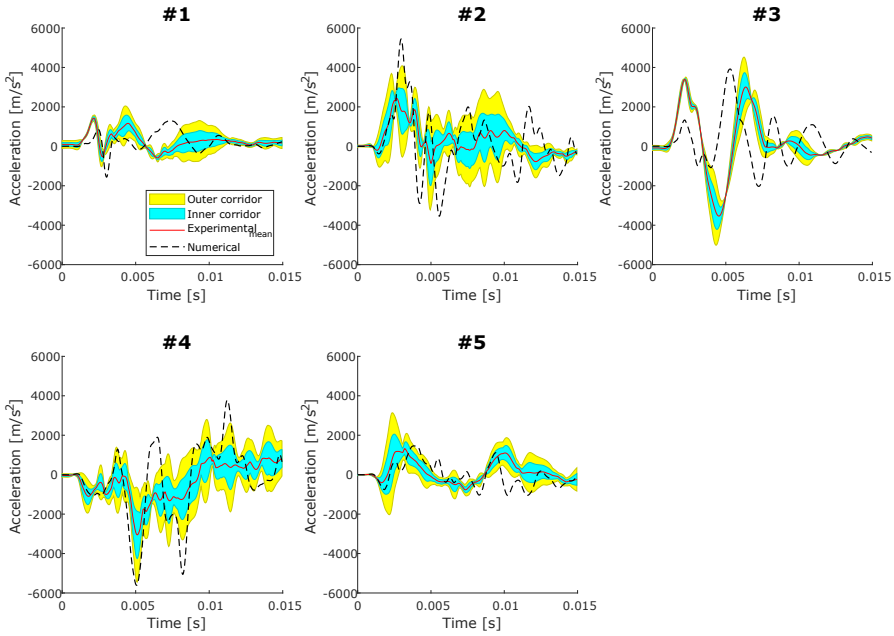

Figure 5.5: Representativeness of the FE model against the UL experimental test, in terms of Helmet accelerations. The cyan shaded area represents the variability of the three experimental tests performed for each impact configuration (inner corridor), the yellow area is the outer corridor, the red line is the mean value across these 3 tests and the black dotted line is the numerical simulation. From top left to bottom right: accelerometers #1, #2, #3, #4 and #5.

larger amplitudes. Overall, these main components showed the best agreement with the target trends, as confirmed by CORA values ranging from 0.51 to 0.74 (Table 5.8). In addition, the negligible component of the rotational acceleration α_x was incorrectly predicted by each of the four predicted curves.

Finally, the numerical and experimental values of PTA, PRA, HIC and RIC for each impact configuration are shown in Table 5.9. *Predicted exp(A), exp(B) and exp(C)* showed similar values among each others in most of the impact configuration analysed. One exception is *Predicted exp(A)* in the Upper-front configuration, which showed a PRA of $12637 rad/s^2$ compared to a PRA values of $18311 rad/s^2$ and $18885 rad/s^2$ shown by *exp(B) and exp(C)*. Consequently, the same considerations apply to RIC. On the other hand, most of the *predicted numerical* values were not in line with the target ranges (Table 5.9).

5.3 Discussion

This study investigates the feasibility of a new technology, based on neural networks, to estimate the head kinematics with sensors attached to the inner surface of a helmet outer shell (Chapter 4). Virtual simulations were employed to analyse the influence of accelerometer orientation, position and numerousness on the head

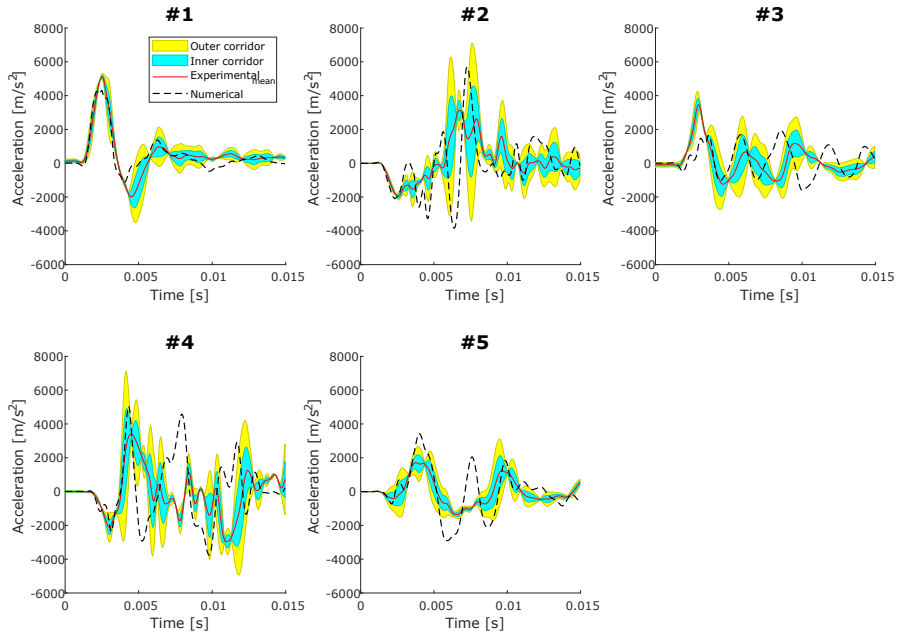

Figure 5.6: Representativeness of the FE model against the R experimental test, in terms of Helmet accelerations. The cyan shaded area represents the variability of the three experimental tests performed for each impact configuration (inner corridor), the yellow area is the outer corridor, the red line is the mean value across these 3 tests and the black dotted line is the numerical simulation. From top left to bottom right: accelerometers #1, #2, #3, #4 and #5.

kinematics estimation, while experimental tests were performed to investigate the representativeness of data used to develop the technology and to validate the methodology.

Results showed that reorienting the accelerometers normally to the helmet shell slightly decreased the accuracy in the estimation of the rotational accelerations. For example, R^2 coefficients reduced from the range 0.913-0.925 (REF configuration) to the range 0.841-0.898 (N12C1-N12C5), as shown in Table 5.3. This did not applied to the linear accelerations which was not affected by the change in orientation of the accelerometers (Table 5.2). Despite performances in the head rotational acceleration deteriorated, single axis accelerometers can be easier attached with their axes normal oriented to the helmet shell. Therefore, the normal direction should be preferred to the tangential direction.

The 6 ANNs with 12 normal oriented accelerometers (N12C1-N12C5 and N12) had similar results among each other, both for the linear (Table 5.2) and rotational (Table 5.3) kinematics. This suggested that performances are not affected by the accelerometer locations, if they are placed far enough to be considered located in different areas of the helmet shell.

Starting from a configuration of twelve accelerometers normal oriented to the helmet shell (N12, Table 5.1), the influence of the accelerometer numerousness on

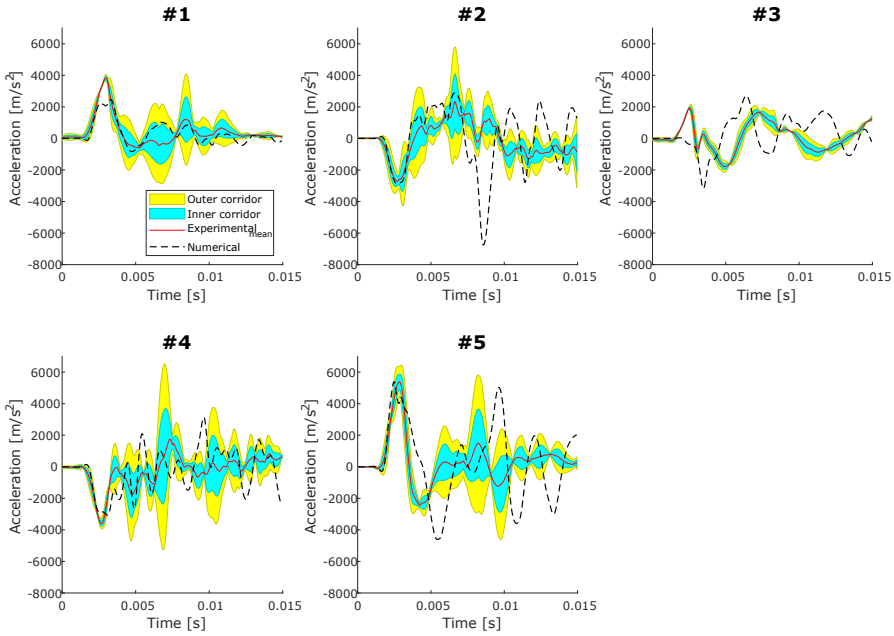

Figure 5.7: Representativeness of the FE model against the B experimental test, in terms of Helmet accelerations. The cyan shaded area represents the variability of the three experimental tests performed for each impact configuration (inner corridor), the yellow area is the outer corridor, the red line is the mean value across these 3 tests and the black dotted line is the numerical simulation. From top left to bottom right: accelerometers #1, #2, #3, #4 and #5.

the kinematic estimation performances was investigated. Decreasing the number of accelerometers from 12 to 5 led to a slightly drop in performances, while a number of accelerometers between 1 and 4 generated poor results. The last configuration with acceptable error can be considered the N5, which showed R^2 coefficients still above 0.9 (from 0.915 to 0.968) for the linear acceleration estimation (Table 5.2) and above 0.8 (from 0.801 to 0.848) for the rotational acceleration estimation (Table 5.3). Thus, a number of accelerometers equal to 5 was considered as the minimum number of sensors required by this technology. Similar results were also obtained by Ghajary [128], who investigated how the numerousness of accelerometers would affect the outcome of a technology, based on ANNs, to reconstruct the force time history of impacts. His work showed how performances slightly degraded decreasing the number of accelerometers from 12 to 4. However, the error reduction obtained increasing the number of accelerometers by Ghajary [128] was negligible compared to the one found in this study. This can be explained by the different complexity of the mechanical structure used in the two studies: Ghajary [128] used a sensorised composite stiffened panel, i.e. a monolithic structure, while this thesis uses a head-helmet assembly, which involves many interfaces (headform - foam, foam - helmet shell, helmet shell - ground). In addition, sensors are attached to a first body (the helmet outer shell) and the ANNs aim to predict the accelerations of a

Table 5.9: Experimental and numerical values of PTA, PRA, HIC and RIC for *Predicted exp(A), exp(B), exp(C) and predicted numerical* of each impact configuration.

Impact scenario	Parameter	exp_A	exp_B	exp_C	*Predicted numerical*	Target
Upper-front	PTA	4141	3882	3563	2446	1412 ± 207
	PRA	12637	18311	18885	13042	8842 ± 928
	HIC	6308	6113	5212	2462	869 ± 197
	RIC [10^4]	3679	8641	9844	4423	2083 ± 710
Upper left	PTA	718	809	917	726	1480 ± 203
	PRA	7671	8723	6883	6691	8197 ± 671
	HIC	228	272	319	219	904 ± 115
	RIC [10^4]	1892	2053	1259	1306	1777 ± 425
Right	PTA	534	639	/	1976	1086 ± 320
	PRA	7340	7192	/	14296	10581 ± 3728
	HIC	69	106	/	1495	513 ± 264
	RIC [10^4]	1435	1128	/	5324	3045 ± 1364
Back	PTA	1756	2026	2114	1524	1202 ± 195
	PRA	9234	10395	7788	7239	7423 ± 2886
	HIC	1306	1725	1825	980	673 ± 177
	RIC [10^4]	2023	2001	750	1367	1306 ± 337

second body (head).

Data used to train ANNs discussed above consisted in Helmet acceleration data (i.e accelerations of specific areas of the helmet recorded by uniaxial accelerometers glued to the helmet shell) and Head acceleration data recorded using a Hybrid III headform. Specifically, these data were entirely obtained from FE simulations. This raised a question about the representativeness of the FE model of the helmet used in this thesis: can the ANNs trained using numerical data be used for real-world applications? This question was addressed reproducing 4 oblique impacts with the same helmet model exploited in the simulations and comparing the results with the corresponding simulations. First of all, results showed a good repeatability of the experimental data. Indeed, for each impact configuration, 3 helmets were tested and therefore 3 curves were available for each parameter analysed. The range of variability was obtained from the envelope of the 3 curves and it was highlighted with a cyan shaded area in each plot from Figure 5.4 to 5.11. Overall, the width of this cyan band remained thin over the entire time history both for the Helmet data (Figures 5.4, 5.5, 5.6, 5.7) and the Head data (Figures 5.8, 5.9, 5.10, 5.11).

Looking to the comparison between the experimental and simulated Helmet accelerations (Figures 5.4, 5.5, 5.6, 5.7), data well matched in the first few milliseconds, i.e at the impact. For instance, most of the graphs in Figures 5.4, 5.5, 5.6, 5.7 showed a good agreement between the first peak values caused by the impact. Instead, after the impact, the numerical acceleration fluctuated more than the experimental acceleration and the matching between the curves worsened. This difference can be due to the different combination of waves recorded by the accelerometers: at the impact and immediately after it, sensors caught the strain wave, while the remaining time history was mainly affected by the propagation and reflection of the longitudinal and transversal waves. Modelling such a phenomenon in inhomogeneous

material is particularly complex and very time consuming, therefore it was not feasible including this task in the concept development of a new technology. A future optimization of the technology should consider a numerical approach that takes into account wave propagation in composite materials [129]. Despite the wave propagation limitation, the predicted curves showed fair to adequate fidelity (the average CORA scores calculated for the Helmet accelerations for each of the 4 impact configurations tested ranged between 0.38 to 0.49 as shown in Table 5.4).

Numerical and simulated data were synchronised with reference to the Helmet accelerations, as the first sensors to register the impact were those attached to the helmet shell. Indeed, the first impacted component during the experimental tests was the helmet shell, with the impact propagating towards the head through the foam. Once the helmet data were synchronised, numerical Head acceleration curves showed a time shift from the corresponding experimental acceleration curves. A potential reason for this is the different fit of the head inside the helmet. The numerical Hybrid III headform was fitted inside the helmet keeping a very small distance of a few millimetres between the head and the foam; in addition, only the lateral comfort liners were implemented. In the experimental tests, the Hybrid III headform was pushed towards the upper foam of the helmet and the comfort liners provided a solid coupling. Consequently, the experimental accelerations experienced a delay in time compared to the numerical results. However, a shift in time does not affect the injury probability output, as it depends only on the curve within the time interval selected. Therefore, numerical curves were shifted to properly match the experimental ones (Figures 5.8, 5.9, 5.10, 5.11).

Overall, numerical Head acceleration curves showed a good reproduction of the experimental trends, as confirmed by the average CORA scores ranging between 0.48 and 0.65 (components) and between 0.25 and 0.67 (resultants) for the four impact configurations analysed. In addition, Numerical PTA and PRA values well approximated the target values (Table 5.7) in 3 out 4 impact configurations, with most of the numerical values falling into the acceptable range of the target values. Same considerations applied to HIC and RIC values. On the other hand, R scenario showed the worst agreement with the target PTA, PRA, HIC and RIC. A possible explanation is that this impact configuration is not required by the ECE 22.05 standard, which was used to validate the helmet numerical model by SpA Dainese. Specifically, looking at the comparison between numerical and experimental accelerations for the R scenario of Figure 5.10, the resultant numerical acceleration shows a faster increase compared to the target one. This can be due to a higher stiffness of the foam in the numerical model compared to the one of the real helmet.

Prediction of head kinematics made providing to the N5F numerical and experimental Helmet accelerations is shown in Figures 5.12, 5.13, 5.14, 5.15. Overall, accelerations predicted using experimental signals (*exp(A), exp(B), exp(C)*) were in an excellent agreement between each others. For instance, Table 5.9 shows that most of PTA, PRA, HIC and RIC values of the predicted experimental curves were within a 15% of error between each others. In addition, kinematics predicted using numerical data had a good agreement with kinematics predicted using the experimental data except for the R scenario. This was expected as, except for the accelerometer #1, the R scenario had the poorest agreement between numerical and experimental Helmet accelerations (it was the only scenario showing an average CORA score below 0.40). Despite this exception, the good agreement between

numerical and experimental prediction confirmed that an ANN can be trained using only numerical data, without limiting its use with real-world data.

On the other hand, predictions made giving to the ANNs numerical Helmet data proved to be inconsistent with experimental results. For instance, numerical prediction of PTA, PRA, HIC and RIC values showed considerable errors when compared with the average target values (Table 5.9). Such a behaviour can only be attributable to a number of simulations (2000) too small for the considered wide range of head kinematics (up to $8000 m/s^2$ and $80 krad/s$). More in detail, ANNs provide the best result if training data provided to the neural networks during the training phase accurately describe the investigated solution domain. However, figure 5.16 shows a lack of data: for each of the 4 impacts tested, 2 scatter plots are given: the left one shows the comparison between the total amount of simulations used to train the network (each simulation is identified by its impact point on the helmet shell, marked with a black dot) and those simulations (identified by red dots) characterised by an impact point on the helmet outer shell enclosed in a sphere of radius 30mm from the impact point of the specific impact configuration considered; the scatter plot on the right shows the distribution of the impact speed and impact angle for the training configurations highlighted in red in the scatter plot on the left. For instance, figure 5.16 (a) represents the upper-front impact scenario: among the training simulations with the impact point located in this area, only one has an impact speed in the range 5.75-9.75m/s and an impact angle in the range $35° - 55°$ (these two ranges were selected because the four impact scenarios were tested with an impact speed of 7.75m/s and an impact angle of 45°. Similar considerations apply to the the upper-left and right scenario (Figure 5.16 (b) and (c)). Instead, the back scenario (Figure 5.16 (d)) shows the highest number of training simulations in these ranges of impact speed and angle (i.e. 6 simulations). This reflected on the results, as the ANN was able to predict with the highest accuracy the head kinematics in the back scenario. This is important to correctly interpret the results: the ANNs trained using only simulations can be exploited with experimental data as discussed in the previous paragraph, however a smaller range of head kinematics with a higher number of simulations should be considered to improve the prediction performances. Extremely high values of acceleration can be excluded as they lead to a really high probability of death, and this is the worst case scenario where unfortunately even this methodology is ineffective.

The results provided evidence that the main challenges for the methodology discussed in this Chapter are: 1) developing a FE model of helmet that guarantees a sufficiently accurate reproduction of both helmet and head accelerations; 2) selecting the optimal compromise between number of simulations and head kinematics range to maximise prediction performances without drastically increase calculation time to prepare the training dataset. The above discussed findings suggest at least that it is feasible to estimate head linear and rotational acceleration components from signals of sensors embedded into the helmet and at the same time far from the head. More important, ANNs can be used to transform the sensor signals into the head kinematics.

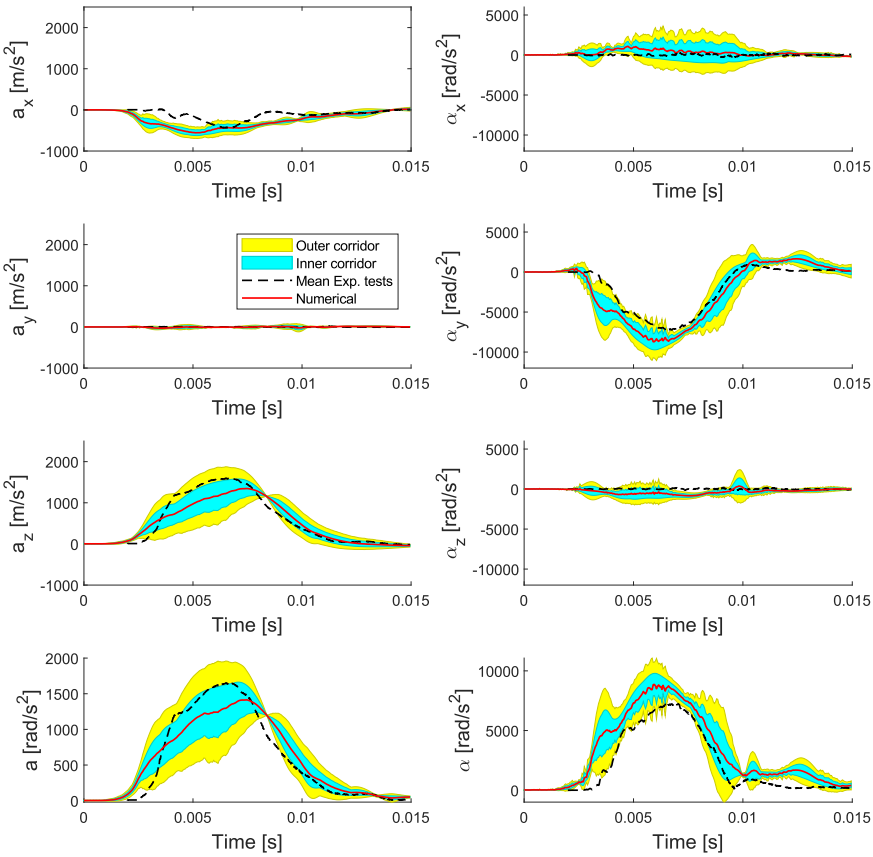

Figure 5.8: Representativeness of the FE model against the UF experimental test, in terms of Head linear acceleration (left side) and Head angular acceleration (right side). The cyan shaded area represents the variability of the three experimental tests performed for each impact configuration (inner corridor), the yellow area is the outer corridor, the red line is the mean value across these 3 tests and the black dotted line is the numerical simulation.

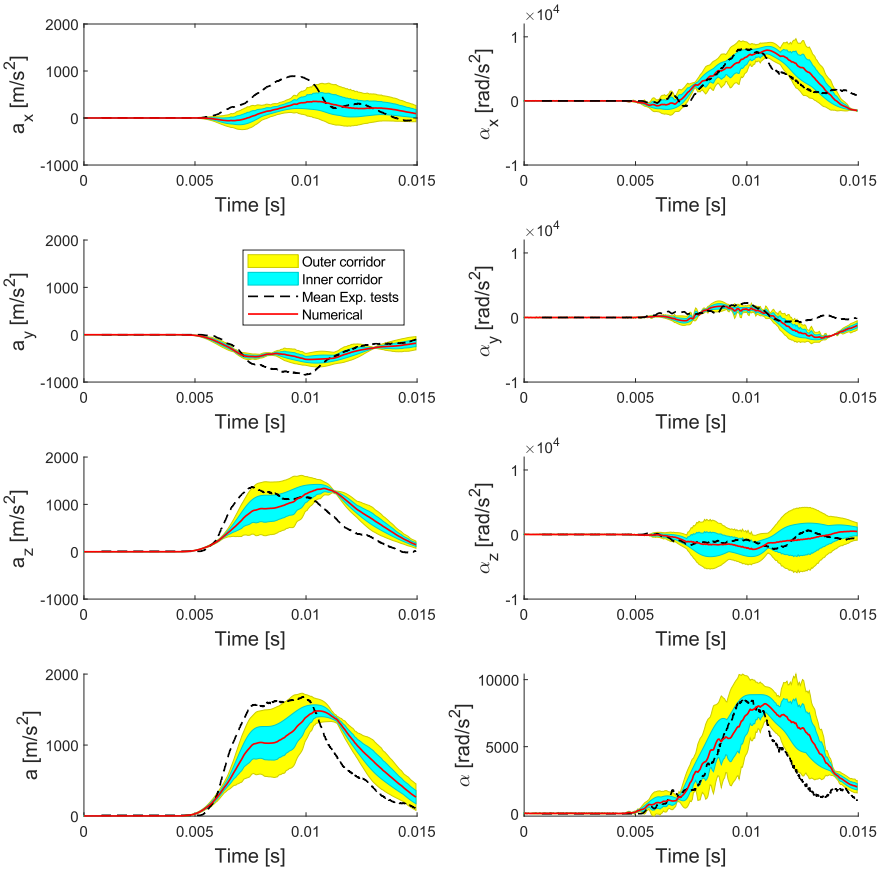

Figure 5.9: Representativeness of the FE model against the UL experimental test, in terms of Head linear acceleration (left side) and Head angular acceleration (right side). The cyan shaded area represents the variability of the three experimental tests performed for each impact configuration (inner corridor), the yellow area is the outer corridor, the red line is the mean value across these 3 tests and the black dotted line is the numerical simulation.

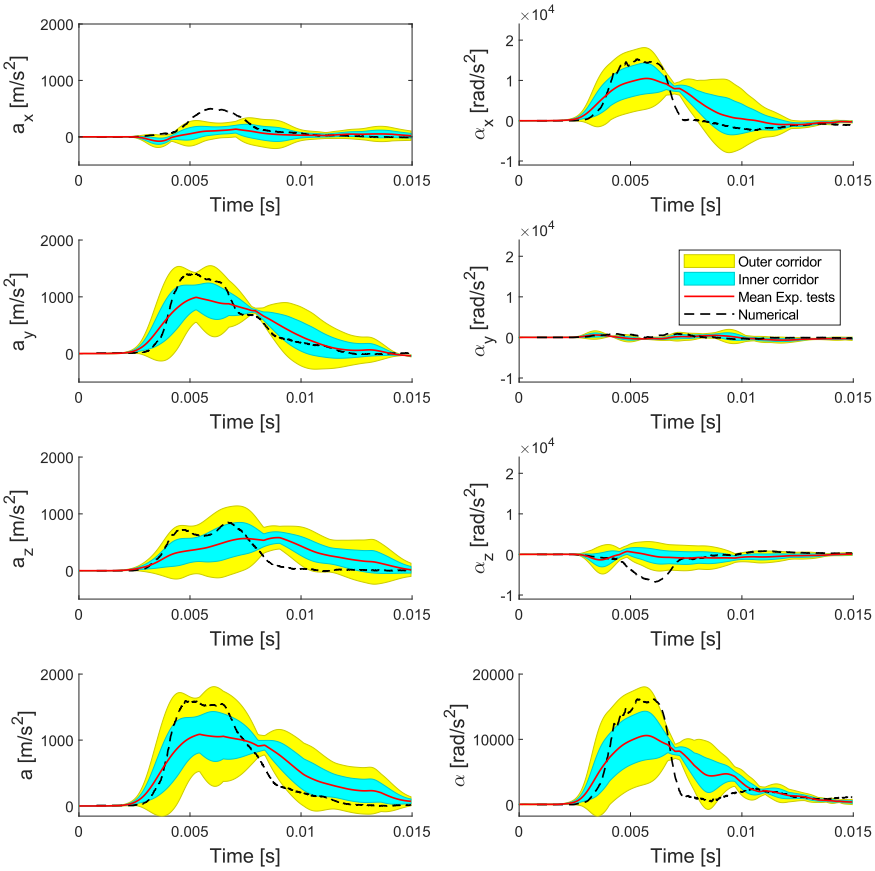

Figure 5.10: Representativeness of the FE model against the R experimental test, in terms of Head linear acceleration (left side) and Head angular acceleration (right side). The cyan shaded area represents the variability of the three experimental tests performed for each impact configuration (inner corridor), the yellow area is the outer corridor, the red line is the mean value across these 3 tests and the black dotted line is the numerical simulation.

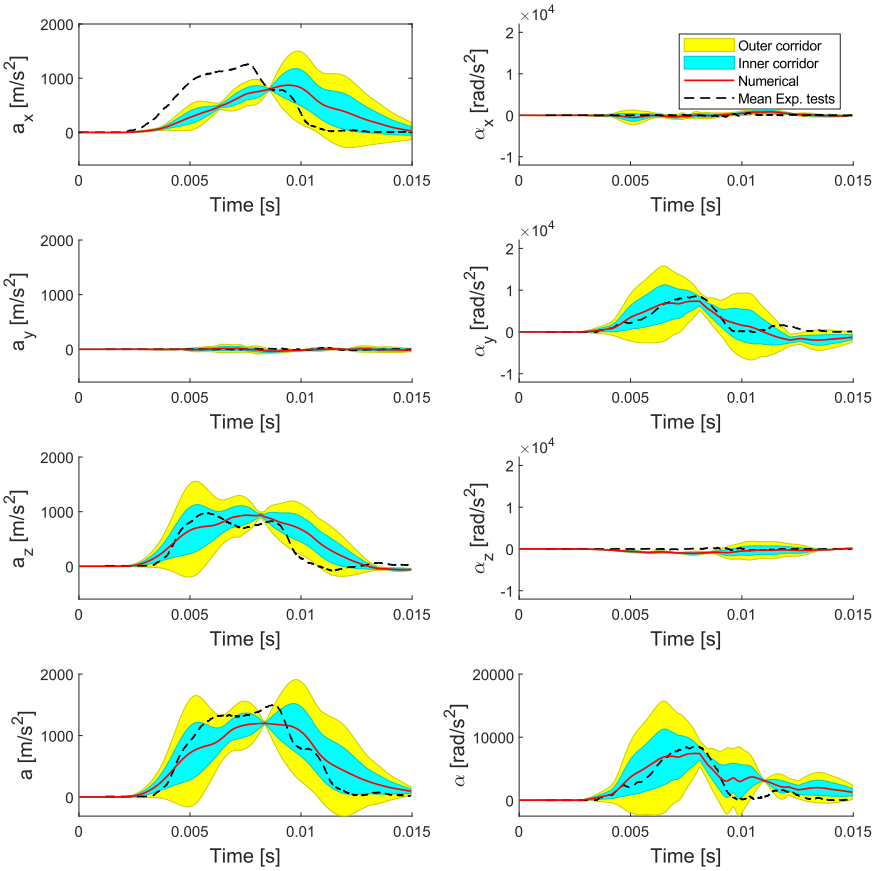

Figure 5.11: Representativeness of the FE model against the B experimental test, in terms of Head linear acceleration (left side) and Head angular acceleration (right side). The cyan shaded area represents the variability of the three experimental tests performed for each impact configuration (inner corridor), the yellow area is the outer corridor, the red line is the mean value across these 3 tests and the black dotted line is the numerical simulation.

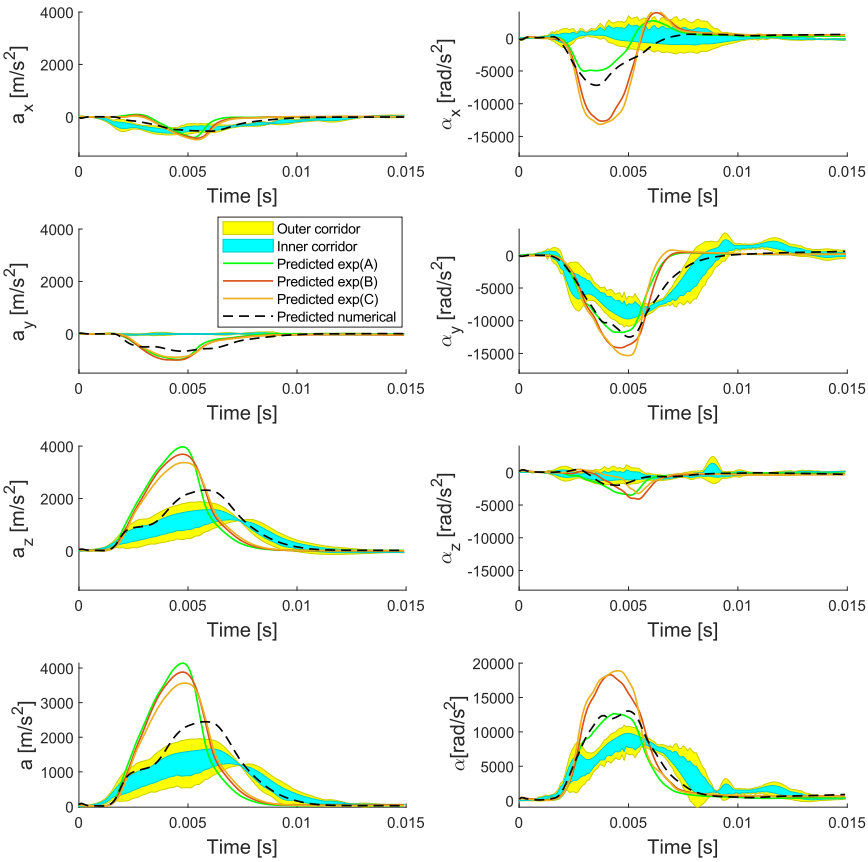

Figure 5.12: Head linear (left side) and rotational (right side) acceleration prediction using N5F for the UF scenario. The cyan shaded area represents the variability of the three experimental tests performed for each impact configuration (inner corridor), the yellow area is the outer corridor; the green, red and orange lines are the Head accelerations predicted using experimental inputs derived respectively from the test performed at Dainese S.p.A. and the two tests performed at ICL, the black dotted line is the Head acceleration predicted using numerical inputs.

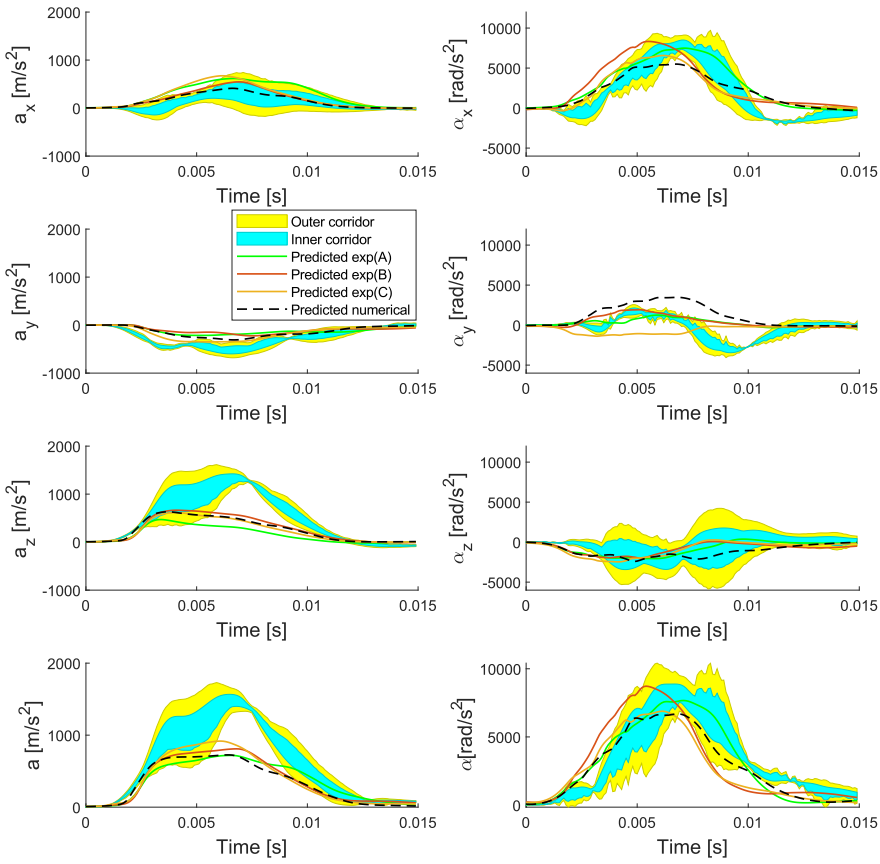

Figure 5.13: Head linear (left side) and rotational (right side) acceleration prediction using N5F for the UL scenario. The cyan shaded area represents the variability of the three experimental tests performed for each impact configuration (inner corridor), the yellow area is the outer corridor; the green, red and orange lines are the Head accelerations predicted using experimental inputs derived respectively from the test performed at Dainese S.p.A. and the two tests performed at ICL, the black dotted line is the Head acceleration predicted using numerical inputs.

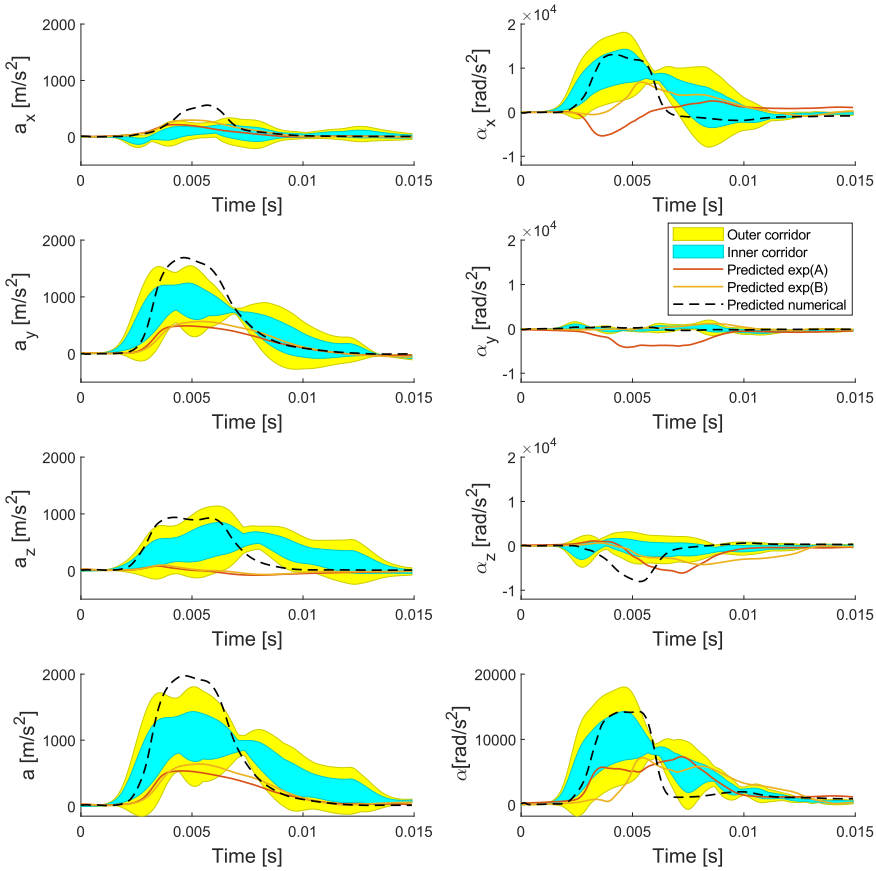

Figure 5.14: Head linear (left side) and rotational (right side) acceleration prediction using N5F for the R scenario. The cyan shaded area represents the variability of the three experimental tests performed for each impact configuration (inner corridor), the yellow area is the outer corridor; the green, red and orange lines are the Head accelerations predicted using experimental inputs derived respectively from the test performed at Dainese S.p.A. and the two tests performed at ICL, the black dotted line is the Head acceleration predicted using numerical inputs.

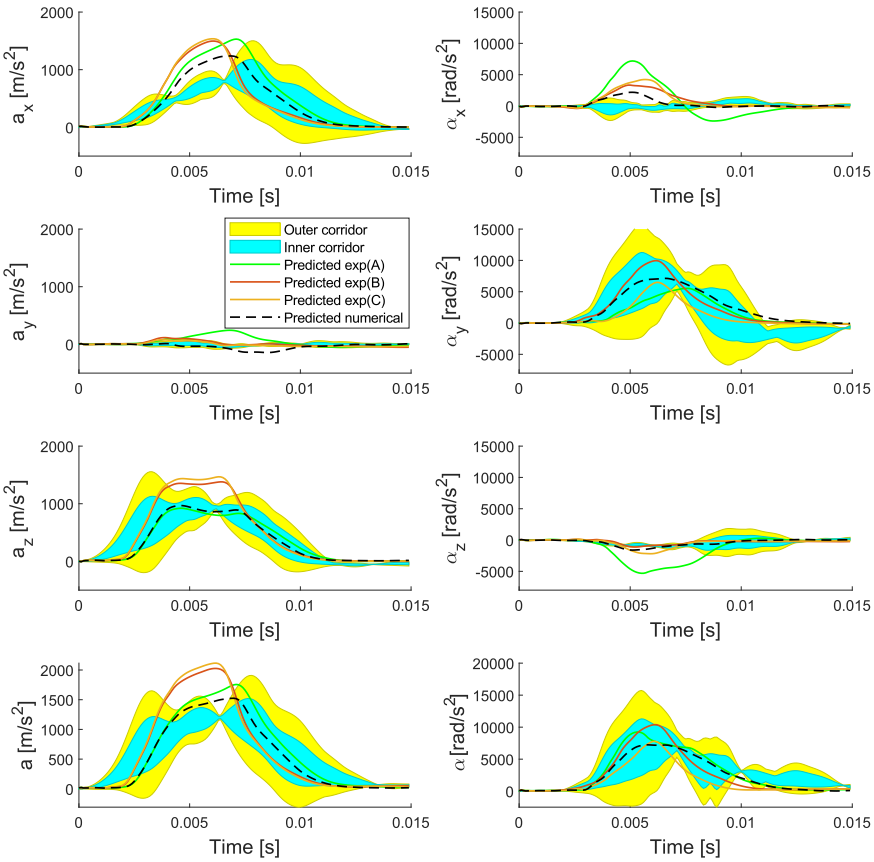

Figure 5.15: Head linear (left side) and rotational (right side) acceleration prediction using the N5F for the B scenario. The cyan shaded area represents the variability of the three experimental tests performed for each impact configuration (inner corridor), the yellow area is the outer corridor; the green, red and orange lines are the Head accelerations predicted using experimental inputs derived respectively from the test performed at Dainese S.p.A. and the two tests performed at ICL, the black dotted line is the Head acceleration predicted using numerical inputs.

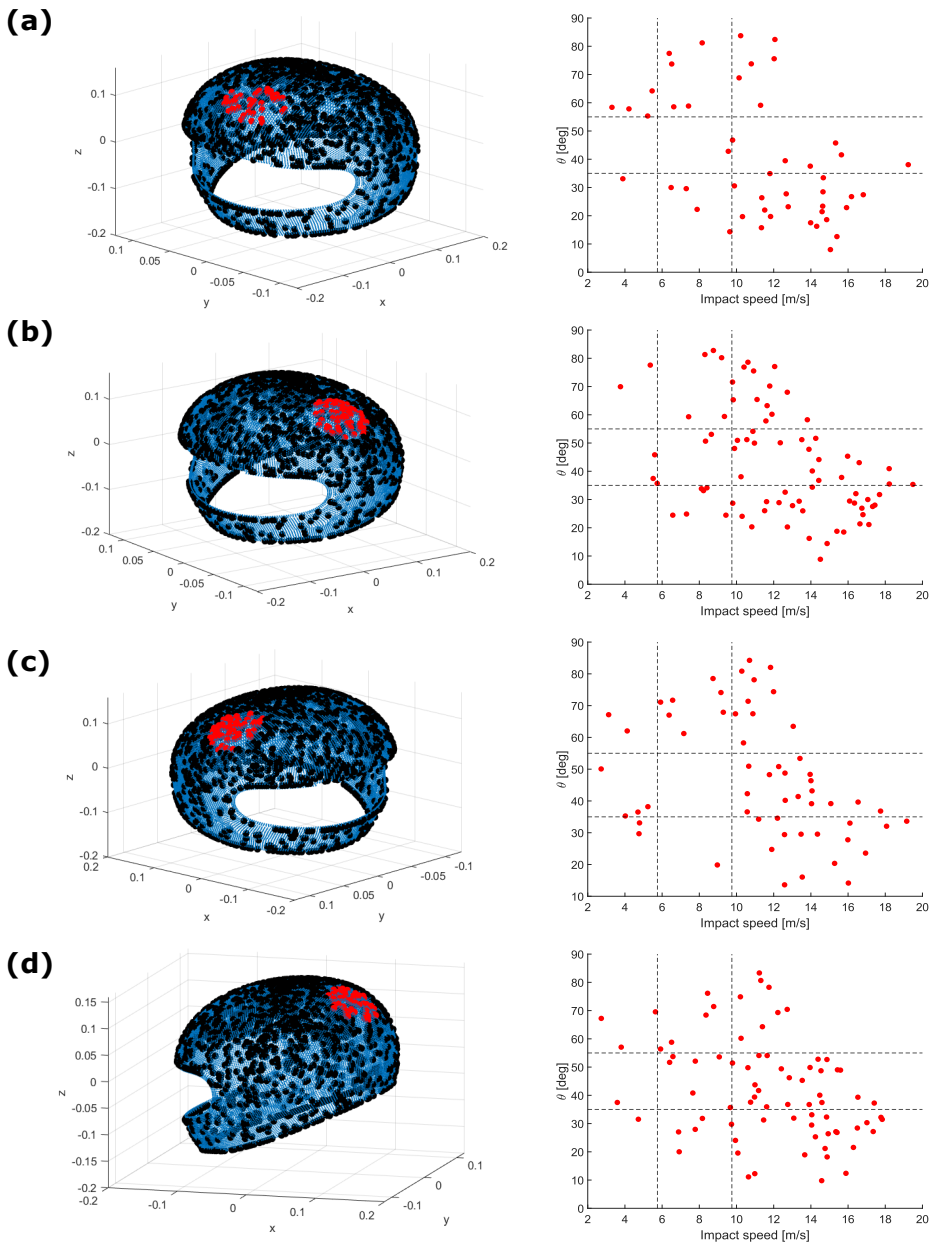

Figure 5.16: For each tested impact scenario (upper-front (a), upper-left(b), right (c) and back(d)), the left image represents the scatter plot of the shell mesh nodes (blue points), impact points for the entire training dataset (black points) and the impact points of the training dataset that are less than 30mm distance from the point of impact of the specific configuration tested (red points); the scatter plot on the right shows the distribution of the impact speed and impact angle for the training configurations highlighted in red in the left scatter plot. The two vertical lines indicate impact speeds corresponding to 5.75m/s and 7.75m/s. The two horizontal lines indicate impact angles corresponding to 35° and 55°.

Chapter 6

Regional brain strain and strain rate prediction

This Chapter addressed the fourth research question mentioned in the research process of Chapter 1: *Is it possible to make a real-time TBI estimation based on the head kinematics?* Recognising that Finite Element Modelling became the state of the art method to compute brain tissue response, a new approach was investigated to solve its main limitations: high computation time and complex computational software. A data-driven approach to predict strain and strain rate with a similar accuracy of a complex brain FE model, but with a calculation time of few milliseconds was investigated. The model consists of several Convolutional Neural Networks (CNNs) able to estimate strains and strain rates in key areas of the brain. CNNs were trained using as input Head kinematics data obtained from a representative set of impact conditions reproduced in a virtual environmental (Chapter 4). The same Head kinematics data were applied to the Centre of Gravity (CoG) of a human brain model and several brain simulations were carried out. As a result, strains and strain rates in key areas of the brain were extracted and used as output data for the CNNs training.

Results showed that a complex FE brain model can be replaced by CNNs trained using only numerical data and then exploited with real world data. In addition, CNNs trained using head kinematics data from simulated impacts of a specific model of motorcycle helmet can be used also for other models of helmets. This represents an important achievement for the development of a tool for the Traumatic Brain Injuries (TBIs) prediction and a relevant contribution to the state of the art concerning TBIs. This study was carried out at the 'Head Lab' department of the Imperial College London.

6.1 Method

The workflow of the model development and the performance assessment approach used in this study are shown in Figure 6.1.

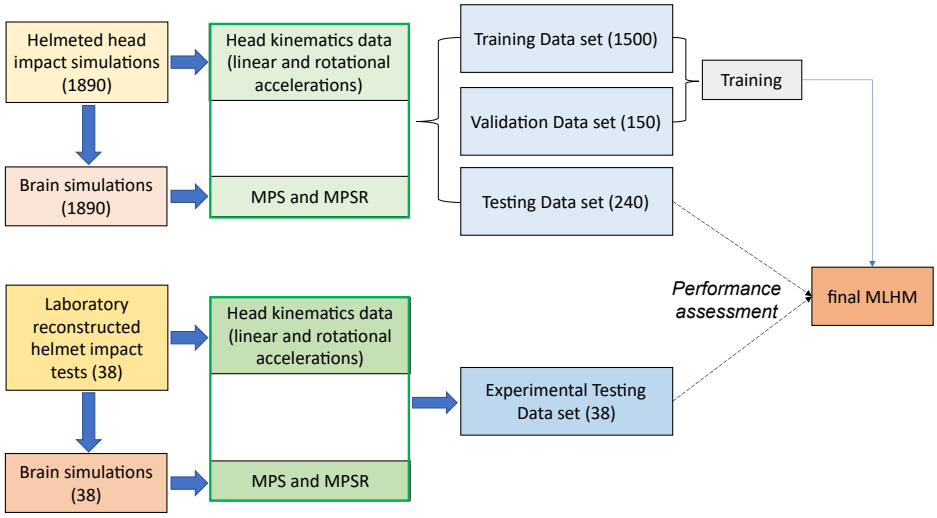

Figure 6.1: Illustration of the model development and the performance assessment phase.

6.1.1 Training data

The first part of the work focused on generating 1) input data (head kinematics) and 2) output data (brain strain and strain rate) needed to train, validate and test the Artificial Neural Networks (ANNs).

1) Head kinematics data used as inputs to train the ANNs were obtained reproducing in a virtual environmental three datasets of 2000, 200 and 300 head impact simulations, used respectively as training, validation and testing datasets. A Hybrid III (HIII) Head Finite Element (FE) model distributed by the Biomechanics and Research, LLC (Biocore) coupled with a AGV X3000 full-face helmet were used to perform the simulations. the detailed information about the helmet FE model can be found in Chapter 3. The impact speed ranged from 8km/h to 78km/h and the simulations were set up to ensure an uniform distribution of the impact point over the entire surface of the helmet. A full description of the three datasets here used can be found in Chapter 4. Finally, the distribution of peak resultant angular acceleration and peak resultant angular velocity of the training dataset is shown in Figure 6.2. The procedure used to generate the simulation datasets (Chapter 4) ensured a wide range for both the angular acceleration and angular velocity

2) The outputs used to train the ANNs were extracted from a high fidelity 3D computational model of brain injury biomechanics [16]. To such end, the three datasets of Head kinematics described in 1) were applied to the skull Centre of Gravity (CoG) of the brain model. A termination time equal to 30ms was selected to fully monitor the brain tissue deformation resulting from the impact. LS-Dyna solver (R10.0, LSTC, US) was used to perform the impact simulations. About 25% of the simulations run using the three datasets ended before the termination time due to numerical errors occurred because of the extremely high deformation value reached by some elements of the brain. As a result, all these simulations were removed: the greatest percentage of them was characterized by a value of the angular acceleration peak greater then $46krad/s^2$. Consequently, training, validation and

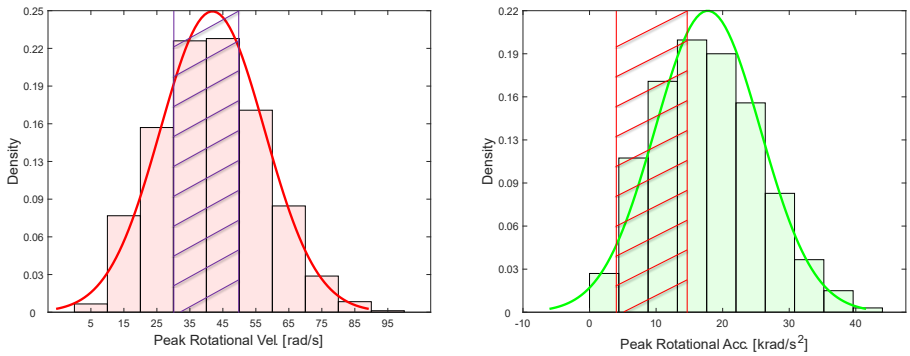

Figure 6.2: Distribution of the kinematics properties across the training dataset. The same properties across the two experimental datasets are enclosed in the hatched areas. (a) peak angular acceleration, (b), peak angular velocity.

testing simulations decreased respectively to 1500, 150 and 240.

The computational model of brain used in this work was validated by Dr. Mazdak Ghajari (detailed information are shown in the supplementary materials section in [130]) in terms of brain displacements through a comparison with open-access data of post-mortem human subjects experiments [131]. Well-controlled rotations were applied to the head, and brain measures were made using receiving crystals inserted into the brain. The model has already been used in different applications such as assessing brain injury prevention effects provided by bicycle helmets [132] and predicting strain and strain rate across the whole brain in 148 American Football head impacts [130].

In 2021 Fahlstedt et al. [133] compared the outputs of the brain model used in this work and other 7 brain models using kinematics data recorded from 17 bicycle helmets subjected to oblique impacts. The study highlighted how different brain models can lead to different results, causing confusion in the biomechanics community, and the study raised the need to find a recognised validation procedure for FE models of the head. Indeed, brain models are nowadays indispensable tools to investigate TBI and currently available models can be used to explore new methodologies to predict TBI in real time. Considering the work discussed in this Chapter, the aim was to prove that a FE model of brain can be replaced by an artificial neural network to perform brain deformation estimations instantaneously. Once the biomechanics community will agree on a standard validation procedure for FE models of the head, the methodology here presented can be used with any validate version of brain model.

The brain model was used to extract the 90th percentile of the maximum value of the 1st principal Green-Lagrange strain (MPS) and strain rate (MPSR) across the whole brain (WB), the whole corpus callosum (CC) and 10 specific tracts. For instance, Figure 6.3 shows the strain and strain rate distribution obtained across the WB for one of the simulations performed. The 10 tracts (Figure 6.4), where cognitive and emotional symptoms are often observed, were selected according to Amy et al. [134]. These tracts are: the body, genu and splenium of the corpus callosum (CCB, CCG, CCS), the corticospinal tract (left and right; CST_L, CST_R), the corona radiata (left and right; CR_L, CR_R), the inferior longitudinal fasciculi

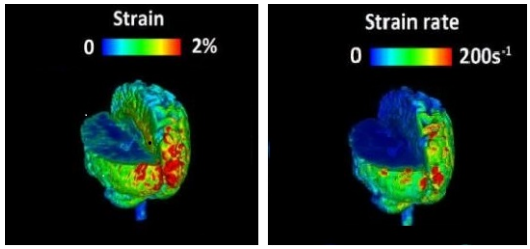

Figure 6.3: Example of strain and strain rate distribution across the WB for one of the performed simulations.

(left and right; ILF_L, ILF_R) and the middle cerebellar peduncle (MCP) [134]. Specifically, the high strain forces sustained by the brain after a TBI can commonly result in damages of the corpus callosum [16], which is associated with cognitive impairment [135, 136]. A damage to the corona radiata is associated with motor and cognitive impairments after TBI [137, 138]. The corticospinal tracts are associated with motor deficits [138, 139], while the inferior longitudinal fasciculi are linked to cognitive and functional loss after TBI [140]. Finally, the middle cerebellar peduncle is associated with cognitive and vestibular/balance symptoms after TBI [141, 142].

6.1.2 Artificial Neural Network architecture

A total of 24 different convolutional neural networks (CNNs) were developed. All of them shared the same architecture: 1) an input layer consisting of a 6x300 matrix. The first 3 rows are the linear acceleration components and the last 3 rows the rotational acceleration components of the head CoG. 300 represents the number of time instant extracted ($dt = 0.0001s$); 2) three convolutional 2D layers of 64 neurons each followed by Rectified Linear unit (ReLU) activation functions; 3) a first Fully Connected (FC) layer of 100 neurons and a subsequent single neuron FC layer; 4) a regression layer as output layer with a single neuron. Parameters of each trained CNN (number and dimension of filters and stride) were optimized to maximize the strain and strain rate estimation performances. The over-fitting was prevented using the dropout operation to each convolutional layer connection.

6.1.3 Impact experiments

Performances of the 24 CNNs were verified using the Testing Dataset (TD) previously described and 38 laboratory reconstructed head impact tests. The experimental tests were broke down into two different groups: the 8 tests performed using the two AGV X3000 helmet models (referred as HIS dataset) and the remaining 30 tests (referred as HIT dataset), performed with 6 different motorcyclists' helmets: HJC C70, Bell Qualifier DLX, Icon Airflite, Bell Qualifier DLX MIPS, Icon Airflite MIPS and Bell Race Star.

Tests performed on the helmets of the HIS dataset were deeply analysed in Chapter 5, and a brief description is given here: tests were performed with an impact speed of 7.75m/s with a standard deviation of 0.0732. For each helmet, 4 different impact scenarios were tested: upper-front (UF), upper-left (UL), back (B) and right (R) shown respectively in Figure 6.5 (a), (b), (c), (d). All tests were performed using a 45° anvil.

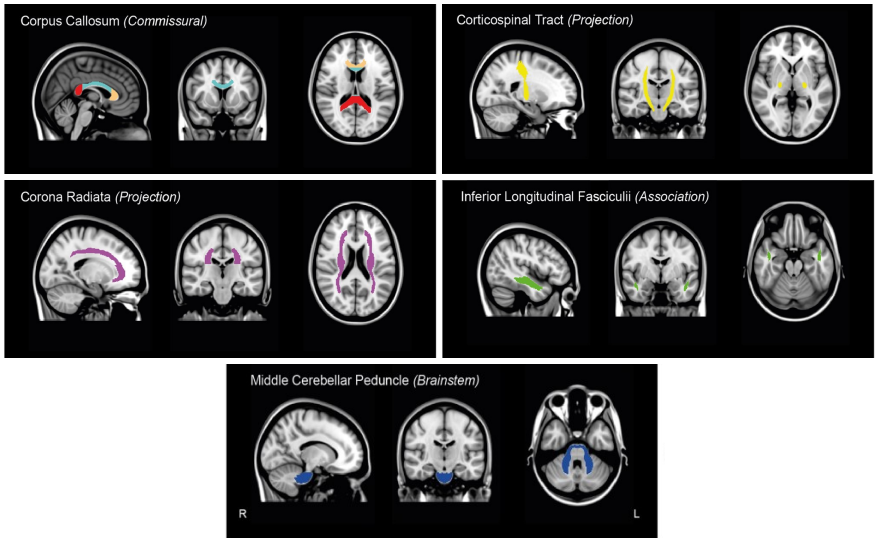

Figure 6.4: Rendering of tracts selected. The corpus callosum shows the three subdivisions as: red = splenium, blue = body, and orange = genu. L = left; R = right. (adopted from [134]).

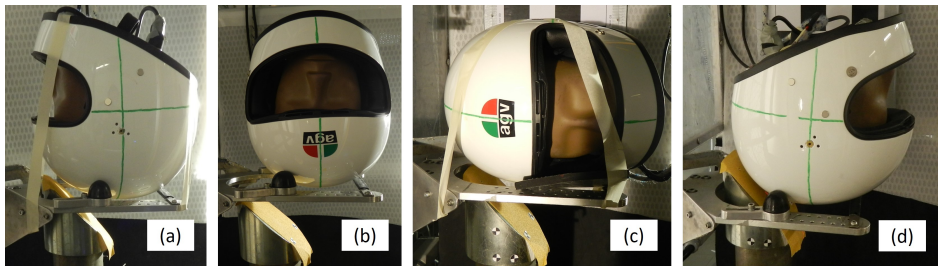

Figure 6.5: Impact test scenarios for the HIS dataset: (a) upper-front (UF), (b) upper-left (UL), (c) right (R) and (d) back (B).

Tests performed on the helmets of the HIT dataset were described in [143], and a brief description is given here: Helmets were tested according to the test method recently introduced in the ECE22.06 [10], except that a Hybrid III 50th percentile male dummy headform was used, which aligned with the impact tests performed on the AGV helmets. The helmeted headform was dropped onto a 45° anvil at a speed of $8.0(+0.15-0.0)m/s$. The 5 impact locations performed on each helmet are shown in Figure 6.6. Specifically, for each model of helmet, 2 samples were used to perform the 5 impact tests required by the standard: impacts 1 to 3 were carried out on helmet sample 1, while impacts 4 and 5 were carried out on helmet sample 2. Head acceleration data were sampled at 50 kHz frequency.

6.1.4 Statistical analysis

Performances were assessed calculating the coefficient of determination R^2 between the estimated MPS or MPSR and their target values for the TD dataset. R^2 was

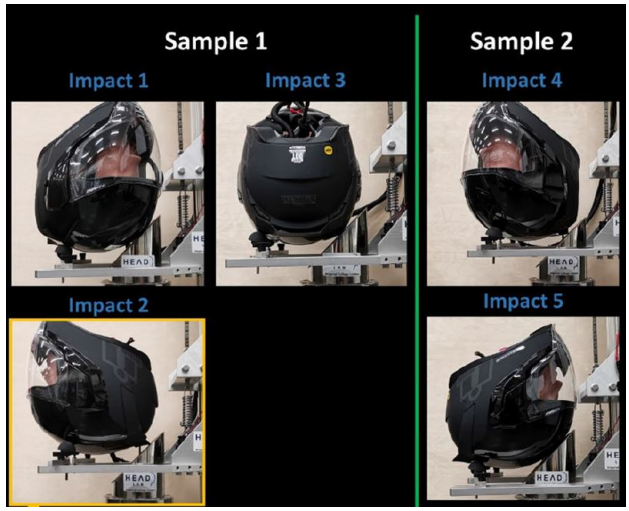

Figure 6.6: Impact test scenarios for the HIT dataset according to the ECE 22.06 standard (adopted from [143]).

Table 6.1: Peak rotational velocity rad/s of the HIS dataset helmets at four impact locations (Figure 5.3, Chapter 5).

Helmets	Impact locations				Mean ± SD
	a	b	c	d	
AGV X3000 - 1	40.3	33.1	51.8	36.8	40.5 ± 8.1
AGV X3000 - 2	41.0	30.3	40.8	38.1	38.1 ± 4.5

used because most of the papers in the state of the art used this metric to evaluate the accuracy of their brain deformation estimator models. Additionally, Root Mean Squared Error (RMSE) for HIS and HIT datasets was assessed.

6.2 Results

The dataset of helmeted head impact simulations used to train the neural networks has been described in terms of kinematic features in Figure 6.2. Peak values of rotational velocity and rotational acceleration ranged respectively from $3rad/s$ to $97rad/s$ and from $2rad/s^2$ to $46rad/s^2$. The same Figure also shows the distribution of these kinematic features for all the 38 experimental impact tests used in this Chapter. Considering these last data, the minimum value assumed by the rotational velocity peak was $26.7rad/s$ and the maximum value $51.8rad/s$. In this range, there was the highest density of data used to train the CNNs. Instead, rotational acceleration peak values varied between $4.7rad/s^2$ and $14.3rad/s^2$; this range was shifted towards the lowest values of rotational accelerations (Figure 6.2 (b)). The detailed kinematics data information of each test belonging to the HIT dataset can be found in [143]. Instead, Tables 6.1 and 6.2 give peak values of rotational velocity and rotational acceleration for the 8 tests of the HIS dataset.

Figure 6.7 shows performances of the trained CNNs in the MPS estimation for the twelve selected Region Of Interest (ROI) of the brain. As shown by each plot,

Table 6.2: Peak rotational acceleration $krad/s^2$ of the HIS dataset helmets at four impact locations (Figure 5.3, Chapter 5).

Helmets	Impact locations				Mean ± SD
	a	b	c	d	
AGV X3000 - 1	8.51	8.88	14.3	11.3	10.7 ± 2.7
AGV X3000 - 2	9.79	7.75	8.85	10.3	9.48 ± 1.2

this dataset took into account the entire range of MPS variability, from 0 to 1. Overall, TD had coefficients of determination R^2 ranging from 0.85 to 0.92. The best performances were obtained in the estimation of MPS for the CCG ROI, with a $R^2 = 0.92$, while MCP area had the worst $R^2 = 0.85$.

For HIT, RMSE ranged from 0.08 to 0.19. WB and CCS regions had the best performances with a RMSE respectively of 0.08 and 0.09, while ILF_R had the worst prediction with a RMSE of 0.19.

For HIS, RMSE ranged between 0.08 and 0.18. Also for this dataset, WB and CCS had the best performances with the same $RMSE = 0.08$, while CST_L had the worst prediction with a RMSE of 0.18.

Excluding the CST_R area, the two experimental datasets had similar performances, as certified by the similar ranges of RMSE. For both HIT and HIS datasets, the 10 tracts showed more underestimated predicted strains that overestimated ones; this was attested by the majority of predictions that lied below the symmetry axis.

Figure 6.8 compares the predicted MPSR with the directly simulated values for each brain ROI. For TD, the WB area had the best performances with a $R^2 = 0.89$. R^2 coefficients for the remaining regions ranged from 0.77 to 0.87.

For HIT, CCB had the best performances with a $RMSE = 0.06$. CC, CCG, ILF_R and MCP had RMSE values smaller then 0.10, while the other ROI had worst performances, with CR_L that showed the worst prediction with a $RMSE = 0.27$.

For HIS, the best performances were reached in the CCG area, with a $RMSE = 0.07$, while CST_R had the worst $RMSE = 0.28$. The other ROI can be divided into 2 groups: WB, CC, CCB, INF_R and MCP that showed a good accuracy in the MPSR estimation with RMSE ranging between 0.09 and 0.11, while prediction of MPSR in CCS, CST_L, CR_L, CR_R and INF_L areas generated worst results, with RMSE values varying between 0.18 and 0.27.

All ROI showed a difference of less than 7% in the estimation of the MSPR between HIT and HIS.

Predicted strain rates were affected by an overestimation in all the considered ROI, except for CCB, CCG and INF_L tracts. Data were also affected by a greater dispersion for high values of strain-rate; this behaviour was marked especially in CST, CR and ILF regions.

6.3 Discussion

Despite TBIs are far from being fully understood, magnitude and distribution of maximum principal brain strain (MPS) and strain rate (MPSR) have been identified as good predictors of TBIs and computational modelling became the tool to investigate head injuries. However, complexity of computational software and the

huge amount of computational time needed hampered the spread of finite element modelling (FEM) for TBI risk assessment in real-world applications. This study aimed to address these 2 limitations of FEM introducing a data-driven approach, based on CNNs, to predict MPS and MPSR of twelve brain ROI in road impacts involving motorcyclists. Indeed, among all road users, TBI is the most frequent cause of serious and fatal road crashes for motorcyclists. Therefore, a technology able to predict TBI in real time would be extremely beneficial for them.

Results showed that a complex finite element model of human brain can be replaces by ANNs to compute MPS and MPSR from the head kinematics. Indeed, when the CNNs were applied to the dataset of simulations (i.e, TD), satisfactory performances were obtained with R^2 coefficients ranging from 0.85 to 0.92 and from 0.77 to 0.89 respectively in the MPS and MPSR prediction for the different brain areas considered. High correlation between the outputs of a FE brain model and real time estimation of the brain response through CNNs were proved also by Shaoju Wu et al. [62], Zhan et al.[65] and Bourdet et al. [66]. These recent studies deepened the correlation between computed and predicted MPS and MPSR into the whole brain and corpus callosum ([62] and [65]) or between computed and predicted Maximum Von Mises stress [66]. This work considered 10 specific brain tracts, focusing not only on global brain deformation estimation, but also on localised areas, ensuring a better understanding of the injury outcome.

Results proved that a model, based on CNNs, to predict brain MPS and MPSR using head kinematics data, can be successfully trained using an entirely numerical dataset and then used with experimental inputs. Indeed, the CNNs described in this thesis were trained using only numerical inputs and outputs. When the CNNs were applied to the experimental datasets, results showed RMSE values ranging from 0.08 and 0.19 for the MPS estimation and from 0.06 and 0.28 for the MPSR estimation. Instead, the most recent studies mentioned in the previous paragraph used a combination between numerical and experimental data as inputs to train the CNNs. As most of the inputs used by these recent studies come from experimental helmet testing, the range of head kinematics used as inputs to train the CNNs is limited. This is due to the fact that existing laboratory test methods have used speeds which are lower than the ones experienced in real collisions. Indeed, propulsion method of existing laboratory rigs, i.e. using gravity to accelerate helmet in a free fall drop, are unable to propel helmets at high speeds.

Numerical simulations employed to generate the input data (i.e. head acceleration components) used in the training phase of the CNNs shared the same specific FE model of helmet, i.e. the helmet model AGV X3000. The results highlighted that CNNs trained in this way can still be used with input data from any typology of motorcycle helmet or helmets with rotational technologies (MIPS or FLEX) fitted into them. As shown by the results, the two experimental datasets considered in the validation process had similar performances, as certified by the similar values of RMSE obtained in each ROI considered (Figures 6.7 and 6.8). Excluding CST_R area, performances of HIT and HIS in the MPS and MPSR estimation differed less then 3% and 5% respectively between each others. However, the first dataset (HIS) consisted of head kinematics data from AGV X3000 helmet testing, i.e the same FE model exploited in the simulations used to train the CNNs. The second dataset (HIT) included 6 motorcycle helmets of different brands (HJC, Bell and Icon), and three of them were equipped with a technology (MIPS or FLEX) aimed to reduce head rotation during the impact.

When experimental inputs were given to CNNs, performances showed discrepancies in predicting MPS and MPSR for general areas rather than for specific tracts. The more general regions (i.e, WB and CC) have shown the best performances with a RMSE varying from 0.08 and 0.11 in the MPS prediction and from 0.09 and 0.12 in the MPSR prediction. Instead, estimation of MPS and MPSR in the specific tracts produced greater values of the RMSE. This difference may be explained with the higher precision required by the model to estimate strain and strain rate in restricted brain areas rather then the whole brain. When the whole brain is considered, even if the simulated brain deformation is not precise for every single element of the brain, a very accurate estimation of maximum values of strain and strain rate can still be obtained. When a localised area is considered, precision has a bigger influence on the performances rather than the whole brain. In addition, for both the experimental datasets, the 10 tracts showed more underestimated than overestimated predicted MPS. On the other hand, predicted MPSR were affected by an overestimation rather than an underestimation in all the considered areas, except for CCB, CCG and INF_L tracts. A future exploitation of this method in a real-time system implemented into a helmet should include a proper correction to adjust these errors.

A limitation of this study is related to the reduced number of simulations (1500) used to train the CNNs compared to the wide range of head kinematics considered as inputs for the neural networks (up to $45krad/s$). Large quantity of data is generally necessary to produce acceptable results from a trained CNN. Wu et al. [62] used 2592 samples to train a neural network able to achieve good performances in brain MPS prediction, while Zhan et al. [65] obtained acceptable results using more then 10000 simulations. In addition, head rotational acceleration peak of data used to train ANNs in these two studies was less than $20krad/s$, while this work considered data with rotational acceleration peak values up to $45krad/s$. Using such a range of rotational head accelerations led to extremely high values of MPS and MPSR in the simulations used to built the output dataset. This suggested to consider a reduced range of head kinematics as input data. Indeed, such high values of brain deformation lead to almost certain death, therefore are biologically not relevant. Performances achieved in this work are sightly weaker than performances showed by other studies. However, similar or better results can be achieved reducing the head kinematics range and keeping the same amount of simulations used to train the CNNs (1500).

A further limitation is the absence of a 10-fold cross-correlation to validate the model. This statistical method is commonly used when the performances of the model are significantly affected by the partitioning chosen between training, validation and testing datasets. As the different numerical training, validation and testing datasets were built in the same way (Chapter 4), no significative changes were observed in the present work.

Another limitation of the proposed model is linked to the limitation of the brain FE model used. Worldwide, several ongoing research projects relate to this topic, showing that the brain model exploited in this study is a simplified model that can be replaced by more advanced brain models in the future.

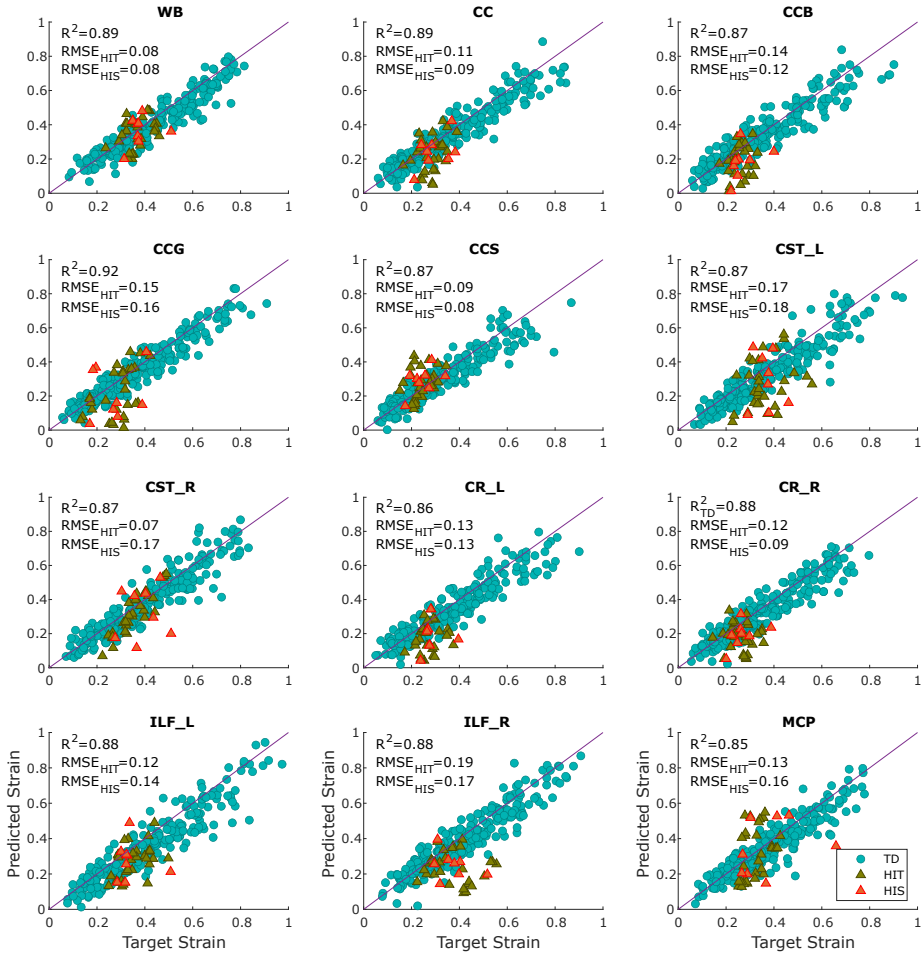

Figure 6.7: Performances of the 12 CNNs trained and optimized to predict strain in different Region Of Interest of the brain using three different datasets: (TD) testing dataset, (HIS-HIT) laboratory reconstructed helmeted head impact tests performed respectively using the AGV X3000 helmet model and other 6 motorcycle helmet types. Each selected plot shows performance in terms of R^2 for TD and RMSE for HIS and HIT. From first to last: (a) WB: whole brain, (b) CC: corpus callosum, (c-d-e) CCB-CCG-CCS: respectively body, genu and splenium of corpus callosum, (f-g) CST_L-CST_R: left and right corticospinal, (h-i) CR_L-CR_R: left and right corona radiata , (l-m) ILF_L-ILF_R: left and right inferior longitudinal fasciculi, (n) MCP: middle cerebellar peduncle.

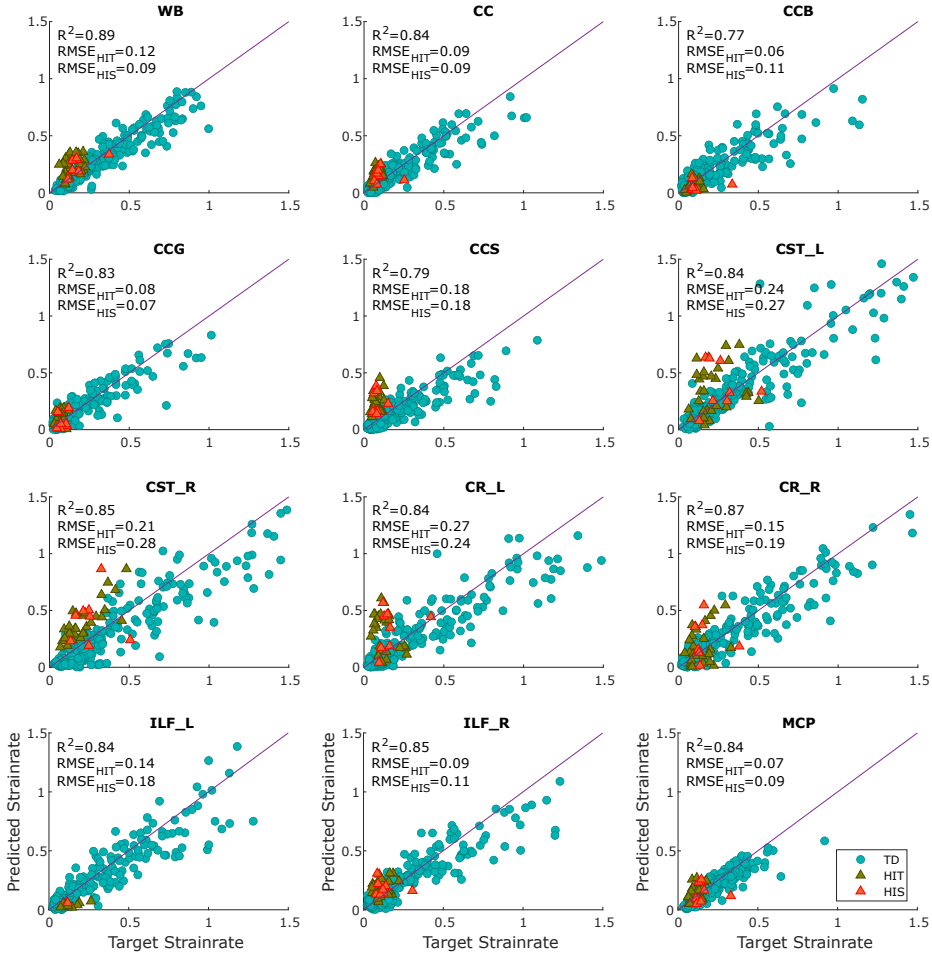

Figure 6.8: Performances of the 12 CNNs trained and optimized to predict strainrate in different Region Of Interest of the brain using three different datasets: (TD) testing dataset, (HIS-HIT) laboratory reconstructed helmeted head impact tests performed respectively using the AGV X3000 helmet model and other 6 motorcycle helmet types. Each selected plot shows performance in terms of R^2 for TD and RMSE for HIS and HIT. From first to last: (a) WB: whole brain, (b) CC: corpus callosum, (c-d-e) CCB-CCG-CCS: respectively body, genu and splenium of corpus callosum, (f-g) CST_L-CST_R: left and right corticospinal, (h-i) CR_L-CR_R: left and right corona radiata , (l-m) ILF_L-ILF_R: left and right inferior longitudinal fasciculi, (n) MCP: middle cerebellar peduncle.

Chapter 7

Conclusion and Outlook

This research described the steps followed in the to develop a methodology for a real time estimation of motorcyclists' traumatic brain injuries in crashes. This included a first trial to identify the helmet CoG accelerations, a methodology to assess the head CoG kinematics and a method to estimate the brain deformations during an impact sustained by the head. These topics were faced sequentially, but they are linked and necessary to implement the methodology discussed in this thesis.

Initially, from an in-depth analysis of devices developed over the years for similar purposes, the 6DOF device was selected and modified: the accelerometers, originally embedded in a padding to guarantee the contact with the head, were rigidly attached to the inner surface of the helmet shell. The algorithm used by the 6DOF device, applied to data acquired by the accelerometers in the new locations, provided the accelerations of the helmet CoG. However, the helmet deformability affected the performances of the modified 6DOF, leading to poor performances in the helmet CoG accelerations. Since the algorithms of the main devices deployed over the years were implemented considering the application to a rigid body, this first step confirmed that such devices can not be adapted to assess the helmet accelerations. In fact, the deformability of the helmet strongly affected performances.

According to the results, the development of a method to assess the helmet CoG accelerations was abandoned and the direct estimation of the head kinematics was investigated. A new technology consisting of single-axis accelerometers attached to the inner surface of a helmet shell and ANNs, to estimate the head linear and rotational head accelerations was implemented. An optimization study identified five as the minimum number of single-axis accelerometers to obtain acceptable performances in the head acceleration estimation with this technology. ANNs were trained using numerical data, significantly reducing the cost of development. The representativeness of the FE model of helmet used to extract numerical data was verified through experimental tests. In addition, experimental results showed that the algorithm is effective. The main challenges for this methodology are 1) the development of a FE set up able to accurately reproduce the signals acquired by the accelerometers embedded into the helmet and the headform kinematics; 2) selecting the adequate number of simulations and their head kinematics range to maximise ANN prediction performances.

Finally, a new methodology, based on CNNs, to estimate strain and strain rate in 12 ROI of the brain was developed. Strain and strain rate were selected since they are good predictors of TBIs. CNNs were trained with numerical data extracted

from a high fidelity 3D computational model of brain injury biomechanics. CNNs showed a good accuracy in the strain and strain rate prediction for all the tracts considered when they were applied to numerical data. Then, trained CNNs were also applied to experimental data: the more general ROI (WB and CC) showed comparable performances with the numerical data, while the specific tracts had a worst prediction. However, results were promising and confirmed that ANNs trained with numerical data can be also used with experimental data. In addition, the typology of motorcycle helmet or any technology to reduce the head rotation fitted in it did not affect the prediction performances. This means that once trained, CNNs can be exploited with every motorcycle helmet.

Thus, this thesis investigated a novel concept of methodology based on an artificial intelligence module consisting of a kinematics sub-module and the injury sub-module. The former returns as output the linear and rotational components of the head acceleration using the signals acquired by 5 single-axis accelerometers attached to the helmet outer shell. The head kinematics components are the inputs to the injury sub-module, which gives in output the TBI risk in terms of strain and strain rate in 12 brain ROI.

This work investigated the methodology in terms of feasibility rather than accuracy, as the accuracy is strongly dependent on the FE models used to generate the training data needed to implement the artificial intelligence module. In this context, future developments will imply the improvement of the helmet and brain FE model. This work suggested that the modelling of the helmet should take into consideration the propagation and reflection of longitudinal and transversal waves generated by the impact. A standard validation procure aimed to improve reliability of brain models should be suggested by the biomechanics community.

The results obtained could open up new possibilities to ensure greater safety not only for motorcyclists, but also for all other road users wearing a helmet such as cyclists. The technology investigated in this thesis is highly customisable and the installation of accelerometers and AI module on the helmet outer shell can be integrated in the production phase of this component. This technology can turn even the most classic helmet into a smart helmet. Big data collected by this technology over the years could ensure a continuous improvement in the estimation of TBI and thus in user safety.

Bibliography

[1] A. Murphy *et al.*, 'Reported road casualties great britain: 2019 annual report', *The Department for Transport: London, UK*, 2020.

[2] N. Administration., 'Traffic safety facts, 2019: Motorcycles', *The Department for Transport: London, UK*, 2021.

[3] B. Chinn *et al.*, 'Cost 327 motorcycle safety helmets', *European Commission, Directorate General for Energy and Transport*, 2001.

[4] J. Mcleod, J. Di Giacomo, J. Christopher and G. Tinkoff, 'Helmet efficacy to reduce head injury and mortality in motorcycle crashes', *J Trauma*, vol. 69, no. 5, pp. 1101–1111, 2010.

[5] H. Lissner, M. Lebow and F. Evans, 'Experimental studies on the relation between acceleration and intracranial pressure changes in man', *Surgery, gynecology & obstetrics*, vol. 111, pp. 329–338, 1960.

[6] S. Kleiven, 'Why most traumatic brain injuries are not caused by linear acceleration but skull fractures are', *Frontiers in bioengineering and biotechnology*, vol. 1, p. 15, 2013.

[7] S. Kleiven, 'Evaluation of head injury criteria using a finite element model validated against experiments on localized brain motion, intracerebral acceleration, and intracranial pressure', *International Journal of Crashworthiness*, vol. 11, no. 1, pp. 65–79, 2006, ISSN: 13588265. DOI: 10.1533/ijcr.2005.0384.

[8] B. Depreitere *et al.*, 'Mechanics of acute subdural hematomas resulting from bridging vein rupture', *Journal of neurosurgery*, vol. 104, no. 6, pp. 950–956, 2006.

[9] 'Uniform provisions concerning the approval of protective helmets and their visors for drivers and passengers of motor cycles and mopeds', United Nations, Standard, 2002.

[10] 'Uniform provisions concerning the approval of protective helmets and their visors for drivers and passengers of motor cycles and mopeds', United Nations, Standard, 2021.

[11] *A new level of rider protection. available from: Https://www.bellhelmets.com/technology/flex.html.* 2021.

[12] P. Halldin, M. Aare, S. Kleiven and H. von Holst, 'Improved helmet design and test methods to reduce rotational induced brain injuries', in *RTO Specialist Meeting, the NATO's Research and Technology Organization (RTO)*, 2003.

[13] J. J. Tepas III *et al.*, 'The effect of delay in rehabilitation on outcome of severe traumatic brain injury', *Journal of pediatric surgery*, vol. 44, no. 2, pp. 368–372, 2009.

[14] J. J. Chu, 'An algorithm for estimating acceleration magnitude and impact location using multiple nonorthogonal single-axis accelerometers', *Journal of Biomechanical Engineering*, vol. 126, no. 6, p. 849, 2005, ISSN: 0148-0731. DOI: 10.1115/1.1824135.

[15] S. Rowson, J. G. Beckwith, J. J. Chu, D. S. Leonard, R. M. Greenwald and S. M. Duma, 'A six degree of freedom head acceleration measurement device for use in football.', *Journal of applied biomechanics*, vol. 27, no. 1, pp. 8–14, 2011, ISSN: 1065-8483.

[16] M. Ghajari, P. J. Hellyer and D. J. Sharp, 'Computational modelling of traumatic brain injury predicts the location of chronic traumatic encephalopathy pathology', *Brain*, vol. 140, no. 2, pp. 333–343, 2017.

[17] D. K. Menon, K. Schwab, D. W. Wright, A. I. Maas *et al.*, 'Position statement: Definition of traumatic brain injury', *Archives of physical medicine and rehabilitation*, vol. 91, no. 11, pp. 1637–1640, 2010.

[18] A. I. King, 'Fundamentals of impact biomechanics: Part i-biomechanics of the head, neck, and thorax', *Annual review of biomedical engineering*, vol. 2, no. 1, pp. 55–81, 2000.

[19] A. Baethmann, J. Eriskat, M. Stoffel, D. Chapuis, A. Wirth and N. Plesnila, 'Special aspects of severe head injury: Recent developments', *Current Opinion in Anesthesiology*, vol. 11, no. 2, pp. 193–200, 1998.

[20] L. F. Marshall, 'Head injury: Recent past, present, and future', *Neurosurgery*, vol. 47, no. 3, pp. 546–561, 2000.

[21] T. K. Mclntosh, D. H. Smith, D. F. Meaney and M. J. Kotapka, 'Neuropathological sequelae of traumatic brain lnjury: Relationship to neurochemical and biomechanical', *Laboratory investigation*, vol. 74, no. 2, p. 315, 1996.

[22] J. Nortje and D. K. Menon, 'Traumatic brain injury: Physiology, mechanisms, and outcome', *Current opinion in neurology*, vol. 17, no. 6, pp. 711–718, 2004.

[23] A. H. Ropper and K. C. Gorson, 'Concussion', *New England Journal of Medicine*, vol. 356, no. 2, pp. 166–172, 2007.

[24] J. H. Adams, D. Graham, L. S. Murray and G. Scott, 'Diffuse axonal injury due to nonmissile head injury in humans: An analysis of 45 cases', *Annals of Neurology: Official Journal of the American Neurological Association and the Child Neurology Society*, vol. 12, no. 6, pp. 557–563, 1982.

[25] J. H. Adams, D. Doyle, I. Ford, T. Gennarelli, D. Graham and D. McLellan, 'Diffuse axonal injury in head injury: Definition, diagnosis and grading', *Histopathology*, vol. 15, no. 1, pp. 49–59, 1989.

[26] T. A. Gennarelli, 'Mechanisms of brain injury.', *The Journal of emergency medicine*, vol. 11, pp. 5–11, 1993.

[27] T. Rust, N. Kiemer and A. Erasmus, 'Chronic subdural haematomas and anticoagulation or anti-thrombotic therapy', *Journal of clinical neuroscience*, vol. 13, no. 8, pp. 823–827, 2006.

[28] W. Keller *et al.*, 'Rating the severity of tissue damage: I. the abbreviated injury scale', *JAMA*, vol. 215, no. 2, pp. 277–280, 1971.

[29] E. Petrucelli, J. D. States and L. N. Hames, 'The abbreviated injury scale: Evolution, usage and future adaptability', *Accident Analysis & Prevention*, vol. 13, no. 1, pp. 29–35, 1981, ISSN: 0001-4575. DOI: https://doi.org/10.1016/0001-4575(81)90040-3.

[30] K. Miller and K. Chinzei, 'Constitutive modelling of brain tissue: Experiment and theory', *Journal of biomechanics*, vol. 30, no. 11-12, pp. 1115–1121, 1997.

[31] M. T. Prange, D. F. Meaney, S. S. Margulies *et al.*, 'Defining brain mechanical properties: Effects of region, direction, and species', *Stapp Car Crash J*, vol. 44, no. 205-213, 2000.

[32] E. G. Takhounts, J. R. Crandall and K. Darvish, 'On the importance of nonlinearity of brain tissue under large deformations', *Stapp car crash journal*, vol. 47, p. 79, 2003.

[33] S. Strich, 'Shearing of nerve fibres as a cause of brain damage due to head injury: A pathological study of twenty cases', *The Lancet*, vol. 278, no. 7200, pp. 443–448, 1961.

[34] C. W. Gadd, 'Use of a weighted-impulse criterion for estimating injury hazard', SAE technical paper, Tech. Rep., 1966.

[35] L. M. Patrick, H. R. Lissner and E. S. Gurdjian, 'Survival by design: Head protection', in *Proceedings: American Association for Automotive Medicine Annual Conference*, Association for the Advancement of Automotive Medicine, vol. 7, 1963, pp. 483–499.

[36] J. Versace, *A review of the severity index*, 1971.

[37] EuroNCAP, 'European New Car Assessment Programme (Euro NCAP) Assessment Protocol Adult occupant protection', no. November, 2017.

[38] EuroNCAP, 'European New Car Assessment Programme (Euro NCAP) pedestrian testing protocol', no. November, 2017.

[39] T. A. Gennarelli, L. E. Thibault and A. K. Ommaya, 'Pathophysiologic responses to rotational and translational accelerations of the head', *SAE Technical Papers*, pp. 296–308, 1972, ISSN: 26883627. DOI: 10.4271/720970.

[40] Thomas, A. and Gennarelli, M.D. and Lawrence, E. and Thibault, Sc. D., 'Biomechanics of acute subdural hematoma', *The Journal of Trauma, 680–686*,

[41] J. Melvin, 'Review of biomechanical impact response and injury in the automotive environment', *Transportation Research Circular*, 1991.

[42] J. A. Newman, 'A Generalized Model for Brain Injury Threshold', *In Proceedings of International Conference on the Biomechanics of Impact, 1986 (pp. 121-131).*, pp. 121–131, 1986.

[43] J. A. Newman, N. Shewchenko and E. Welbourne, 'A Proposed New Biomechanical Head Injury Assessment Function -The Maximum Power Index', *Reprinted From: Stapp Car Crash Journal*, vol. 44, no. 724, 2000, ISSN: 0148-7191.

[44] H. Kimpara and M. Iwamoto, 'Mild traumatic brain injury predictors based on angular accelerations during impacts', *Annals of biomedical engineering*, vol. 40, no. 1, pp. 114–126, 2012.

[45] E. Takhounts, M. Craig, K. Moorhouse, J. McFadden and V. Hasija, 'Development of brain injury criteria (bric).', *Stapp car crash journal*, vol. 57, 2013.

[46] E. G. Takhounts, V. Hasija, S. A. Ridella, S. Rowson and S. M. Duma, 'Kinematic rotational brain injury criterion (bric)', in *Proceedings of the 22nd enhanced safety of vehicles conference. Paper*, Citeseer, 2011, pp. 1–10.

[47] T. Yanaoka, Y. Dokko and Y. Takahashi, 'Investigation on an injury criterion related to traumatic brain injury primarily induced by head rotation', SAE Technical Paper, Tech. Rep., 2015.

[48] L. F. Gabler, J. R. Crandall and M. B. Panzer, 'Development of a metric for predicting brain strain responses using head kinematics', *Annals of biomedical engineering*, vol. 46, no. 7, pp. 972–985, 2018.

[49] L. F. Gabler, J. R. Crandall and M. B. Panzer, 'Development of a second-order system for rapid estimation of maximum brain strain', *Annals of biomedical engineering*, vol. 47, no. 9, pp. 1971–1981, 2019.

[50] M.-C. Lee and R. C. Haut, 'Insensitivity of tensile failure properties of human bridging veins to strain rate: Implications in biomechanics of subdural hematoma', *Journal of biomechanics*, vol. 22, no. 6-7, pp. 537–542, 1989.

[51] D. C. Viano and P. Lovsund, 'Biomechanics of brain and spinal-cord injury: Analysis of neuropathologic and neurophysiology experiments', *Traffic Injury Prevention*, vol. 1, no. 1, pp. 35–43, 1999.

[52] T. J. Horgan, 'A finite element model of the human head for use in the study of pedestrian accidents', Ph.D. dissertation, University College Dublin Ireland, 2005.

[53] C. Ward, M. Chan and A. Nahum, 'Intracranial pressure—a brain injury criterion', *SAE Transactions*, pp. 3867–3880, 1980.

[54] S. Kleiven, 'Predictors for traumatic brain injuries evaluated through accident reconstructions', *Stapp car crash J*, vol. 51, no. 81, pp. 81–114, 2007.

[55] A. C. Bain and D. F. Meaney, 'Tissue-level thresholds for axonal damage in an experimental model of central nervous system white matter injury', *Journal of biomechanical engineering*, vol. 122, no. 6, pp. 615–622, 2000.

[56] L. Zhang, K. H. Yang, A. I. King and D. C. Viano, 'A new biomechanical predictor for mild traumatic brain injury–a preliminary finding', in *Proc. 2003 Summer Bioengineering Conference*, 2003, pp. 137–138.

[57] M. Hajiaghamemar, M. Seidi and S. S. Margulies, 'Head rotational kinematics, tissue deformations, and their relationships to the acute traumatic axonal injury', *Journal of biomechanical engineering*, vol. 142, no. 3, p. 031 006, 2020.

[58] C. K. Donat *et al.*, 'From biomechanics to pathology: Predicting axonal injury from patterns of strain after traumatic brain injury', *Brain*, vol. 144, no. 1, pp. 70–91, 2021.

[59] H. Mao *et al.*, 'Development of a finite element human head model partially validated with thirty five experimental cases', *Journal of biomechanical engineering*, vol. 135, no. 11, p. 111 002, 2013.

[60] H.-S. Kang, R. Willinger, B. M. Diaw and B. Chinn, 'Validation of a 3d anatomic human head model and replication of head impact in motorcycle accident by finite element modeling', *SAE transactions*, pp. 3849–3858, 1997.

[61] L. Liang, M. Liu, C. Martin and W. Sun, 'A deep learning approach to estimate stress distribution: A fast and accurate surrogate of finite-element analysis', *Journal of The Royal Society Interface*, vol. 15, no. 138, p. 20 170 844, 2018.

[62] S. Wu, W. Zhao, K. Ghazi and S. Ji, 'Convolutional neural network for efficient estimation of regional brain strains', *Scientific reports*, vol. 9, no. 1, pp. 1–11, 2019.

[63] W. Zhao and S. Ji, 'White matter anisotropy for impact simulation and response sampling in traumatic brain injury', *Journal of neurotrauma*, vol. 36, no. 2, pp. 250–263, 2019.

[64] B. Efron, 'The estimation of prediction error: Covariance penalties and cross-validation', *Journal of the American Statistical Association*, vol. 99, no. 467, pp. 619–632, 2004.

[65] X. Zhan *et al.*, 'Rapidly and accurately estimating brain strain and strain rate across head impact types with transfer learning and data fusion', *arXiv preprint arXiv:2108.13577*, 2021.

[66] N. Bourdet, C. Deck, A. Trog, F. Meyer, V. Noblet and R. Willinger, 'Deep learning methods applied to the assessment of brain injury risk', in *International Research Council on Biomechanics of Injury (IRCOBI) 2021, 6-10 septembre 2021, en ligne*, 2021.

[67] D. S.M. *et al.*, 'Analysis of real-time head accelerations in collegiate football players', *Clinical Journal of Sport Medicine*, vol. 15, no. 1, pp. 3–8, 2005.

[68] J. R. Funk, S. Duma, S. Manoogian and S. Rowson, 'Biomechanical risk estimates for mild traumatic brain injury', vol. 51, p. 343, 2007.

[69] R. M. Greenwald, T. G. Joseph, J. J. Chu and J. J. Crisco, 'Head impact severity measures for evaluating brain injury risk exposure', vol. 62, no. 4, pp. 789–798, 2008. DOI: 10.1227/01.NEU.0000311244.05104.96.

[70] J. J. Crisco *et al.*, 'Head impact exposure in collegiate football players', *Journal of Biomechanics*, vol. 44, no. 15, pp. 2673–2678, 2011, ISSN: 00219290. DOI: 10.1016/j.jbiomech.2011.08.003.

[71] J. G. Beckwith, R. M. Greenwald and J. J. Chu, 'Measuring head kinematics in football: Correlation between the head impact telemetry system and hybrid iii headform', *Annals of Biomedical Engineering*, vol. 40, no. 1, pp. 237–248, 2012, ISSN: 00906964. DOI: 10.1007/s10439-011-0422-2.

[72] S. Rowson *et al.*, 'Rotational head kinematics in football impacts: An injury risk function for concussion', *Annals of Biomedical Engineering*, vol. 40, 2012. DOI: 10.1007/s10439-011-0392-4.

[73] R. Jadischke, D. C. Viano, N. Dau, A. I. King and J. McCarthy, 'On the accuracy of the head impact telemetry (hit) system used in football helmets', *Journal of Biomechanics*, vol. 46, no. 13, pp. 2310–2315, 2013. DOI: 10.1016/j.jbiomech.2013.05.030.

[74] M. A. Allison, Y. S. Kang, J. H. Bolte, M. R. Maltese, K. B. Arbogast *et al.*, 'Validation of a helmet-based system to measure head impact biomechanics in ice hockey.', *Medicine and science in sports and exercise*, vol. 46, no. 1, pp. 115–123, 2014.

[75] L. L. Brainard *et al.*, 'Gender differences in head impacts sustained by collegiate ice hockey players', *Medicine and science in sports and exercise*, vol. 44, no. 2, p. 297, 2012.

[76] J. G. Beckwith, J. J. Chu and R. M. Greenwald, 'Validation of a noninvasive system for measuring head acceleration for use during boxing competition', *Journal of Applied Biomechanics*, vol. 23, no. 3, pp. 238–244, 2007, ISSN: 15432688. DOI: 10.1123/jab.23.3.238.

[77] E. Hanlon and C. Bir, 'Validation of a wireless head acceleration measurement system for use in soccer play', *Journal of applied biomechanics*, vol. 26, no. 4, pp. 424–431, 2010.

[78] H. Kimpara, Y. Nakahira and M. Iwamoto, 'Head injury prediction methods based on 6 degree of freedom head acceleration measurements during impact', *International Journal of Automotive Engineering*, vol. 2, no. 2, pp. 13–19, 2011, ISSN: 2185-0992. DOI: 10.20485/jsaeijae.2.2_13.

[79] M. A. Allison, Y. S. Kang, M. R. Maltese, J. H. Bolte and K. B. Arbogast, 'Measurement of hybrid iii head impact kinematics using an accelerometer and gyroscope system in ice hockey helmets', *Annals of Biomedical Engineering*, vol. 43, no. 8, pp. 1896–1906, 2015, ISSN: 15739686. DOI: 10.1007/s10439-014-1197-z.

[80] L. C. Wu *et al.*, 'In vivo evaluation of wearable head impact sensors', *Annals of biomedical engineering*, vol. 44, no. 4, pp. 1234–1245, 2016.

[81] M. Higgins, P. D. Halstead, L. Snyder-Mackler and D. Barlow, 'Measurement of impact acceleration: Mouthpiece accelerometer versus helmet accelerometer', *Journal of athletic training*, vol. 42, no. 1, p. 5, 2007.

[82] S. Manoogian, D. McNeely, S. Duma, G. Brolinson and R. Greenwald, 'Head acceleration is less than 10 percent of helmet acceleration in football impacts.', *Biomedical sciences instrumentation*, vol. 42, pp. 383–388, 2006.

[83] H. Joodaki, A. Bailey, D. Lessley, J. Funk, C. Sherwood and J. Crandall, 'Relative motion between the helmet and the head in football impact test', *Journal of biomechanical engineering*, vol. 141, no. 8, 2019.

[84] L. E. Miller, C. Kuo, L. C. Wu, J. E. Urban, D. B. Camarillo and J. D. Stitzel, 'Validation of a custom instrumented retainer form factor for measuring linear and angular head impact kinematics', *Journal of biomechanical engineering*, vol. 140, no. 5, 2018.

[85] D. King, P. A. Hume, M. Brughelli and C. Gissane, 'Instrumented mouthguard acceleration analyses for head impacts in amateur rugby union players over a season of matches', *The American journal of sports medicine*, vol. 43, no. 3, pp. 614–624, 2015.

[86] F. Hernandez, P. B. Shull and D. B. Camarillo, 'Evaluation of a laboratory model of human head impact biomechanics', *Journal of biomechanics*, vol. 48, no. 12, pp. 3469–3477, 2015.

[87] F. Hernandez *et al.*, 'Six degree-of-freedom measurements of human mild traumatic brain injury', *Annals of biomedical engineering*, vol. 43, no. 8, pp. 1918–1934, 2015.

[88] L. F. Gabler *et al.*, 'On-field performance of an instrumented mouthguard for detecting head impacts in american football', *Annals of biomedical engineering*, vol. 48, no. 11, pp. 2599–2612, 2020.

[89] T. Knox, 'Use of instrumented earplugs to measure driver head accelerations', SAE Technical Paper, Tech. Rep., 2002.

[90] R. T. Tierney *et al.*, 'Sex differences in head acceleration during heading while wearing soccer headgear', *Journal of athletic training*, vol. 43, no. 6, pp. 578–584, 2008.

[91] E. D. Bekiaris, A. Spadoni and S. I. Nikolaou, 'Saferider project: New safety and comfort in powered two wheelers', in *2009 2nd Conference on Human System Interactions*, IEEE, 2009, pp. 600–602.

[92] A. Delhaye and L. Marot, 'A european scanning tour for motorcycling safety, final report of the ec/move/c4 project riderscan', 2015.

[93] D. A. Greenhill, P. Navo, H. Zhao, J. Torg, R. D. Comstock and B. P. Boden, 'Inadequate helmet fit increases concussion severity in american high school football players', *Sports Health*, vol. 8, no. 3, pp. 238–243, 2016.

[94] R. Jadischke, *Football helmet fitment and its effects on helmet performance*. Wayne State University, 2012.

[95] T. Uhl, 'The inverse identification problem and its technical application', *Archive of Applied Mechanics*, vol. 77, no. 5, pp. 325–337, 2007.

[96] L. Yu and T. H. Chan, 'Moving force identification based on the frequency–time domain method', *Journal of Sound and Vibration*, vol. 261, no. 2, pp. 329–349, 2003.

[97] Y. Liu and W. S. Shepard Jr, 'Dynamic force identification based on enhanced least squares and total least-squares schemes in the frequency domain', *Journal of sound and vibration*, vol. 282, no. 1-2, pp. 37–60, 2005.

[98] Z. Lu and S. Law, 'Identification of system parameters and input force from output only', *Mechanical Systems and Signal Processing*, vol. 21, no. 5, pp. 2099–2111, 2007.

[99] Ł. Jankowski, 'Off-line identification of dynamic loads', *Structural and Multidisciplinary Optimization*, vol. 37, no. 6, pp. 609–623, 2009.

[100] J. Liu, X. Sun, X. Han, C. Jiang and D. Yu, 'Dynamic load identification for stochastic structures based on gegenbauer polynomial approximation and regularization method', *Mechanical Systems and Signal Processing*, vol. 56, pp. 35–54, 2015.

[101] F. E. Gunawan, H. Homma and Y. Kanto, 'Two-step b-splines regularization method for solving an ill-posed problem of impact-force reconstruction', *Journal of Sound and Vibration*, vol. 297, no. 1-2, pp. 200–214, 2006.

[102] T. Kreitinger, M. Wang and H. Schreyer, 'Non-parametric force identification from structural response', *Soil Dynamics and Earthquake Engineering*, vol. 11, no. 5, pp. 269–277, 1992.

[103] G. Liu, W. Ma and X. Han, 'An inverse procedure for identification of loads on composite laminates', *Composites Part B: Engineering*, vol. 33, no. 6, pp. 425–432, 2002.

[104] C.-D. Pan, L. Yu, H.-L. Liu, Z.-P. Chen and W.-F. Luo, 'Moving force identification based on redundant concatenated dictionary and weighted l1-norm regularization', *Mechanical Systems and Signal Processing*, vol. 98, pp. 32–49, 2018.

[105] Y. Mao, X. Guo and Y. Zhao, 'A state space force identification method based on markov parameters precise computation and regularization technique', *Journal of Sound and Vibration*, vol. 329, no. 15, pp. 3008–3019, 2010.

[106] Y. Ding *et al.*, 'Average acceleration discrete algorithm for force identification in state space', *Engineering Structures*, vol. 56, pp. 1880–1892, 2013.

[107] K. Li, J. Liu, X. Han, X. Sun and C. Jiang, 'A novel approach for distributed dynamic load reconstruction by space–time domain decoupling', *Journal of Sound and Vibration*, vol. 348, pp. 137–148, 2015.

[108] B. Mao, S. Xie, M. Xu, X. Zhang and G. Zhang, 'Simulated and experimental studies on identification of impact load with the transient statistical energy analysis method', *Mechanical Systems and Signal Processing*, vol. 46, no. 2, pp. 307–324, 2014.

[109] S. Xie, Y. Zhang, Q. Xie, C. Chen and X. Zhang, 'Identification of high frequency loads using statistical energy analysis method', *Mechanical Systems and Signal Processing*, vol. 35, no. 1-2, pp. 291–306, 2013.

[110] B.-T. Wang and C.-H. Chiu, 'Determination of unknown impact force acting on a simply supported beam', *Mechanical systems and signal processing*, vol. 17, no. 3, pp. 683–704, 2003.

[111] R. Hashemi and M. Kargarnovin, 'Vibration base identification of impact force using genetic algorithm', *International Journal of Mechanical Systems Science and Engineering*, vol. 1, no. 4, pp. 204–210, 2008.

[112] H. Inoue, N. Ikeda, K. Kishimoto, T. Shibuya and T. Koizumi, 'Inverse analysis of the magnitude and direction of impact force', *JSME international journal. Ser. A, Mechanics and material engineering*, vol. 38, no. 1, pp. 84–91, 1995.

[113] T. Jang, H. Baek, S. Han and T. Kinoshita, 'Indirect measurement of the impulsive load to a nonlinear system from dynamic responses: Inverse problem formulation', *Mechanical Systems and Signal Processing*, vol. 24, no. 6, pp. 1665–1681, 2010.

[114] S.-J. Kim and S.-K. Lee, 'Experimental identification for inverse problem of a mechanical system with a non-minimum phase based on singular value decomposition', *Journal of mechanical science and technology*, vol. 22, no. 8, pp. 1504–1509, 2008.

[115] T. Jang, 'A method for simultaneous identification of the full nonlinear damping and the phase shift and amplitude of the external harmonic excitation in a forced nonlinear oscillator', *Computers & Structures*, vol. 120, pp. 77–85, 2013.

[116] Z. Chen, T. H. Chan and A. Nguyen, 'Moving force identification based on modified preconditioned conjugate gradient method', *Journal of sound and vibration*, vol. 423, pp. 100–117, 2018.

[117] F. E. Gunawan, 'Levenberg–marquardt iterative regularization for the pulse-type impact-force reconstruction', *Journal of Sound and Vibration*, vol. 331, no. 25, pp. 5424–5434, 2012.

[118] W. Steven and C. Narciso, 'Encyclopedia of physical science and technology (third edition)', 2003.

[119] F. B. Fitch, 'Warren s. mcculloch and walter pitts. a logical calculus of the ideas immanent in nervous activity. bulletin of mathematical biophysics, vol. 5 (1943), pp. 115–133.', *The Journal of Symbolic Logic*, vol. 9, no. 2, pp. 49–50, 1944.

[120] F. Rosenblatt, 'The perceptron: A probabilistic model for information storage and organization in the brain.', *Psychological review*, vol. 65, no. 6, p. 386, 1958.

[121] D. E. Rumelhart, G. E. Hinton and R. J. Williams, 'Learning representations by back-propagating errors', *nature*, vol. 323, no. 6088, pp. 533–536, 1986.

[122] L. R. Medsker and L. Jain, 'Recurrent neural networks', *Design and Applications*, vol. 5, 2001.

[123] S. Hochreiter, 'The vanishing gradient problem during learning recurrent neural nets and problem solutions', *International Journal of Uncertainty, Fuzziness and Knowledge-Based Systems*, vol. 6, no. 02, pp. 107–116, 1998.

[124] 'UFIM Racing Homologation Programme for Helmets. Mies, Switzerland.', Standard, 2017.

[125] A. J. Padgaonkar, K. Krieger and A. King, 'Measurement of angular acceleration of a rigid body using linear accelerometers', 1975.

[126] J. K. Reichert and J. P. Landolt, 'Digital and analog filters for processing impact test data', SAE Technical Paper, Tech. Rep., 1981.

[127] C. Gehre, H. Gades and P. Wernicke, 'Objective rating of signals using test and simulation responses', in *21st International Technical Conference on the Enhanced Safety of Vehicles Conference (ESV)*, 2009, pp. 09–0407.

[128] M. Ghajari, Z. Sharif-Khodaei, M. Aliabadi and A. Apicella, 'Identification of impact force for smart composite stiffened panels', *Smart Materials and Structures*, vol. 22, no. 8, p. 085 014, 2013.

[129] A. Idesman, 'Accurate finite-element modeling of wave propagation in composite and functionally graded materials', *Composite Structures*, vol. 117, pp. 298–308, 2014.

[130] K. Zimmerman *et al.*, 'Player position in american football influences the magnitude of mechanical strains produced in the location of chronic traumatic encephalopathy pathology: A computational modelling study', *Journal of biomechanics*, vol. 118, p. 110 256, 2021.

[131] A. Alshareef, J. S. Giudice, J. Forman, R. S. Salzar and M. B. Panzer, 'A novel method for quantifying human in situ whole brain deformation under rotational loading using sonomicrometry', *Journal of neurotrauma*, vol. 35, no. 5, pp. 780–789, 2018.

[132] F. Abayazid, K. Ding, K. Zimmerman, H. Stigson and M. Ghajari, 'A new assessment of bicycle helmets: The brain injury mitigation effects of new technologies in oblique impacts', *Annals of biomedical engineering*, vol. 49, no. 10, pp. 2716–2733, 2021.

[133] M. Fahlstedt *et al.*, 'Ranking and rating bicycle helmet safety performance in oblique impacts using eight different brain injury models', *Annals of biomedical engineering*, vol. 49, no. 3, pp. 1097–1109, 2021.

[134] A. E. Jolly *et al.*, 'Detecting axonal injury in individual patients after traumatic brain injury', *Brain*, vol. 144, no. 1, pp. 92–113, Nov. 2020, ISSN: 0006-8950. DOI: 10.1093/brain/awaa372.

[135] K. M. Kinnunen *et al.*, 'White matter damage and cognitive impairment after traumatic brain injury', *Brain*, vol. 134, no. 2, pp. 449–463, 2011.

[136] P. M. Arenth, K. C. Russell, J. M. Scanlon, L. J. Kessler and J. H. Ricker, 'Corpus callosum integrity and neuropsychological performance after traumatic brain injury: A diffusion tensor imaging study', *The Journal of head trauma rehabilitation*, vol. 29, no. 2, E1, 2014.

[137] M. F. Kraus, T. Susmaras, B. P. Caughlin, C. J. Walker, J. A. Sweeney and D. M. Little, 'White matter integrity and cognition in chronic traumatic brain injury: A diffusion tensor imaging study', *Brain*, vol. 130, no. 10, pp. 2508–2519, 2007.

[138] K. Caeyenberghs *et al.*, 'Correlations between white matter integrity and motor function in traumatic brain injury patients', *Neurorehabilitation and neural repair*, vol. 25, no. 6, pp. 492–502, 2011.

[139] G. S. Choi *et al.*, 'Classification of cause of motor weakness in traumatic brain injury using diffusion tensor imaging', *Archives of neurology*, vol. 69, no. 3, pp. 363–367, 2012.

[140] B. L. Edlow *et al.*, 'Diffusion tensor imaging in acute-to-subacute traumatic brain injury: A longitudinal analysis', *BMC neurology*, vol. 16, no. 1, pp. 1–11, 2016.

[141] D. Drijkoningen *et al.*, 'Training-induced improvements in postural control are accompanied by alterations in cerebellar white matter in brain injured patients', *NeuroImage: Clinical*, vol. 7, pp. 240–251, 2015.

[142] J. H. Cole *et al.*, 'Spatial patterns of progressive brain volume loss after moderate-severe traumatic brain injury', *Brain*, vol. 141, no. 3, pp. 822–836, 2018.

[143] X. Yu, I. Logan, I. d. P. Sarasola, A. Dasaratha and M. Ghajari, 'The head and brain protection of modern motorcycle helmets under oblique impacts', *Unpublished manuscrip*, 2021.